University of Nevada, Reno

COSEISMIC AND POSTSEISMIC DEFORMATION OF 2011 MW 9 TOHOKU EARTHQUAKE - A NONLINEAR INVERSION OF GPS DATA

A Thesis Submitted in Partial Fulfillment

of the Requirements for the Degree of Master of Science in

Geophysics

by

Yang Zhang

Dr. Corné W. Kreemer / Thesis Advisor

May 2015

UNIVERSITY OF NEVADA RENO

THE GRADUATE SCHOOL

We recommend that the thesis prepared
under our supervision by

YANG ZHANG

entitled

COSEISMIC AND POSTSEISMIC DEFORMATION OF 2011 MW 9 TOHOKU EARTHQUAKE - A NONLINEAR INVERSION OF GPS DATA

be accepted in partial fulfillment of the
requirements for the degree of

MASTER OF SCIENCE

Corné W. Kreemer, Ph.D. – Advisor

William C. Hammond, Ph.D. – Committee Member

Geoffrey Blewitt, Ph.D. – Committee Member

Ilya Zaliapin, Ph.D. – Graduate School Representative

David Zeh, Ph.D. – Dean, Graduate School

May 2015

ABSTRACT

On March 11, 2011, a magnitude Mw = 9.0 megathrust occurred off the Tohoku coast near the Japan trench. This thesis studies the coseismic and postseismic deformation of the earthquake based on the Global Positioning System (GPS) observations. GPS position time series are modeled to extract coseismic and postseismic displacements. Coseismic displacements are used to invert for coseismic slip. A nonlinear algorithm called Occam's algorithm is employed to invert for the rake of the fault slip (83°). For postseismic deformation, the coupled effect of afterslip and viscoelastic are considered. Nonlinear parameters such as the viscosity of the lower crust and the uppermost mantle ($10^{18.9} \approx 7.9 \times 10^{18} Pa \cdot s$), the elastic thickness (51 km), and the rake of fault slip (83 °) are found with the same nonlinear inversion algorithm. Different components of deformation caused by different mechanisms of deformation are computed, and the results show that afterslip dominates in the first 100 days after the mainshock and the viscoelastic relaxation dominates in the later days of the postseismic deformation.

This thesis is dedicated to
my father Zhang, Xiong-Zhi (张雄志),
my mother Yang, Xiao-Lan (杨晓兰),
and my sister Zhang, Ran (张苒).
Without your love, nothing in my life is possible.

ACKNOWLEDGEMENTS

It would not have been possible to write this thesis without the help and support of the kind people around me, to only some of whom it is possible to give particular mention here.

I would like to express the deepest appreciation to my committee chair, Dr. Corné Kreemer, who graciously welcomed me into Nevada Geodetic Lab (NGL) and made my research a top priority. He opened the door for me to the research of postseismic deformation and pointed me to the study of the 2011 Tohoku earthquake. During the years in NGL, he gives me the ultimate support and shows the genuine patience toward my immaturity.

I would like to thank Dr. William Hammond, whose knowledge in inversion and postseismic deformation has guided me through many difficulties. I would like to thank Dr. Geoffrey Blewitt. His brilliant insight inspires me. I also would like to thank other former and current colleagues in NGL, including Jay Goldfarb, Elliot Klein and Robin Chacko. Their friendship and helps encourage me all the time. Over four years' study and research at NGL in the University of Nevada, Reno have been the most wonderful experience in my life.

I would like to thank my thesis committee, Corné Kreemer, William Hammond, Geoffrey Blewitt, and Ilya Zaliapin, for their insightful comments, participation and interest in my work.

I thank NFS for supporting my work (grant EAR-0911754) and GEONET Japan for making data available. I thank Heather Stamps for her generous help with proofreading.

TABLE OF CONTENTS

LIST OF TABLES

LIST OF FIGURES

CHAPTER 1
INTRODUCTION

On March 11, 2011, a destructive $M_w 9.0$ megathrust earthquake ruptured the plate interface off the coast of Tohoku, Japan and extended to the Japan trench. The quake's epicenter was located approximately 100 km east of the Oshika Peninsula of Tohoku and the hypocenter at an underwater depth of approximately 30 km. It is the most powerful earthquakes recorded by modern instruments to have hit Japan, triggering tsunami waves up to 40.5 meters tall. Following the quake, Japan experienced over 1000 aftershocks, several of which reaching over magnitude 7.0 M_w. Sadly, these quakes resulted in more than fifteen thousand deaths and an estimated economic cost of US $235 billion, making this the costliest natural disaster in world history.

This earthquake occurred within an active plate boundary where seismicity is high. The Pacific Plate is subducting west-northwestward under the Okhotsk plate at a rate of 83 mm/year offshore of the Tohoku and northern Kanto regions [*Sella et al.*, 2002; *Apel et al.*, 2006](Figure 1.1). Figure 1.2 from *Tajima et al.* [2013] shows significant historical earthquakes off the coast of Tohoku. In Japan's historical earthquake catalog, the earliest earthquake that is comparable to the 2011 Tohoku earthquake in mechanism and magnitude happened in A.D. 869 (the Jogan era), which was estimated to be M8.3 or larger and triggered significant tsunami as well [*Minoura et al.*, 2001]. During the 17th to 19th century, there are 8 $M \geq 7$ earthquake, and 4 $M \geq 8$ earthquakes recorded in this region. Over the last century there are 14 M7 earthquakes and 2 M8 earthquakes (the M8.1 normal faulting event in 1933 and the Mw 8.2 1968 Tokachi-Oki subduction zone event) that took place off the coast of Tohoku. However, the magnitude of the March 11, 2011

earthquake has far exceeded the magnitude of those earthquakes, none of which reached M9 [*Tajima et al.*, 2013]. Thus, the occurrence of the 2011 Tohoku earthquake has changed our understanding of the seismicity in this region(e.g. *Ozawa et al.* [2011]; *Simons et al.* [2011]).

A number of geophysical processes involved in this earthquake have been well observed by various modern instruments. Coseismic and postseismic deformation are well recorded by several regional GPS networks in Japan, South Korea [*Baek et al.*, 2012], and China [*Wang et al.*, 2011; *Zhao et al.*, 2012]. In particular, the GPS network in Japan, GEONET, containing more than 1200 continuous GPS sites and covering the Japanese islands [*Sagiya*, 2004], provides the main data for this study. Seismic waves are recorded by globally distributed broadband seismographic networks [*Maeda et al.*, 2011]. The regional gravity change caused by this earthquake has been captured by GRACE satellites [*Wang et al.*, 2012; *Han et al.*, 2014]. The triggered tsunami has been surveyed along the coast and measured by GPS tide gauge [*Fujii et al.*, 2011]. These valuable geophysical data sets have been triggering researches on various important scientific topics.

In this thesis, the coseismic and postseismic deformation of the 2011 Tohoku earthquake observed by GPS are studied. Chapter 2 discusses the GPS positioning time series covering the coseismic and postseismic deformation processes of this earthquake. Based on time series modeling, coseismic and postseismic displacements are estimated. Chapter 3 presents the geodetic coseismic slip inversion. Major published coseismic slip inversion results are summarized. Based on the method developed in that chapter, variations in results are explained. Chapter 4 discusses over three years postseismic deformation of this earthquake. Coupled effect between afterslip and viscoelastic relaxation is considered. Major Earth

structure parameters are inverted for in viscoelastic Earth media, using a nonlinear inversion scheme. The final chapter is a conclusion chapter of the whole thesis.

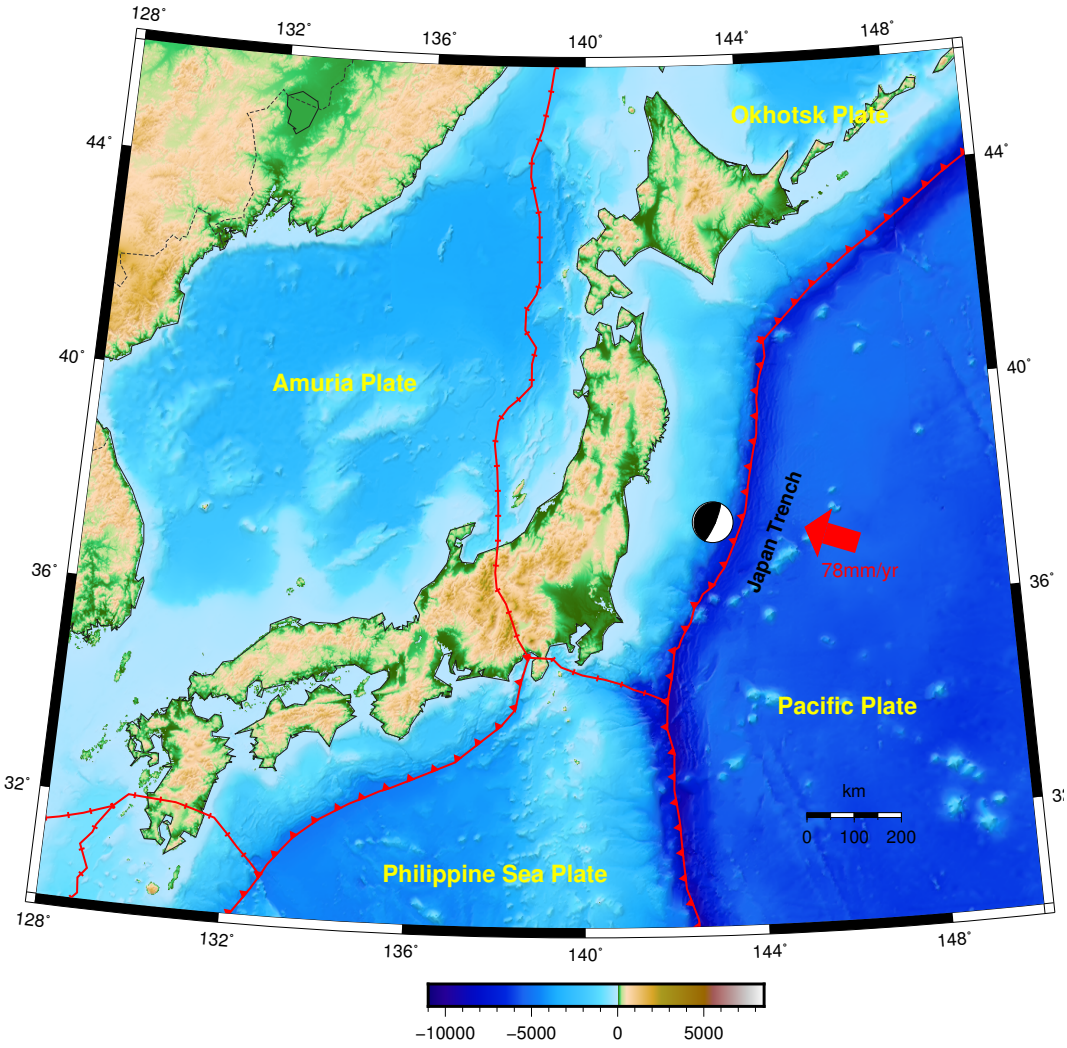

Figure 1.1: Tectonic setting in and around Japan [*Bird*, 2003]. Epicenter and focal mechanism of the 2011 Tohoku earthquake is shown.

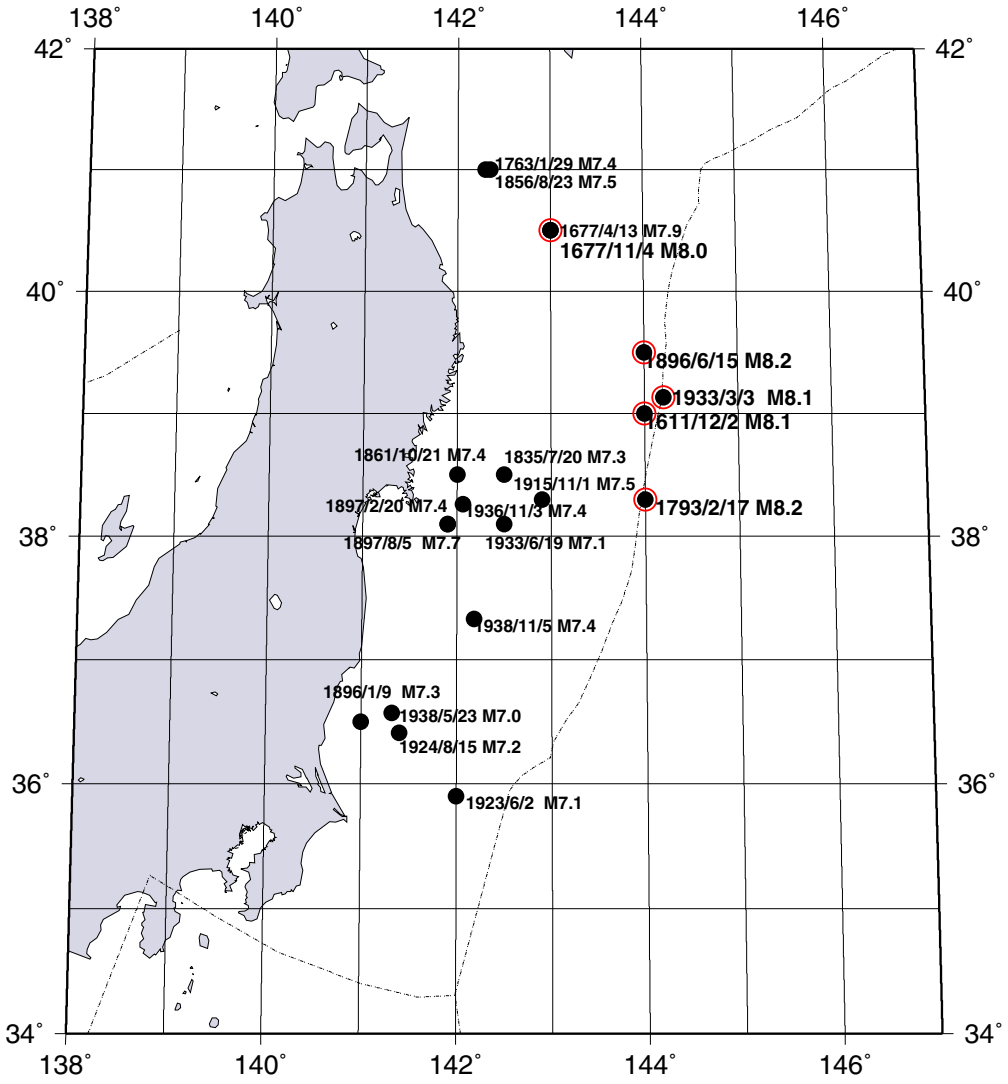

Figure 1.2: Significant historical earthquakes ($M \geq 7$)off the coast of Tohoku before the March 11, 2011 Tohoku earthquake [*Tajima et al.*, 2013]. Events with $M \geq 8$ are indicated by red open circles.

CHAPTER 2

GPS OBSERVATION AND TIME SERIES ANALYSIS

2.1 Introduction

On the continental side of the Japan trench, the large and extensive deformation, from the epicenter to places as far as 3000 km away in Mongolia and the Far-East Russia, has been well recorded by several regional GPS networks, including GEONET in Japan [*Sagiya*, 2004], CMONOC/TEONET in China [*Wang et al.*, 2011; *Zhao et al.*, 2012], and the regional GPS network in South Korea [*Baek et al.*, 2012], as well as several IGS stations. The availability of the unprecedented amount of GPS data better informs our understanding of the deformation of this earthquake.

Understanding the characteristics of co- and post-seismic deformation of Tohoku earthquake provides the observational basis for modeling and interpretation of the underlying mechanisms. For the postseismic deformation in particular, two major mechanisms: afterslip [*Marone et al.*, 1991; *Perfettini*, 2005] and viscoelastic relaxation [*Nur and Mavko*, 1974], have been proposed to explain it. However, the role of each mechanism in the postseismic deformation is controversial.

In this chapter, the major characteristics of coseismic and postseismic deformation of this earthquake are examined based on time series modeling results and coseismic offsets published in other studies. Possible evidence for the existence of viscoelastic relaxation deformation following the 2011 Tohoku earthquake is proposed.

2.2 GPS Data and Time Series Modeling

The whole territory of the Japan islands has been covered by a dense GPS array since 1994, called GEONET [*Sagiya*, 2004] (Figure 2.2). The average distance between stations is about 20 km $\sim$ 30 km. Daily time series of GEONET stations are produced at the Nevada Geodetic Lab and used to estimate the coseismic and postseismic displacements at each station based on the method introduced below.

In order to account for steady plate motion and non-tectonic seasonal variations, GPS positioning time series are detrended using at least 2 years of observation before the 2011 Tohoku earthquake. The detrending is based on the model

$$y_i = kt_i + b + S_1 sin(\omega_1 t_i) + C_1 cos(\omega_1 t_i) + S_2 sin(\omega_2 t_i) + C_2 sin(\omega_2 t_i),$$

where $y_i(t_i)$ are epochs of time series before the mainshock; the first two terms on the right indicate linear plate motion; the rest of terms on the right represent annual and semi-annual seasonal variations with $\omega_1 = 2\pi/(1yr)$ and $\omega_2 = 2\pi/(0.5yr)$, respectively.

The detrended postseismic time series of each station are then modeled with either one exponentially decaying term for far-field stations

$$\mathbf{y}_i = \mathbf{a}_1 \left(1 - e^{\frac{T_0 - t_i}{\tau_1}}\right) \quad \tau_1 > 0 \ ,$$

or two exponential decaying terms for near-field stations

$$\mathbf{y}_i = \mathbf{a}_1 \left(1 - e^{\frac{T_0 - t_i}{\tau_1}}\right) + \mathbf{a}_2 \left(1 - e^{\frac{T_0 - t_i}{\tau_2}}\right) \quad \tau_2 > \tau_1 > 0 \ ,$$

where $\mathbf{y_i}$ is the vector displacement at time t_i, and $\mathbf{a_1}$ and $\mathbf{a_2}$ are vector magnitudes for the corresponding temporal terms. The decaying parameter τ_1 and τ_2 control how fast the time series decay. Note that the three components of a station share

the same decaying term(s). Hereinafter, these two models are referred to as Model EXP and Model 2EXPs, respectively. Offsets in time series due to instrumental change or other earthquakes are also fitted wherever necessary. There was a slow earthquake event at Bungo Channel from January to October in 2010 before the 2011 Tohoku earthquake [*Ozawa et al.*, 2013], which interrupted the preseismic time series of stations near Bungo Channel. We exclude the section of the time series that the slow event happened when estimating preseismic velocities, and replaced it with an offset.

2.3 Results and Discussion

2.3.1 Model EXP versus Model 2EXPs

For near-field stations, two exponential terms are needed to fit the time series. Taking station 0550 as an example, Figure 2.5 compares how well data from the east component of site 0550 can be fitted by Model 2EXPs against its fit by Model EXP. The residual time series of Model EXP shows a clear curvature suggesting that there are trends in the time series not being fitted. However, the residual time series of Model 2EXPs shows a uniform residual suggesting that Model 2EXPs provides a better fit. Figure 2.2 shows the spatial distribution of stations fitted with different kinds of models (stations that are fitted with Model 2EXPs and Model EXP, are marked with red and black vectors, respectively). Most stations in Honshu are modeled with Model 2EXPs, with exception to those located at southwestern end of Honshu, which can be satisfactorily modeled with Model EXP. Stations in Hokkaido, western half of Shikoku, and Kyushu are modeled with Model EXP,

as well. (For administrative region names mentioned above, refer to the map in Appendix E.) Model 2EXPs could have important meaning for postseismic deformation study. For instance, *Ergintav et al.* [2009] and *Hearn et al.* [2009] interpret that the short duration process in Model 2EXPs is afterslip and the slower process is the viscoelastic relaxation.

2.3.2 Observed Coseismic Displacements

The near-field coseismic ground deformation of the 2011 Tohoku earthquake is large. Figure 2.6 shows the observed displacements at Tohoku. Both the largest horizontal and vertical displacements are observed at station J550, 76 km away from the epicenter. The station subsides ∼1.1 meter and moves southeastwardly ∼5.5 meter.

Vertical displacements observed at Tohoku shows a very clear pattern that agrees well with characteristics of the ground deformation of typical thrust faulting. Stations along the coast of Pacific ocean subside, and the ones along the coast of the Japan Sea go up. The belt zone of zero vertical displacements appears in the central area of Tohoku closer to the Japan Sea side of the island.

Figure 2.7 shows for a larger area how the magnitude of the horizontal displacements decay on Japanese islands. The horizontal displacements peak at eastern coast of Tohoku. On the island of Kyushu, about 1200 kilometers away from the epicenter, the coseismic displacements are still significant (Figure 2.11), where the average magnitude of horizontal coseismic displacements is as high as ~ 2 cm. The complete list of all the stations and their estimated coseismic displacements can be found in Appendix D.

In order to get a more comprehensive picture of the deformation caused by the 2011 Tohoku earthquake, GEONET data in Japan is combined with two other major regional networks: CMONOC/TEONET in China [*Wang et al.*, 2011; *Zhao et al.*, 2012] and the regional GPS network in South Korea [*Baek et al.*, 2012], where data from these stations were unavailable for the processing of raw GPS observations performed at NGL. Akaike information criterion (AIC) test also indicates that Model 2EXPs is preferable to Model EXP. Figure 2.1 shows the spatial distribution these stations (including some IGS stations). An extensive area from the epicenter to as far as 3000 kilometers away are all covered by GPS stations. Figure 2.8 shows the spatial decay of the magnitude of horizontal coseismic displacements across the continent. As far as over 3000 km away form the epicenter at station ULAB, 2$\sim$3 mm coseismic displacement is observed in the east component, which is just within the capability of movement detection for current GPS technique ($\sim$1 mm).

The GPS visible vertical movement has much smaller spatial scale than the horizontal movement. The farthest stations from the epicenter that shows explicit vertical coseismic displacement are located about 600 km away form the epicenter (e.g. stations located near the boundary between Kansai and Chubu), which is about four times smaller than the epicentral distance of the farthest station that shows explicit horizontal displacements ($\sim$ 3000 km). This is because the vertical component of GPS is several times less sensitive than the horizontal components, and vertical movement is much smaller than horizontal movement in megathrust. Figure 2.9 shows the magnitude of vertical displacements in Japan. Although we estimate the vertical displacements for most stations, only stations in Tohoku have obvious vertical displacements. To the south of the Tohoku area, stations in Chubu and Kanto show vague vertical coseismic displacements that can be barely picked up by eyes; vertical movements in time series of stations that are located in Kansai

and west of it are almost indiscernible by eyes. To the north of the Tohoku area, the Hokkaido island is located near the nodal plane of the coseismic deformation of the Tohoku megathrust, thus from central Tohoku to Hokkaido, the magnitude of coseismic displacements decreases quickly. Needless to mention, in regional networks in Korea and China, it is not possible to observe any vertical movement related to this earthquake. The modeling in the next chapter will further confirm these observations.

2.3.3 Observed Postseismic Displacements

The earthquake triggers a significant postseismic deformation, which is still going on today and will last for decades. Figure 2.10 shows the observed postseismic displacements in the near-field at day 1200 after the earthquake. The largest postseismic displacements is found at station J550, with vertical displacements being $\approx 0.4m$ and horizontal displacements being $\approx 0.7m$. The vertical postseismic deformation at Tohoku shows the opposite movement to the vertical coseismic deformation. Stations along the Pacific coast uprise and those along the coast of Japan Sea subside during the postseismic phase of deformation.

Postseismic deformation is much harder to interpret than coseismic deformation because of the multitude of mechanisms of postseismic deformation. Two mechanisms, afterslip and viscoelastic relaxation have been proposed to explain large scale postseismic deformation. However, it is not clear whether one of them dominates or they are actively coupled in the postseismic deformation phase. Although this section focuses on observation only, one of the purposes of the analysis is to illuminate the important problem of how different mechanisms drive the

postseismic deformation.

Many studies have suggested that afterslip of the 2011 Tohoku Earthquake is much smaller than its coseismic slip (e.g. *Ozawa et al.* [2012]; *Diao et al.* [2013]; *Yamagiwa et al.* [2014]). If the only mechanism of the postseismic deformation is afterslip, this implies that the postseismic deformation should be smaller in magnitude and extent comparing to coseismic deformation. However, what we observe in the postseismic deformation of the 2011 Tohoku earthquake is that the spatial extent of the postseismic deformation is comparable to that of the coseismic deformation; the magnitude of postseismic displacements are close or even larger than that of the coseismic displacements, especially for far-field stations. We can see this phenomenon in both horizontal and vertical components.

Figure 2.13 shows time series of horizontal components recorded at several far field stations. Postseismic displacements coexist and can surpass coseismic displacements. We don't have postseismic displacements data out of Japan except several IGS stations. However, according to studies by *Baek et al.* [2012] and *Shestakov et al.* [2012] the horizontal postseismic deformation happened in an area in size similar to that of coseismic deformation.

For the vertical deformation, the area where the postseismic vertical displacements in the time series can be visually identified is about the same in size as the area where the coseismic displacements are visually identified, i.e. northern and eastern Honshu (Chubu, Kanto and Tohoku).

In summary, why are postseismic displacements larger than coseismic displacements in the far-field? The possible answer is that beside afterslip, viscoelastic relaxation is also taking place.

In addition to the evidence based on the comparisons of extent and magnitude of co- and post-seismic deformation, another possible piece of evidence of viscoelastic relaxation comes from the azimuthal difference between co- and post-seismic displacement vectors. Figure 2.11 shows that on Kyushu, the observed horizontal postseismic displacements have almost the same magnitude as the observed horizontal coseismic displacements. However, a striking feature is that the observed coseismic and postseismic displacement vectors on Kyushu is not aligned. There are 15∼30 °azimuthal differences between coseismic and postseismic displacements, and the postseismic deformation on Kyushu has more northward movement than the coseismic deformation here. If coseismic and postseismic deformation are all caused by slip on the fault, at a distance this far from the epicenter, there should not be significant azimuthal differences between coseismic and postseismic displacements.

2.4 Conclusion

In this study, based on time series analysis over 1300 stations and published coseismic offsets of South Korea and China's regional GPS networks, the coseismic and postseismic deformation of the 2011 Tohoku earthquake is carefully examined. The crustal deformation induced by this earthquake are both large and extensive. The onshore coseismic and 3-year postseismic displacements have exceeded 5 m and 0.7 m in the near-field, respectively, and reached as far as 3000 km away at stations located in Mongolia and far-east Russia. The decaying trends of the co- and post-seismic deformation are analyzed and compared. The horizontal movement of both co- and post-seismic deformation has been observed by the farthest stations used in this study(∼3000 km away from the epicenter). And the verti-

cal movement is only visually explicit in GPS time series in northern and eastern Honshu (Chubu, Kanto and Tohoku) within 600km from the epicenter.

Time series analysis carried out in this study provides important implications to the mechanisms of the postseismic deformation of the Tohoku earthquake. While the afterslip is much smaller than the coseismic slip, why do the co- and post-seismic deformation have the similar spatial extent in both vertical and horizontal components? The answer might be beside afterslip, there is another mechanism contribute the postseismic deformation, i.e. viscoelastic relaxation. In addition, the azimuthal difference between the observed co- and post-seismic displacements also suggest viscoelastic relaxation deformation. We will further investigate the multitude of postseismic deformation mechanisms in the following chapters.

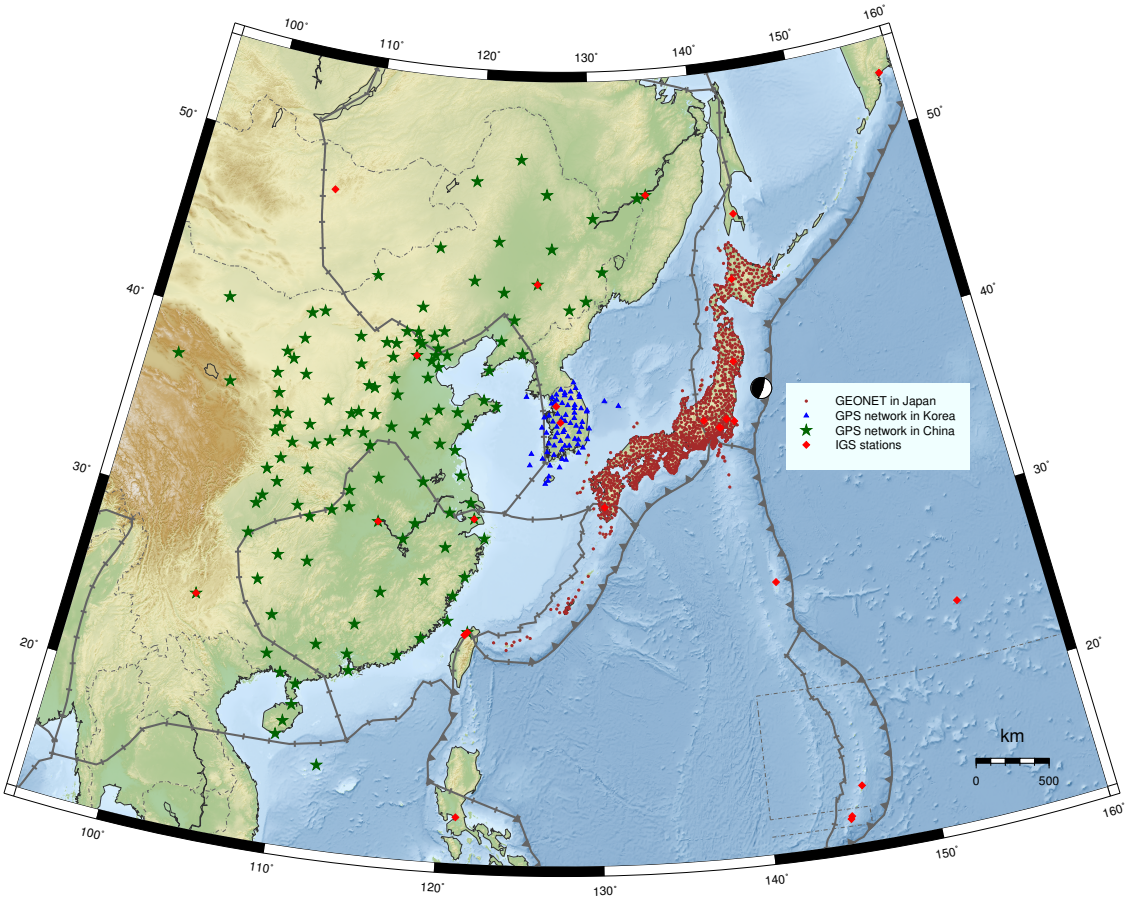

Figure 2.1: Map of all stations from three regional networks, as well as some IGS stations.

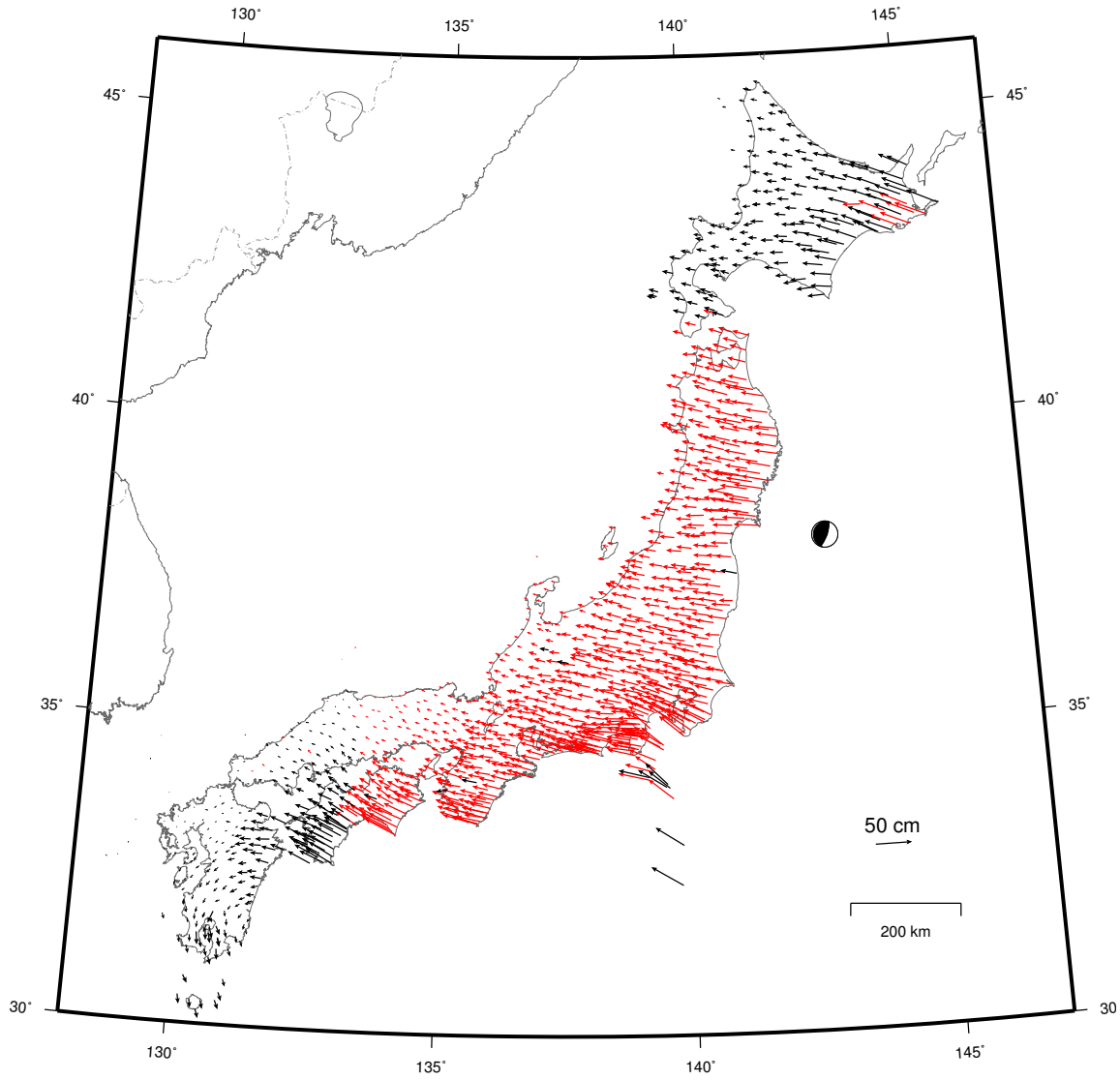

Figure 2.2: GEONET stations and estimated preseismic velocities with respect to Eurasian plate (IGS08 Eurasian pole [*Kreemer et al.*, 2014]). For postseismic time series modeling, sations marked with red vectors are modeled with 2EXPs model, and stations marked with black vectors are modeled with EXP model.

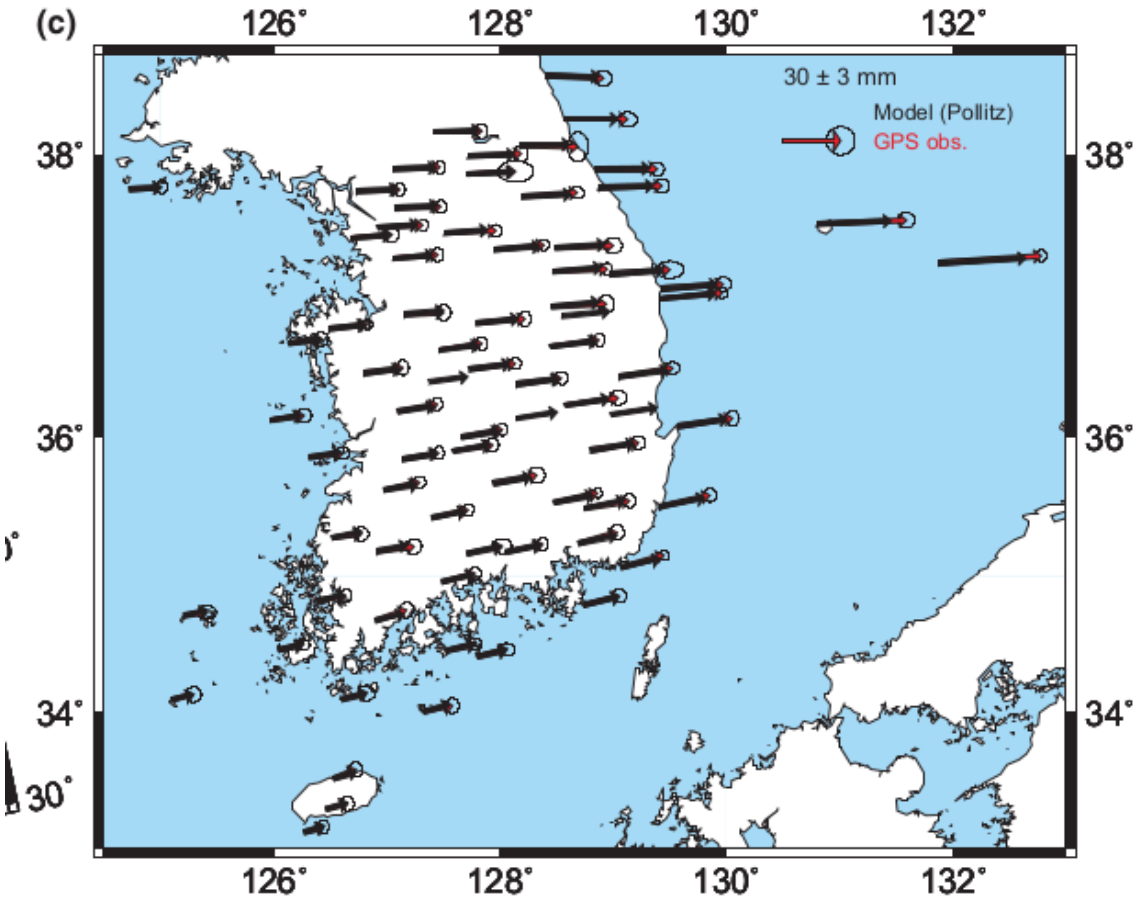

Figure 2.3: The regional GPS network in Korea with estimated coseismic slip. Coseismic slip results are from *Baek et al.* [2012].

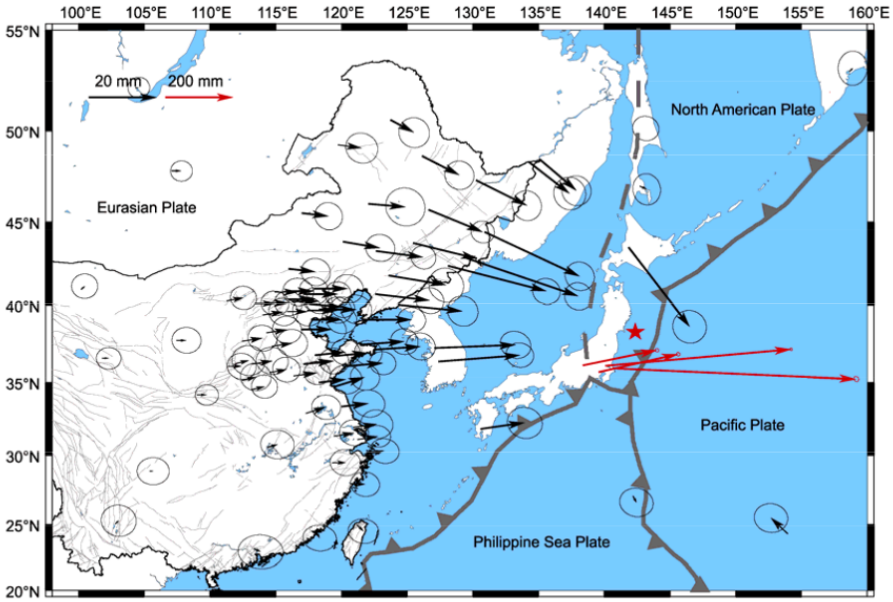

Figure 1 GPS-observed coseismic displacements in eastern China associated with the Tohoku-oki earthquake. The error ellipses represent 90% confidence.

Figure 2.4: The regional GPS network in China with estimated coseismic displacements. Coseismic slip results are from *Wang et al.* [2011]; *Zhao et al.* [2012].

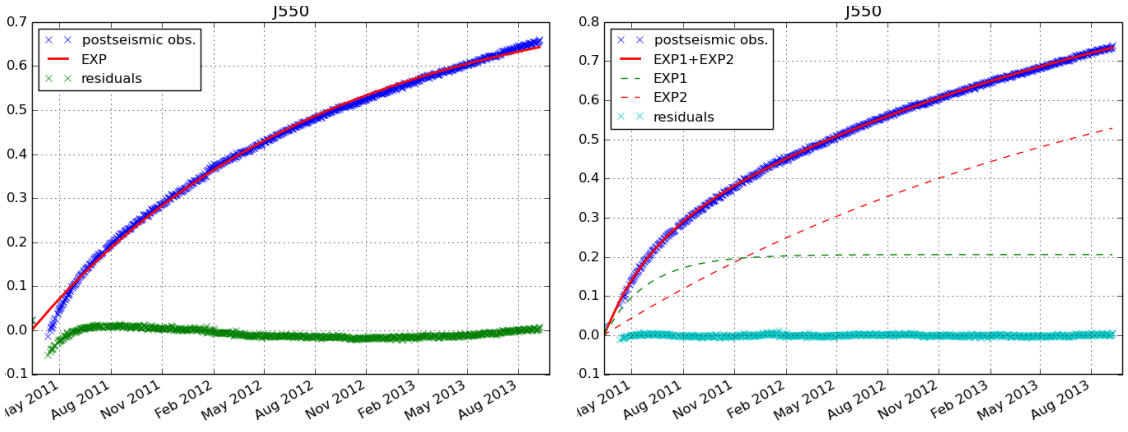

Figure 2.5: Near-field stations fitted with Model EXP and Mode 2EXPs.

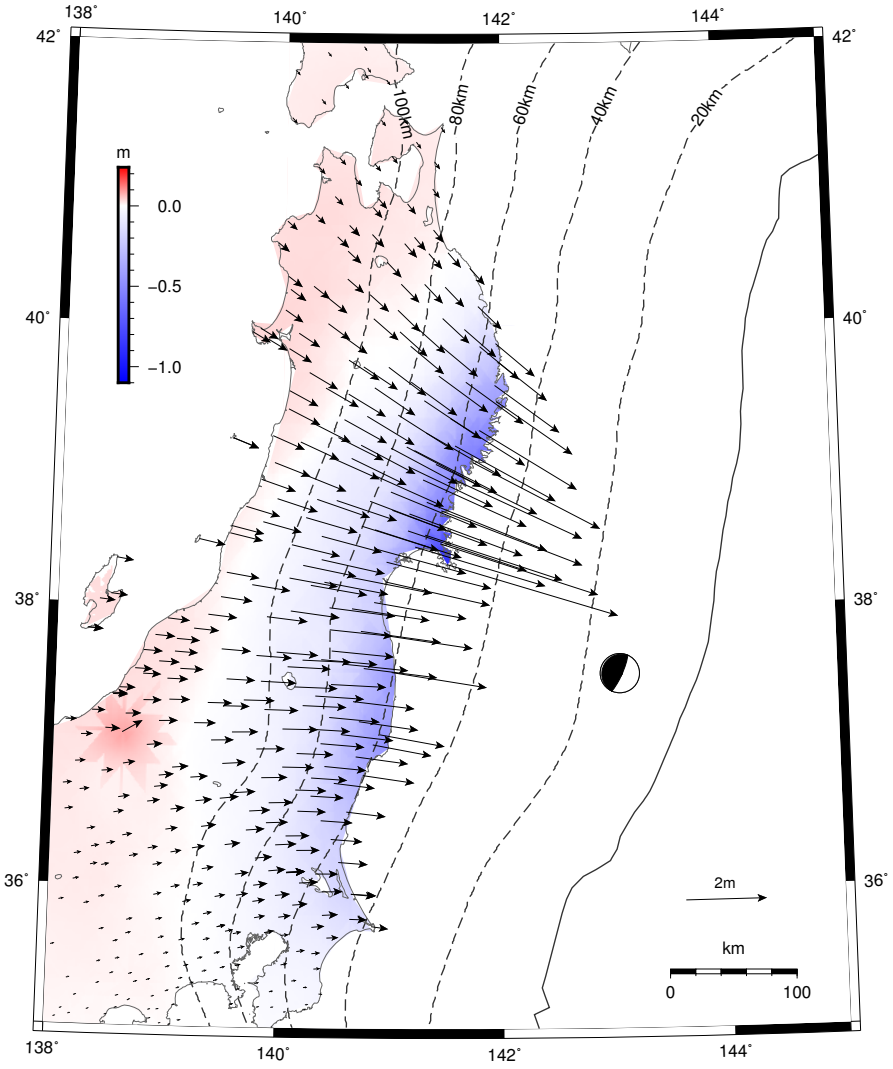

Figure 2.6: Observed coseismic displacements at Tohoku. Horizontal displacements are shown with vectors. Vertical displacements are shown in colors. Dashed lines are slab contours.

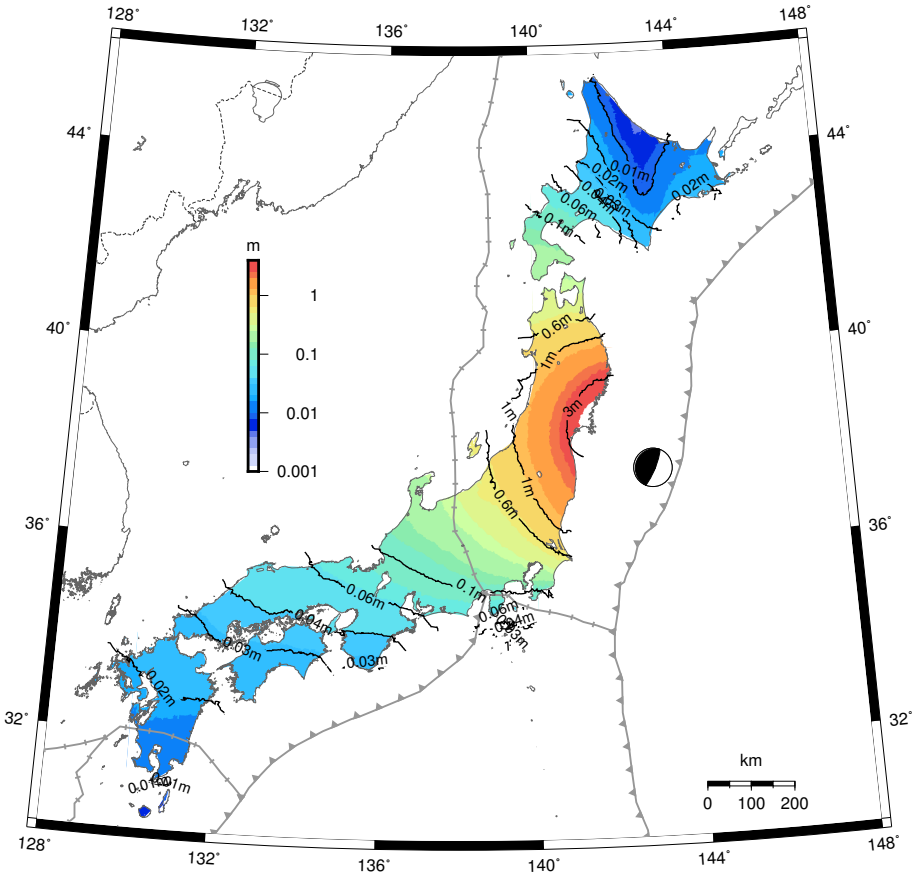

Figure 2.7: Magnitude of the observed horizontal coseismic displacements.

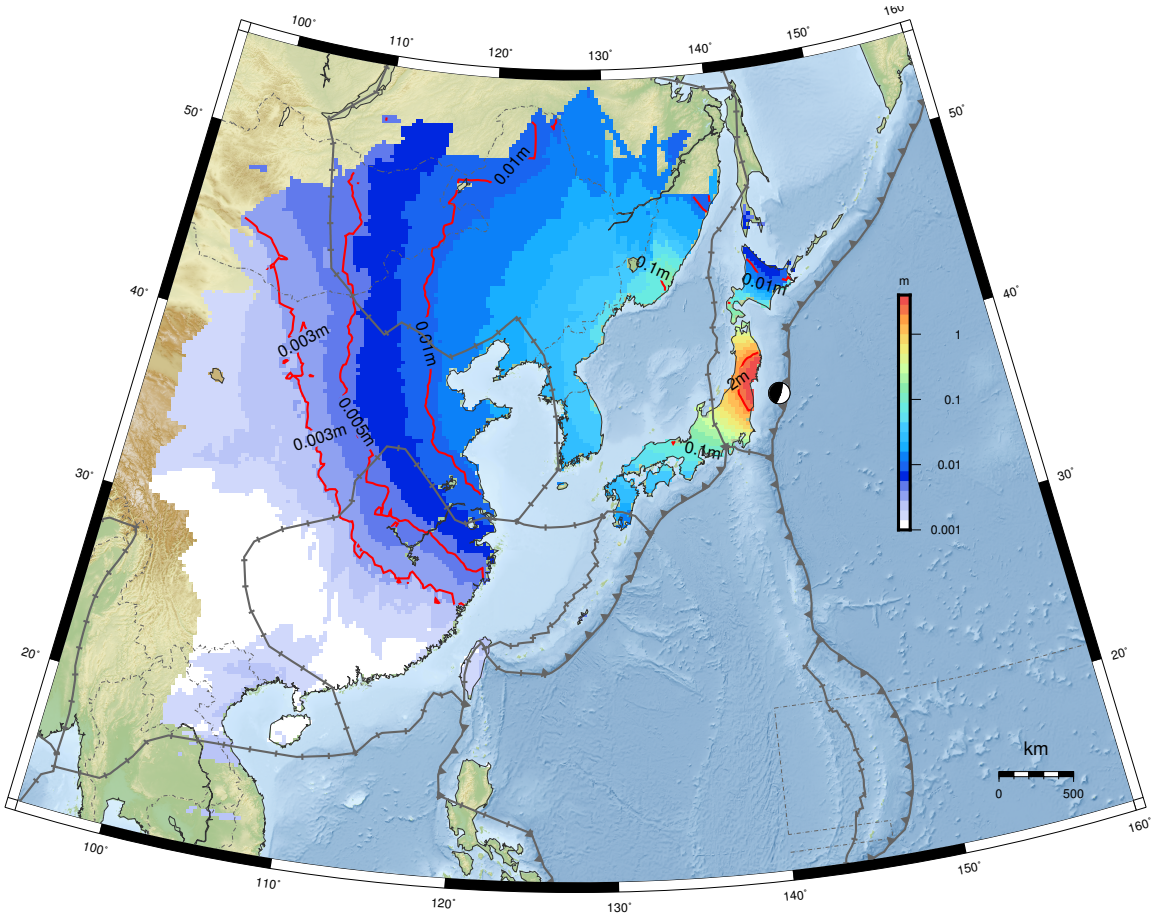

Figure 2.8: Magnitude of the observed horizontal coseismic displacements across the continent, combining data from this analysis, as well as [*Wang et al.*, 2011] and [*Zhao et al.*, 2012].

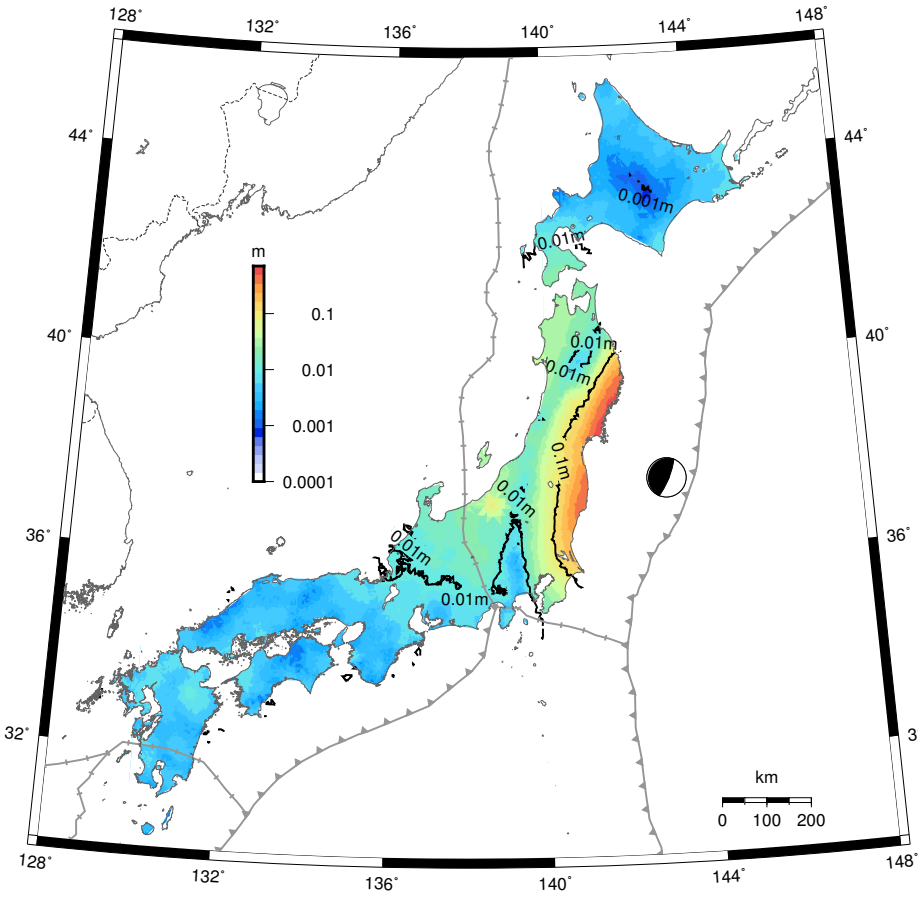

Figure 2.9: Magnitude of the observed vertical coseismic displacements in Japan.

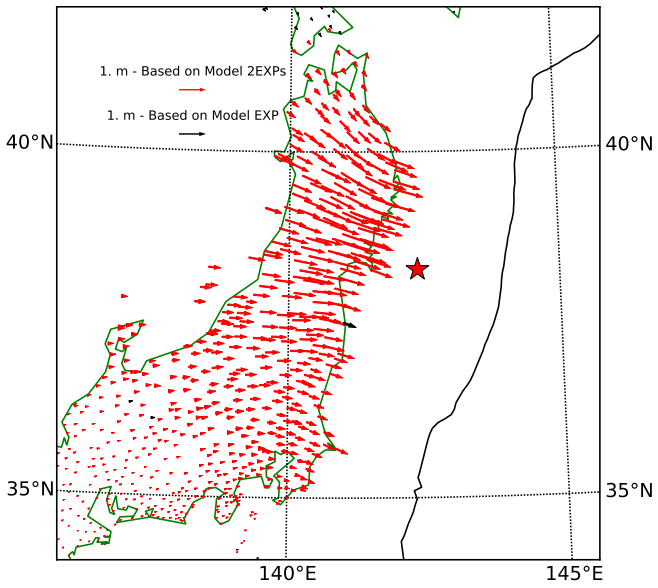

Figure 2.10: Observed postseismic displacements in the near-field at Honshu at day 1200 after the mainshock.

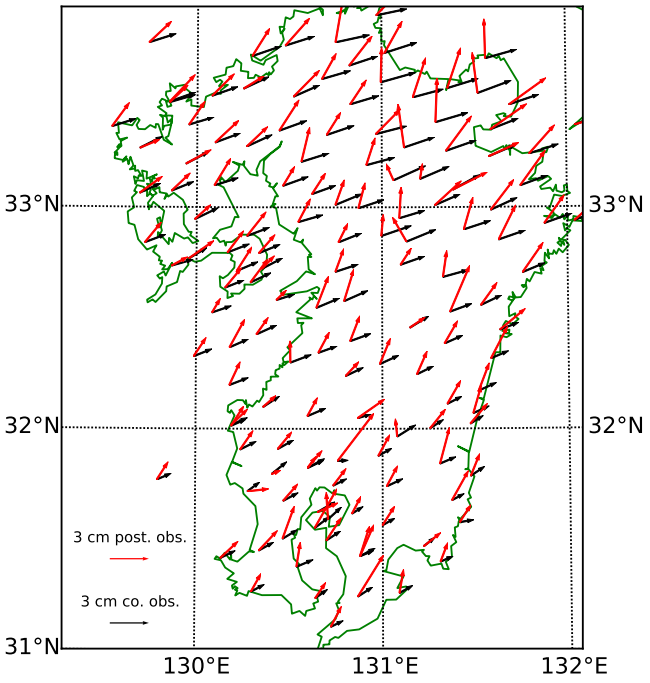

Figure 2.11: Observed coseismic (red vectors) and postseismic displacements (1200 days after the mainshock, black vectors) at Kyushu.

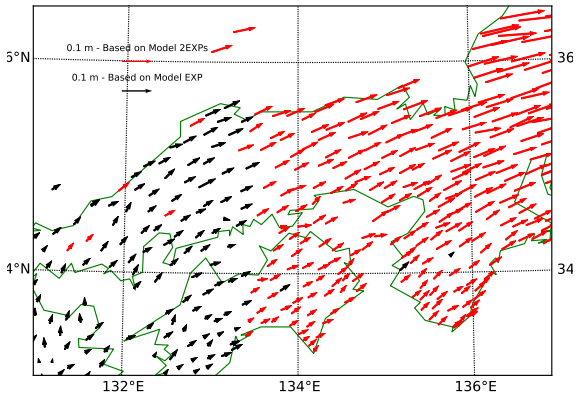

Figure 2.12: Estimated postseismic displacements at day 1200 after the main shock. Red and black vectors mark the stations that are fit with Model 2EXPs and Model EXP, respectively.

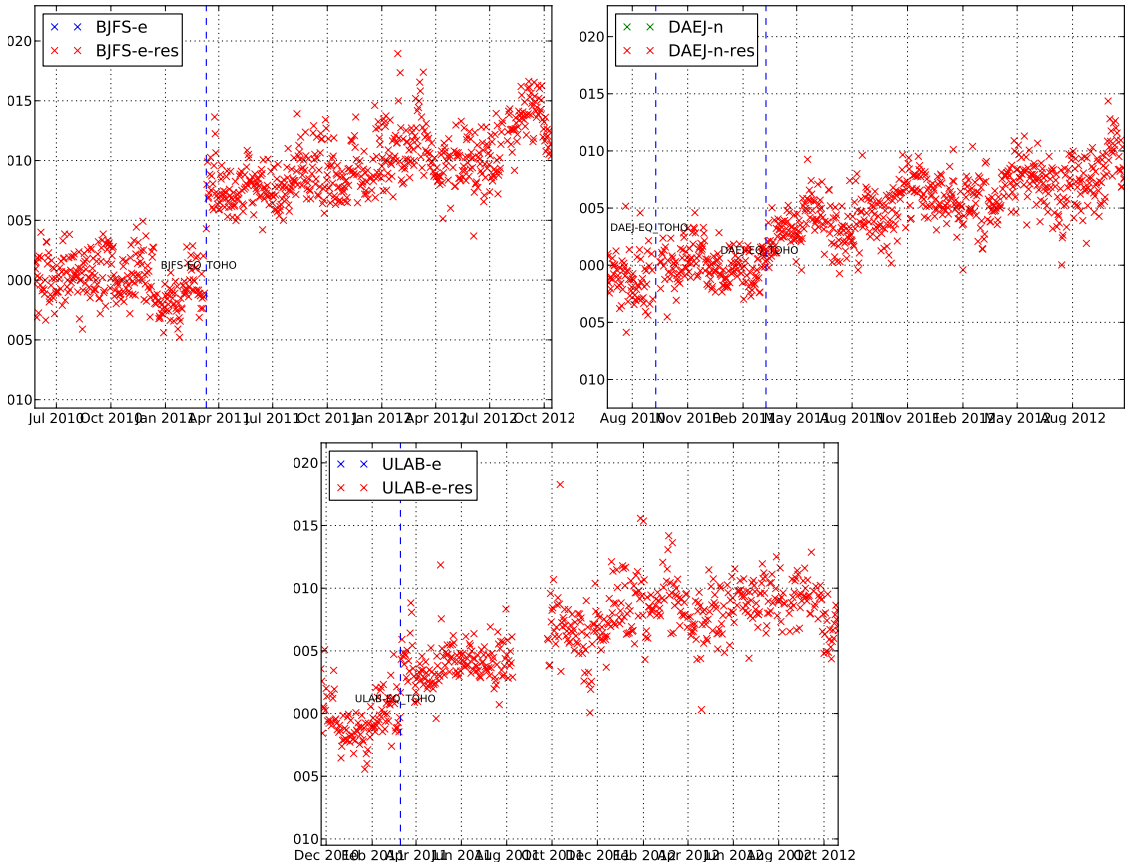

Figure 2.13: Far field stations

CHAPTER 3

COSEISMIC SLIP INVERSION

3.1 Introduction

Since the 2011 Tohoku earthquake, many studies on the static coseismic slip of this earthquake have been published. Various kinds of geophysical data sets have been utilized, for instance, seismic data, GPS data, GRACE gravity data and tsunami data. Different geometries of the Earth and the fault are considered for modeling, such as elastic half-space Earth model, spherical Earth model, and models constructed using finite element method which allows great flexibility. Furthermore, different inversion techniques are employed, from conventional least square with different regularization strategies [*Ozawa et al.*, 2012; *Evans and Meade*, 2012] to Bayesian method [*Minson et al.*, 2014].

Results obtained from various data sets and methods show quite different details, including the most important geophysical quantities like seismic moment, maximum slip and location of maximum slip. Moment magnitudes inferred by geodetic data range from Mw9.0 to Mw9.2. The corresponding seismic moment of the latter is twice of the former. Reported maximum slip varies from 20 meter to 70 meter. The locations of the maximum slip change from at the trench to 30 $\sim$ 40 km at depth. Therefore, a basic question we ask in this section is why do such huge difference exist in the coseismic slip inversion results? I will try to answer this question based on my own inversion method. Understanding why it is hard to reach consensus on static slip inversion of the 2011 Tohoku earthquake is very important. It reveals the limit of the data sets and methods. More importantly, it tells us the reliability of the results: which part of results are well understood and

which part of results contains uncertainty.

As the analysis in the previous chapter has shown, the deformation caused by the earthquake is huge and extensive. Published geodetic slip models present good fit to near-field data. However, larger scale deformation has not been carefully examined. Questions, such as how well the slip model fit the far-field data, how far the coseismic deformation has reached, and how the coseismic deformation decreases spatially, have not been well answered.

In this chapter, a number of published coseismic slip inversion results are review and compared. A nonlinear inversion algorithm called Occam's Inversion is introduced and used to decide the best rake angle of the coseismic slip. Inverted coseismic slip results are presented and various factors that affect the inversion results are discussed.

3.2 Review: Geodetic Coseismic Slip Inversion Results of 2011 Tohoku Earthquake

The 2011 Tohoku earthquake has been well observed by many modern techniques and thus triggers many studies on coseismic slip distribution of this earthquake. Some studies use mainly geodetic data [*Ozawa et al.*, 2012, 2011; *Pollitz et al.*, 2011; *Ito et al.*, 2011; *Minson et al.*, 2014; *Simons et al.*, 2011]. Some studies exclude geodetic data and use other types of data, such as GRACE observation[*Wang et al.*, 2012], seismic data [*Ammon et al.*, 2011; *Shao et al.*, 2011], and tsunami data[*Fujii et al.*, 2011]. Some studies jointly invert all possible data typies to combine the strength of each data type [*Yokota et al.*, 2011].

In this section, major characteristics of a number of coseismic inversion studies that are completely or partially based on GPS data are summarized and compared. The characteristics compared are data types used, moment/moment magnitude, maximum slip and location of maximum slip.

Table 3.2 summarizes published geodetic coseismic slip inversion results, which show obvious differences. Seismic moment varies from 8.8 to 9.2 [*Simons et al.*, 2011]. The maximum slip varies from near 30 meter to almost 80 meter. Even for studies using the same dataset, quite different results are reported. For example, *Simons et al.* [2011], *Ozawa et al.* [2012], and *Pollitz et al.* [2011] are all using inland GPS plus seafloor observations, but they obtain quite different locations of maximum slip and moment magnitude. Most studies show maximum slip near E143°, N38°, but some results are shallower (e.g. *Ozawa et al.* [2012]), some are deeper(e.g. *Pollitz et al.* [2011] without seafloor). Usually results using tsunami data show large trench slip (e.g. *Yokota et al.* [2011]). Results from *Pollitz et al.* [2011] and *Simons et al.* [2011] don't show trench slip. Detailed results of the abovementioned summarized in Appendiex C.

The results variety is mainly due to the fact that the geometry of the geodetic observations are poor; all geodetic observations are located on one side of the trench and inland GPS observations are far from the epicenter. In order to get reasonable results, researchers have to regulate the problem, or equivalently, imposing a priori information, where subjectivity plays the major role and thus allow different authors produce various results depending on their own judgment and preference. In the results part of this section, I will show how these factors could affect slip inversion results. A minor reason for result variety is because of different model choosing. For example, spherically earth model versus flat earth model,

with or without considering lateral heterogeneity(trench geometry), etc.

3.3 Data

Onshore GPS time series are fitted using preseismic and postseismic models to extract coseismic and postseismic displacements. For details, please refer to Chapter 2.

Although a great amount of GPS observations has been obtained for the 2011 Tohoku earthquake, the spatial distribution of these data is not optimal. Almost all GPS stations are located on the hanging-wall side of the thrusting fault. Furthermore, distances of stations to the epicenter and the trench are far (the distance of the closest station to the epicenter is $\sim$ 75km, and to trench $\sim$200km). In the practical inversion, the geometry has low resolution on the fault segments that are near the trench. Therefore, seafloor geodetic observations are also used in this study. Because of the seafloor stations location above the source region, they become very valuable in improving the geometry of the inversion problem. Several studies have reported that including seafloor observations can significantly improve model resolution, e.g. *Iinuma et al.* [2012]. *Ozawa et al.* [2012] shows that inverted maximum coseismic slip has been greatly increased by including seafloor observations. *Pollitz et al.* [2011] using a spherical earth model suggests that more coseismic slip details can be recovered with seafloor observations. In this study, we also include seafloor observations and evaluate their role in determining coseismic slip. Table 3.1 shows the data we used in this study.

3.4 Fault and earth model

The fault model is based on Slab1.0 [*Hayes et al.*, 2012]. The cross section of the fault is shown in Figure 3.1. Three 700-km-long planar surfaces striking 195°are connected to form the whole fault. The upper and lower edge depths are fixed at 3 km and 45 km, respectively. The dip is progressively steeper with greater depth: 7.7 °from 3 to 21 km, 14 °from 21 to 39 km, and 22 °from 39 to 57 km depth.

Slip on the fault is assumed to have the same rake direction. For the 2011 Tohoku earthquake, a lot of studies assume slip rake is 90 °. However, since the rake angle is the angle between slip and the strike direction, and the strike angle of the fault model in this study (195°here) has a certain degree of uncertainties, the rake angle therefore bare some uncertainties, as well. In order to accommodate the error in the strike direction and allow more flexibility in the slip model, we use an nonlinear scheme called Occam's algorithm (for details, please see A.2) to incorporate nonlinear parameters into the inversion. Thus slip rake will be inverted for as a nonlinear parameter along with coseismic fault slip as linear parameters. Because Occam's inversion is an iterative method, initial values are required to start the iterations. In this study, 90 °is used as the initial value of rake, and the coseismic slip obtained by linear inversion with rake 90 °as the initial value of coseismic slip.

The Earth model is based on PREM [*Dziewonski and Anderson*, 1981]. The density, bulk modulus and shear modulus changing along depth is shown in figure 3.3.

Green's functions which relate the slip on the fault to static surface displacement are computed using the method proposed by *Pollitz* [1996]. The method is based on the spherical harmonic decomposition on a spherically symmetrical earth

geometry. Therefore, it can be used to study deformation that are very far from the epicenter. In this study, the farthest station we include is ULAB, which is over 3000 km away from the epicenter. Figure 3.4 is plotted without vertical exaggeration showing that the spherical effect of the earth cannot be ignored for studying deformation at far distance.

3.5 Inversion

The thorough mathematical treatment of the linear and nonlinear inversion methods used in this part is described in Appendix A. Here we only introduce the main idea and the specific model setup.

Regardless of the only nonlinear parameter, rake of slip r, the linear form of the inversion for coseismic slip can be formulated as

$$\min_{\mathbf{m}} \left\{ \|\mathbf{WGBm} - \mathbf{Wd}\| + \sum_i \alpha_i \|\mathbf{L}_i\mathbf{Bm}\| \right\} \tag{3.5.1}$$

(Appendix Equation (A.1.2)), where $\mathbf{G}$ contains Green's functions, $\mathbf{m}$ is the model parameters, and $\mathbf{d}$ is the GPS observations. The matrix W in Equation (3.5.1) is the weighting matrix. Following *Ozawa et al.* [2011, 2012], the weighting ratio for horizontal : vertical displacements of onshore GPS observations is chosen to be 5:1. The weightings of seafloor observations are varied to evaluate their effects on deciding slip results. The matrix B is called basis matrix, whose column vectors form the basis of the fault slip vectors (the fault slip vector $s = \mathbf{Bm}$). We use B-spline functions introduced in *Yabuki and Matsu'ura* [1992] as the bases.

The second term of Equation (3.5.1) is the regularization term, where three kinds of regularization [*Iinuma et al.*, 2012] are considered: 0th order regularization

(damping), 2nd order regularization (smoothing), and boundary regularization. Each kind of the regularization will introduce a hyperparameter α_i, the value of which is decide empirically based on L-curve method.

Ultimately, by using a nonlinear inversion method, Occam's algorithm, we incorporate the nonlinear parameter r into the inversion Equation (3.5.1) (Appendix A.2). Occam's algorithm is a method based on Newton's method for minimization, where the minimum value is iteratively approximated based on the information provided by derivatives with respect to model parameters. Here the derivatives of the misfit with respect to nonlinear parameter r is estimated by numerical differentiation.

3.6 Results

Occam's inversion converges fast in our model: after only two or three iterations, the rake value is stabilized at ∼83 °. How seafloor observations affect the inverted rake value is tested. The inverted rake remains at 83 °while the weighting ratio between seafloor and onshore observations are varied from $2:1$ to $0:1$ (Number 0 means seafloor observations are not considered).

The resulting slip distribution is shown in Figure 3.7a, corresponding to a geodetic moment of $5.88 \times 10^{22} Nm$ ($Mw = 9.18$). The maximum slip, over 40 m, is located at the updip direction of the epicenter of the Global CMT solution and breaks through the trench. Corresponding model fits to GPS data are shown in Figures 3.5 and 3.6.

The importance of the offshore GPS data is shown in Figure 3.7b, which presents

alternative inversion results. Comparing parts (a) and (b) which use all data and only land data, respectively, slip inversions which do not account for the offshore GPS tend to have larger maximum slip and moment magnitude. This result is also confirmed by *Ozawa et al.* [2012] and *Nishimura et al.* [2014].

3.7 Discussion

3.7.1 Ill-conditioned problem - Poor data geometry and low model resolution

Although unprecedented GPS observations have been collected for the 2011 Tohoku earthquake, there is one important defect of these data: the spatial distribution of the observation is poor, which make the coseismic inversion problem of the 2011 Tohoku earthquake an ill-conditioned problem. This ill-conditionedness is the major reason why many geodetic inversion results disagree with each other on many important physical parameters about this earthquake (See the review section). For example, geodetic inverted magnitude of the earthquake ranges from 9.0 to 9.2. Maximum slip ranges from 20 m to near 70 m. The location of maximum slip and spatial distribution of slip also varies a lot between different studies.

Researchers have combined different kinds of data to overcome the geometric defect. For example, using tsunami data with onshore GPS data can increase the resolution near the trench. However, when datasets with different nature are combined, another important problem is emerged: How should these datasets be weighed properly in the inversion algorithm to reflect their relative importance?

Some studies choose the weighting parameters empirically, and the others treat weighting parameters as unknown parameters that are included in the inversion.

In the situation of combining seafloor observation with onshore GPS observations, our experiments show that if the true relative accuracy (50:1, according to *Sato et al.* [2011]) is used, because the sparsity of the seafloor observations, the inverted slip result is almost the same as the results with onshore observations only. In other words, if we want the influence of seafloor observations be explicit in slip inversion results, large weights have to be assigned to them.

Understanding the root of these discrepancies is important to understand the limit of the data and method. This understanding is also the basis of our interpretation of various results. It draws limits for us in how much we can trust our data and method, and it tells us how to interpret variable inversion results and what part of results can be trusted to what extent.

3.7.2 Seafloor observations

Seafloor observation errors are about 50 to 60 times larger than those in regular campaigns [*Sato et al.*, 2011]. In the situation we considered in this work, seafloor GPS observations are very important for improving geometry of this inversion problem. Since there are no other observations above the epicenter, it is reasonable to give more weights on seafloor observations than that is implied by formal error. Figure 3.8 $\sim$ 3.11 show how different weightings between inland and seafloor GPS observations affect inverted coseismic slip. Figure 3.12 shows that while standard deviation of seafloor observations is increased, the RMS misfit of seafloor observation changes dramatically. However, the RMS misfit of inland GPS decreases only

slightly. Figure 3.13 shows that seafloor observations can bring down the inverted moment of slip.

3.7.3 Regularization

Because the problem is ill-conditioned in nature, we need regularization techniques to get physically reasonable results. Using regularization is equivalent to making assumptions about the final slip results, or imposing a priori information on the slip. For coseismic slip, often used regularization include 2nd order regularization (smoothness of slip) [*Yabuki and Matsu'ura*, 1992], 0th order regularization (magnitude of slip)[*Evans and Meade*, 2012]. Some authors used combined regularization method [*Iinuma et al.*, 2012]. Another often used regularization is boundary regularization, which often implied in literature but as shown below, is very important in the coseismic inversion of Tohoku earthquake because of the special model geometry of this earthquake.

0th order and 2nd order regularization

For the particular geometry of 2011 Tohoku earthquake, since the stations are all on one side of the faults, 2nd order regularization requires the slip as smooth as possible, therefore, slip tend to appear on the far edge of the fault. On the contrary, 0th order regularization requires slip as small as possible, thus slip tend to appear closer to stations, because when the slip is more close to the stations, they are more effective in generating displacements. The 2nd and the 0th order regularizations imply opposing strategies that affect the spatial distribution of coseismic slip. Also, with 2nd order regularization, the moment magnitude tend to be larger than 9.2.

On the other hand, with 0th order regularization, moment can be bring down close to 9.0.

Boundary regularization

For geodetic inversion of the 2011 Tohoku earthquake, because all observations are all on one side of fault, using boundary regularization on the trench is very important. The leftmost columns of Figure 3.8 $\sim$ 3.11 show the situation using 2nd regularization without boundary regularization. All the slip tend to concentrate on the boundary of the fault model, where the resolution is very low. Note the fault model is actually stretched out of the trench and on the edge there should be no slip. In the method proposed by *Yabuki and Matsu'ura* [1992], which is employed by *Ozawa et al.* [2011, 2012], boundary regularization is implicitly imposed by the fact that the maximum slip of the B-spline basis functions cannot appear on the edge of the fault model. *Iinuma et al.* [2012] explicitly states the boundary condition for regularization.

3.7.4 Large scale deformation

Figure 3.14 presents the predicted vertical deformation. Part a of the figure shows the predicted value, indicating large subsidence along the Pacific coast and slightly uprise along the Japan Sea coast, which is consistent with the observation (Figure 2.6). Part b shows the absolute value of the predicted vertical displacements. Considering that the vertical sensitivity of GPS is $\sim$4 mm, it confirms what we found in the previous chapter that vertical offsets are mainly detectable at stations located at the northern Honshu area (mainly Tohoku, part of Chubu and Kanto).

While GPS visible vertical deformation is confined in northern Honshu, the horizontal displacements are extensive. Figure 3.15 reveals the predicted spatial decay of the magnitude of the coseismic horizontal deformation, which is consistent with the observation (Figure 2.8).

3.8 Conclusion

Coseismic offsets from over 1300 onshore GPS stations and several seafloor sites are used to invert the coseismic slip of the 2011 Tohoku earthquake. The best rake angle of the coseismic slip is estimated as 83 °with a nonlinear inversion algorithm called Occam's Inversion. Various published coseismic slip results are reviewed, and based on our own method, we discussed factors that can affect the inverted slip results, such as the impact of seafloor observations and different kinds of regularizations. Predicted coseismic offsets in South Korea and China are compared with published observations. The results show that while the vertical movement can only be observed in Japan, the horizontal movement is very extensive and can be captured in area as far as over 3000 km away from the epicenter.

Station Code	Date of observation (UTC)		Coseismic Displacement[a] (m)		
	Pre-Tohoku Earthquake	Post-Tohoku Earthquake	Easting	Northing	Vertical
GJT3	1 Nov 2005	11 April 2011	29.5 ± 0.5	-11 ± 0.5	3.9 ± 0.5
GJT4	11 Apr 2010	11 Apr 2011	14 ± 1	-5 ± 1	N/A
MYGI	21 Feb 2011	28 Mar 2011	$22.1 \pm \alpha$	$-10.4 \pm \alpha$	$3.1 \pm \alpha$
MYGW	21 Feb 2011	28 Mar 2011	$14.3 \pm \alpha$	$-5.1 \pm \alpha$	$-0.8 \pm \alpha$
FUKU	23 Feb 2011	29 Mar 2011	$4.4 \pm \alpha$	$-1.7 \pm \alpha$	$0.9 \pm \alpha$
KAMN	16 Nov 2010	3 Apr 2011	$13.8 \pm \beta$	$-5.8 \pm \beta$	$1.6 \pm \beta$
KAMS	19 Nov 2010	5 Apr 2011	$21.1 \pm \beta$	$-8.9 \pm \beta$	$1.5 \pm \beta$

[a] $\alpha = 0.1 \sim 0.2$ and $\beta = 0.5 \sim 0.6$.

Table 3.1: Date of observations and estimated coseismic displacements at GPS/A stations after *Iinuma et al.* [2012].

Reference	Data	Moment (Nm)	Mw	Max Slip (m)
Ozawa et al. [2011]	Onland GPS	3.43E22	9.0	27
Ozawa et al. [2012]	Onland and seafloor GPS	3.43E22	9.0	~ 60
Pollitz et al. [2011]	Onland and seafloor GPS	4.06E22	9.0	33 (onland GPS)
Yokota et al. [2011]	Strong motion, teleseismic, geodetic, tsunami	4.2E22	9.0	35
Ito et al. [2011]	Onland and seafloor GPS	4.16E22	9.0	60
Simons et al. [2011]	Onland and seafloor GPS	-	$8.8 \sim 9.2$	$\sim$60
Minson et al. [2014]	Onland and seafloor GPS, tsunami data	-	9.2	$\sim$80

Table 3.2: Coseismic slip obtained from geodetic inversion summarized.

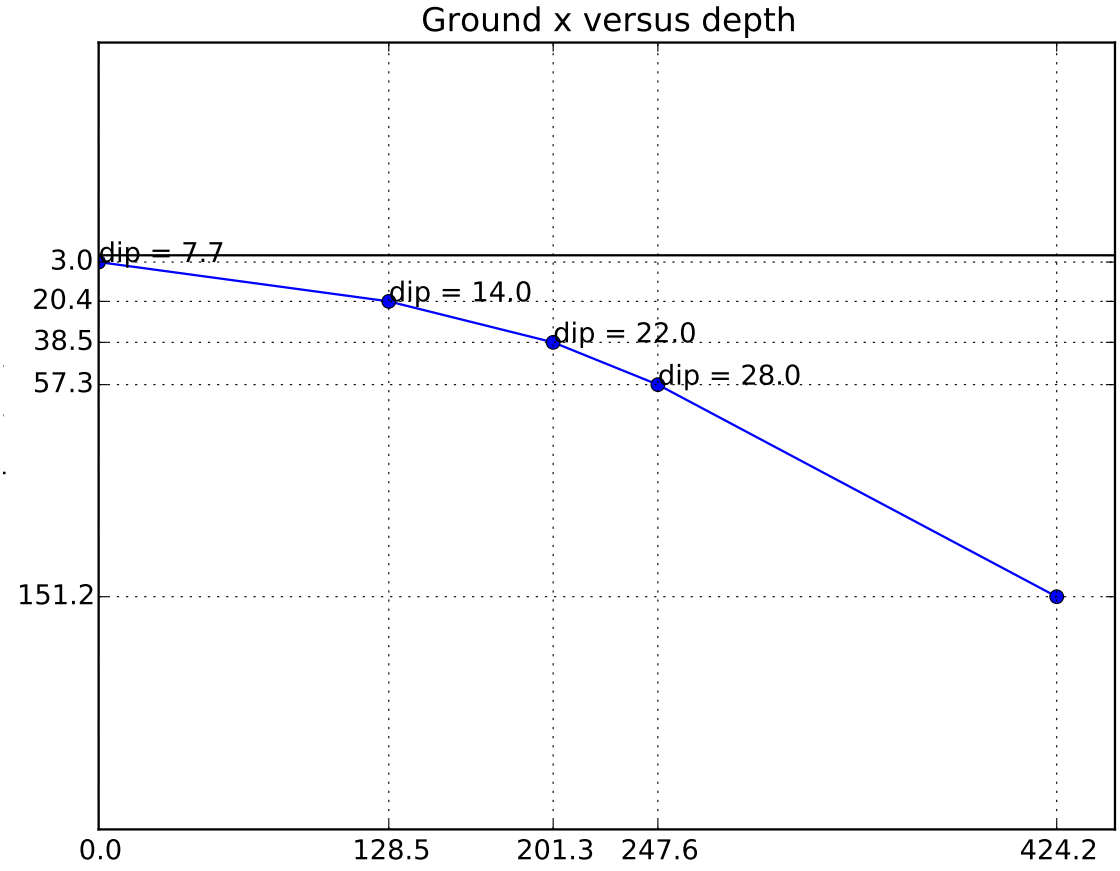

Figure 3.1: Cross section of the fault model.

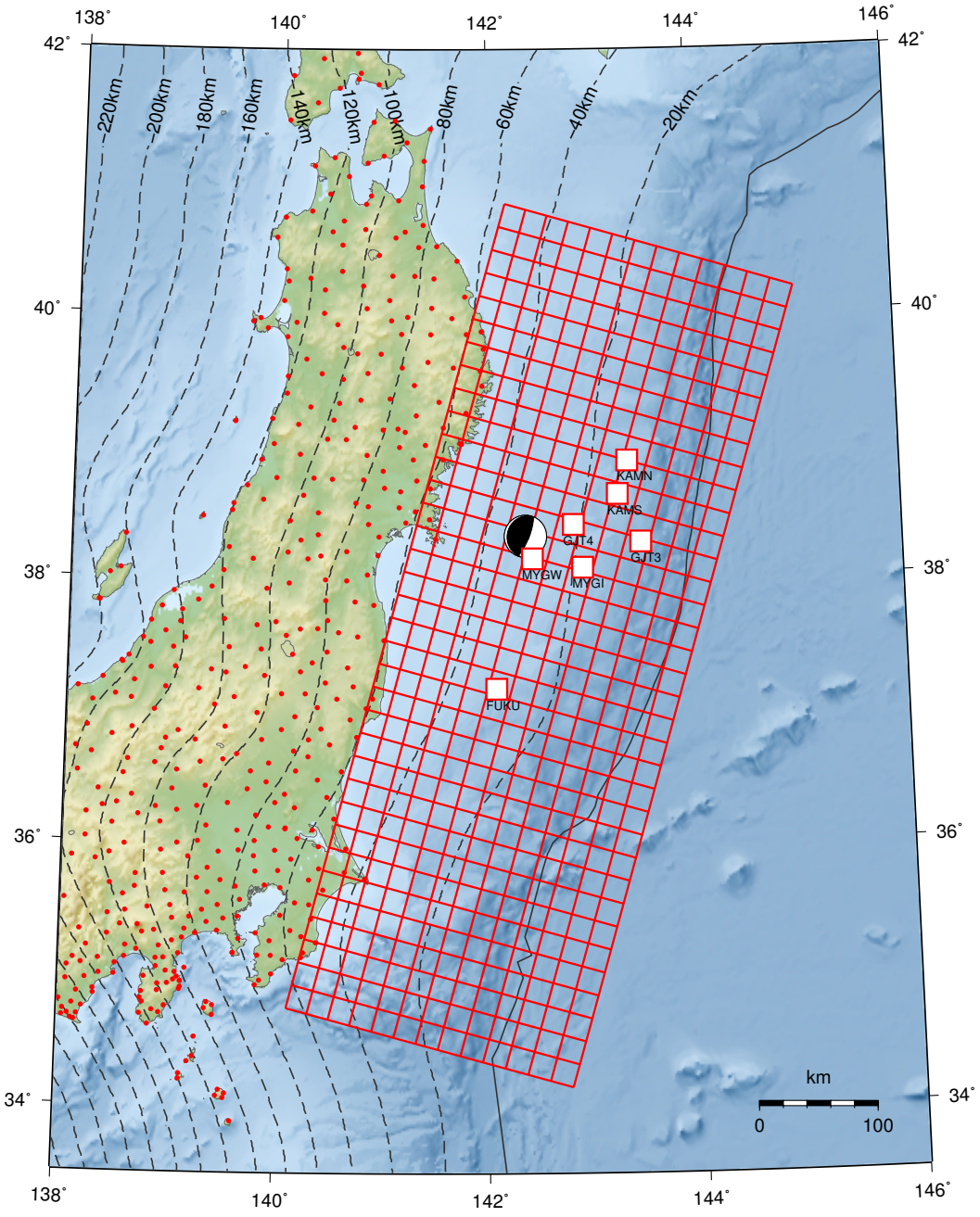

Figure 3.2: Fault model in a map view.

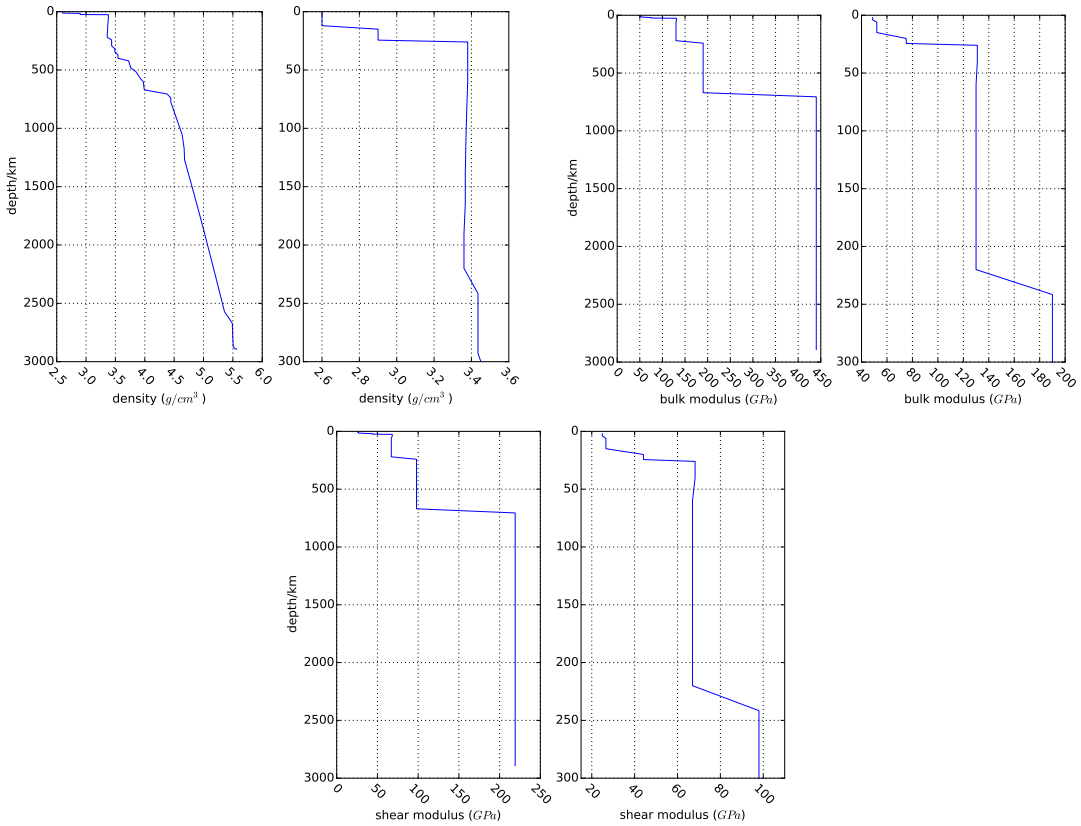

Figure 3.3: Properties of the Earth model along depth, following PREM.

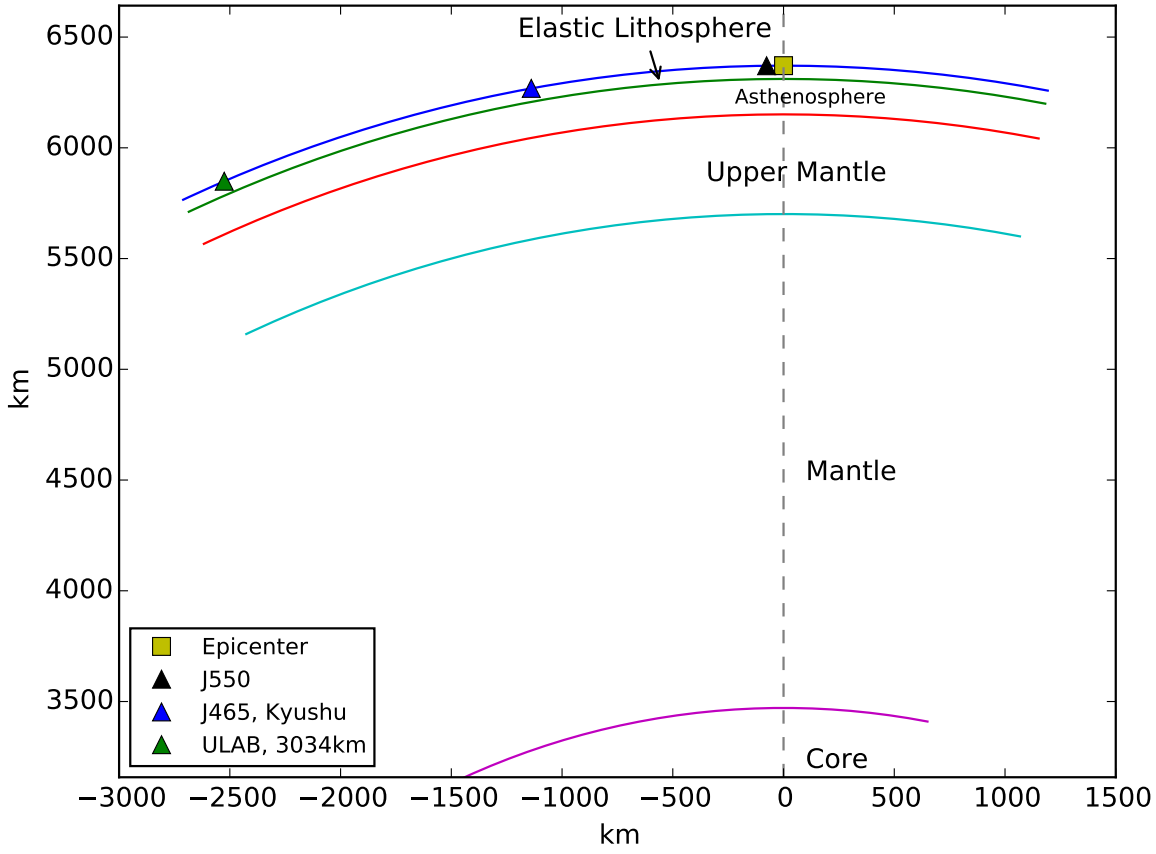

Figure 3.4: Model geometry and spherical effect. The dotted line is a radius line of the spherical Earth passing through the epicenter.

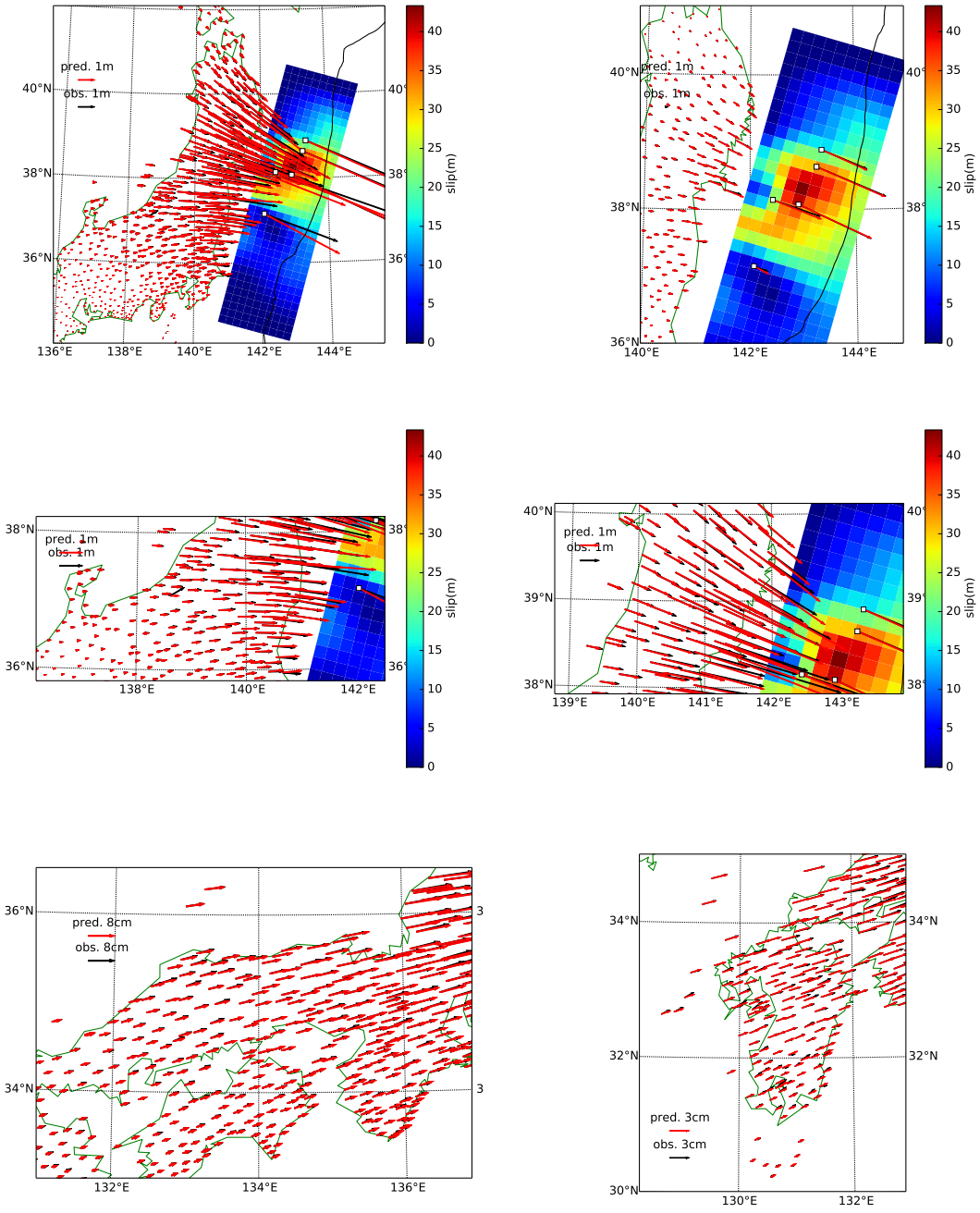

Figure 3.5: Predicted versus observed displacements.

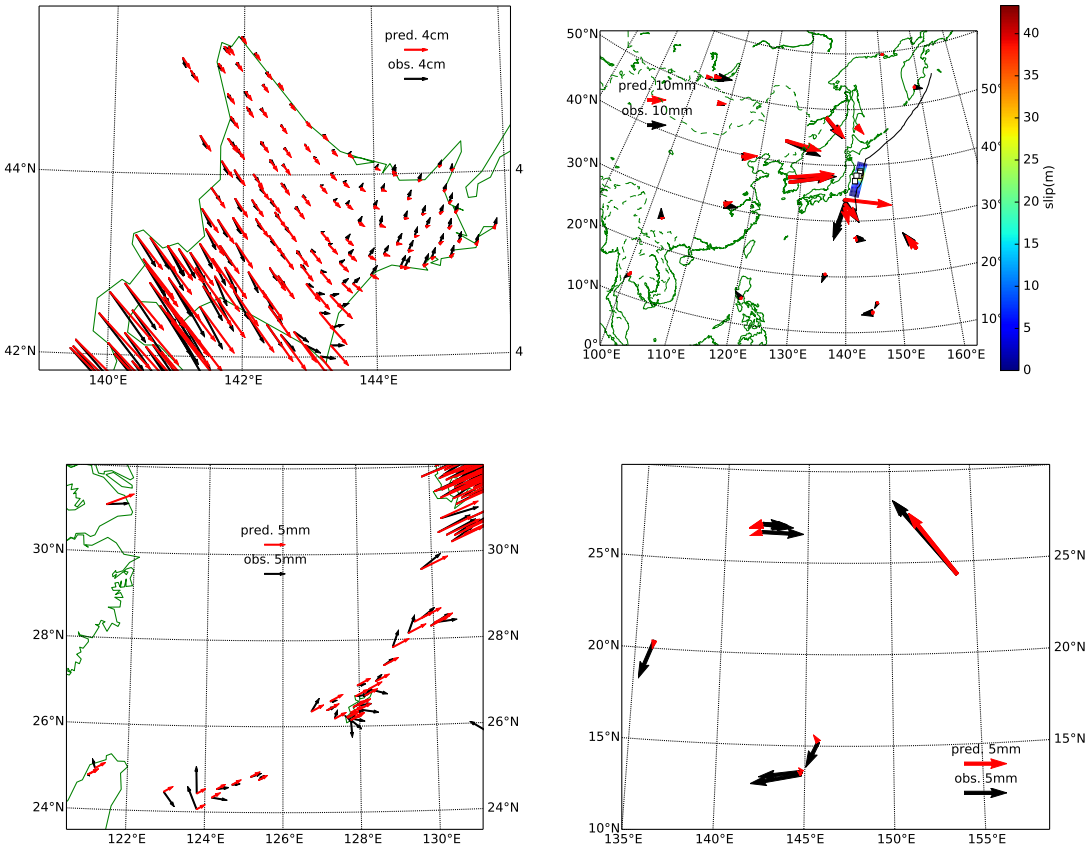

Figure 3.6: Continued.

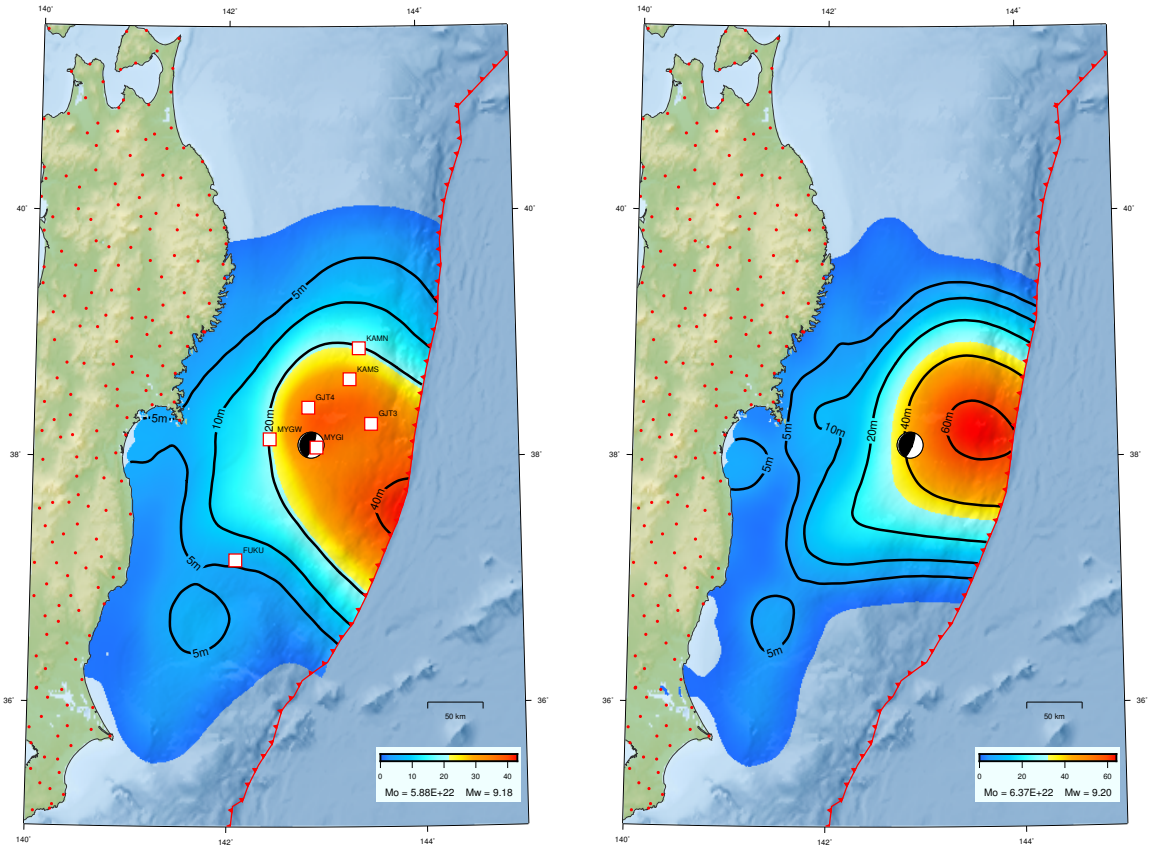

(a) With seafloor observations, which are marked by white squares, weighted one time larger than onshore stations.

(b) Without considering seafloor observations.

Figure 3.7: Inverted coseismic slip. Moment mechanism and location of the epicenter is from Japan Meteorological Agency. Red dots are onshore GPS stations. Black lines are slip contours.

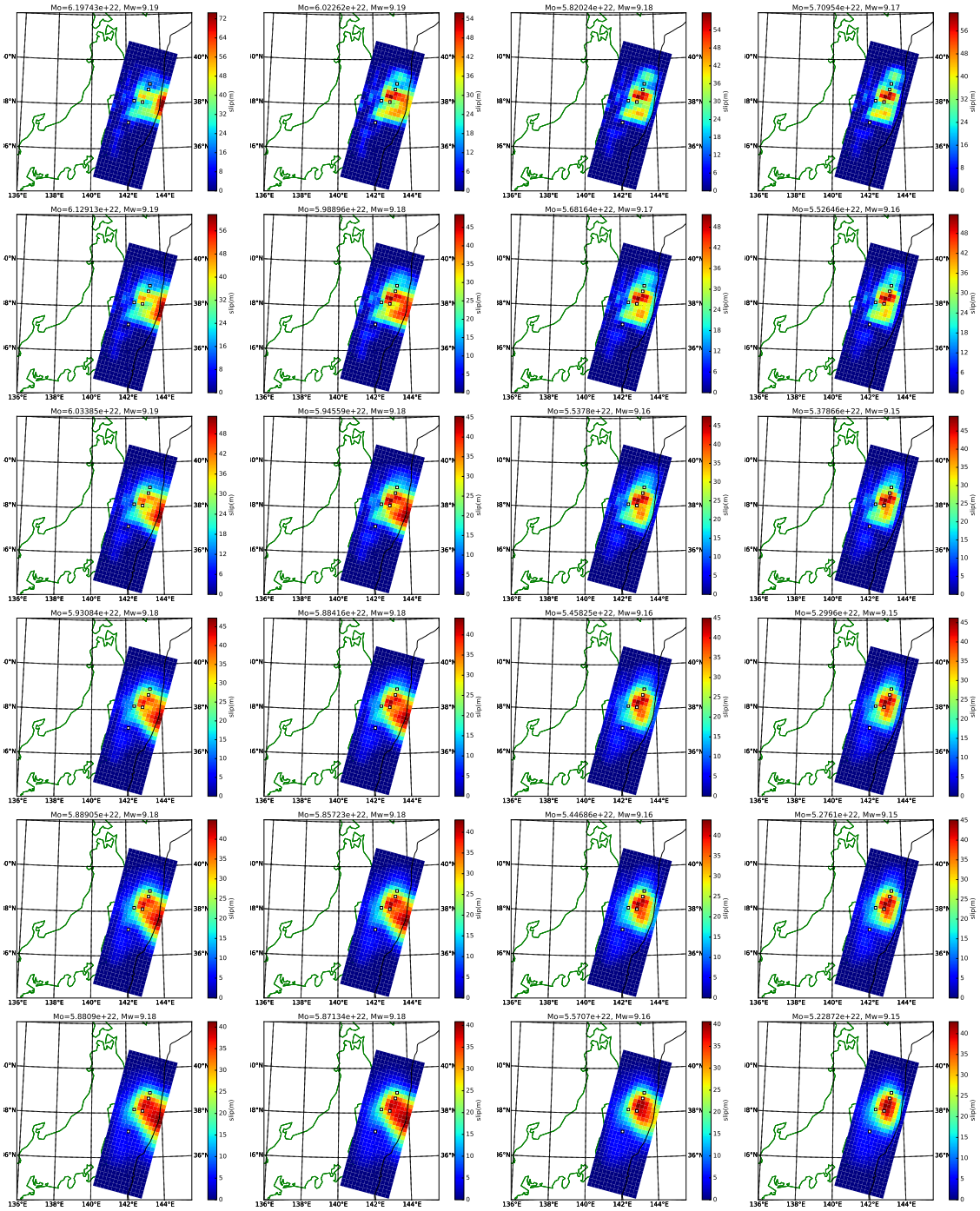

Figure 3.8: Inverted coseismic slip with different regularization parameters. The weighting ratio between seafloor and onshore observations is 1:1 in this plot. ($W_{\text{seafloor}} : W_{\text{onshore}} = 1 : 1$). From the top to the bottom, the roughening parameter increases. From the left to the right, the top edge regularization parameter increases. Each subfigure is plotted with different color scale, and the maximum slip of each subfigure is indicated by the upper boundary of the color bar associated with that subfigure. Seafloor stations are marked with white squares.

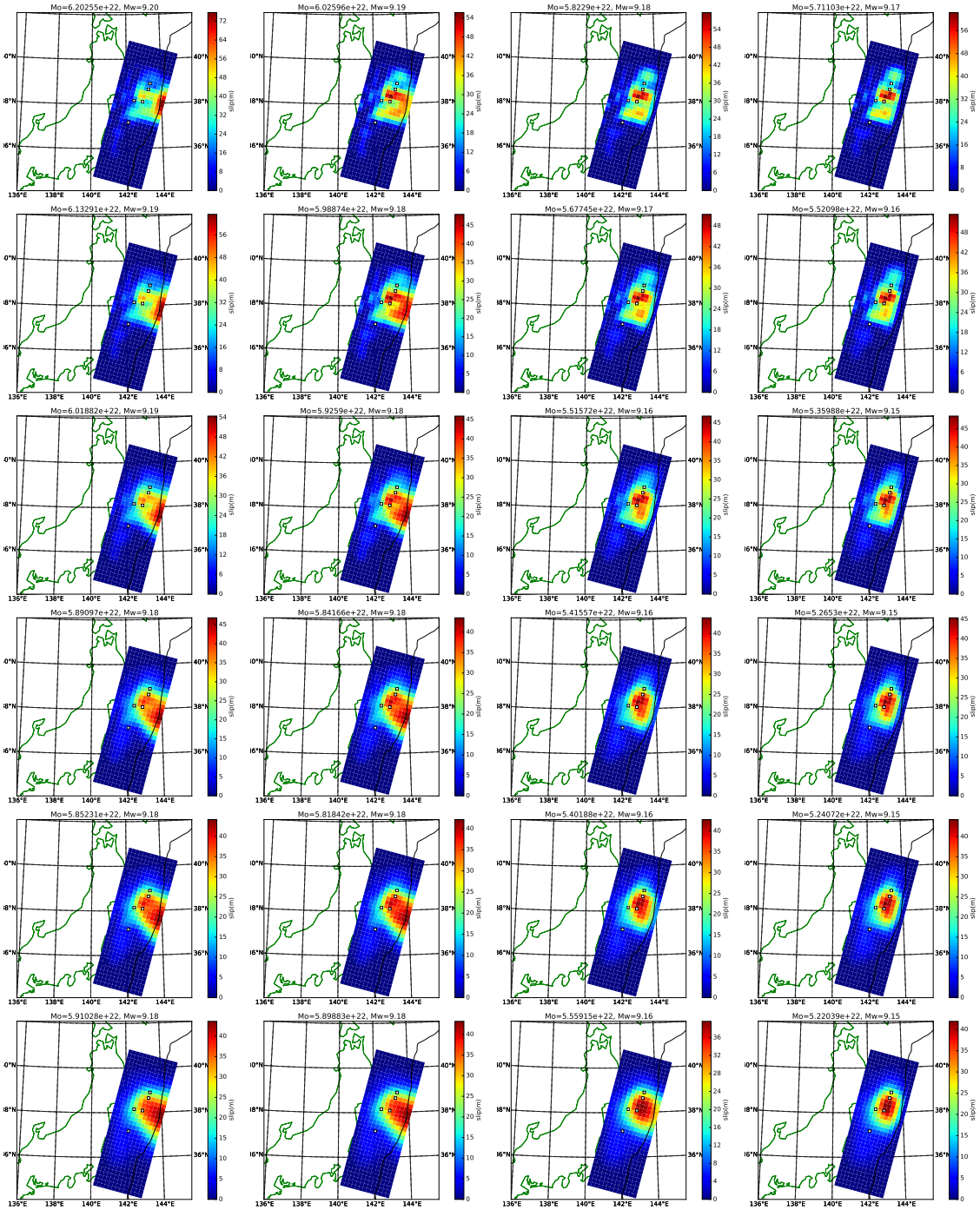

Figure 3.9: $W_{\text{seafloor}} : W_{\text{onshore}} = 1/2 : 1$. The rest of information is the same as Figure 3.8.

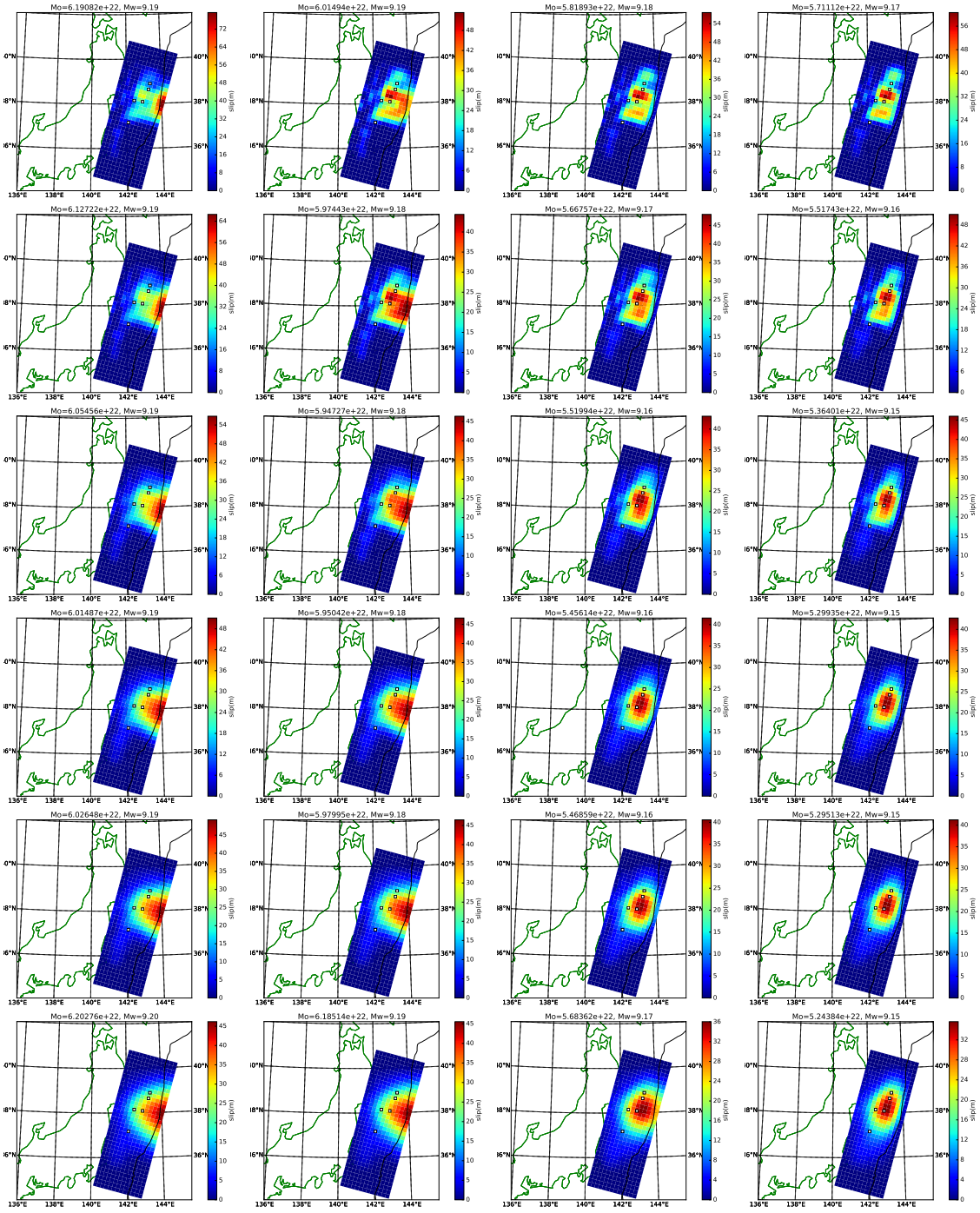

Figure 3.10: $W_{\text{seafloor}} : W_{\text{onshore}} = 1/10 : 1$. The rest of information is the same as Figure 3.8.

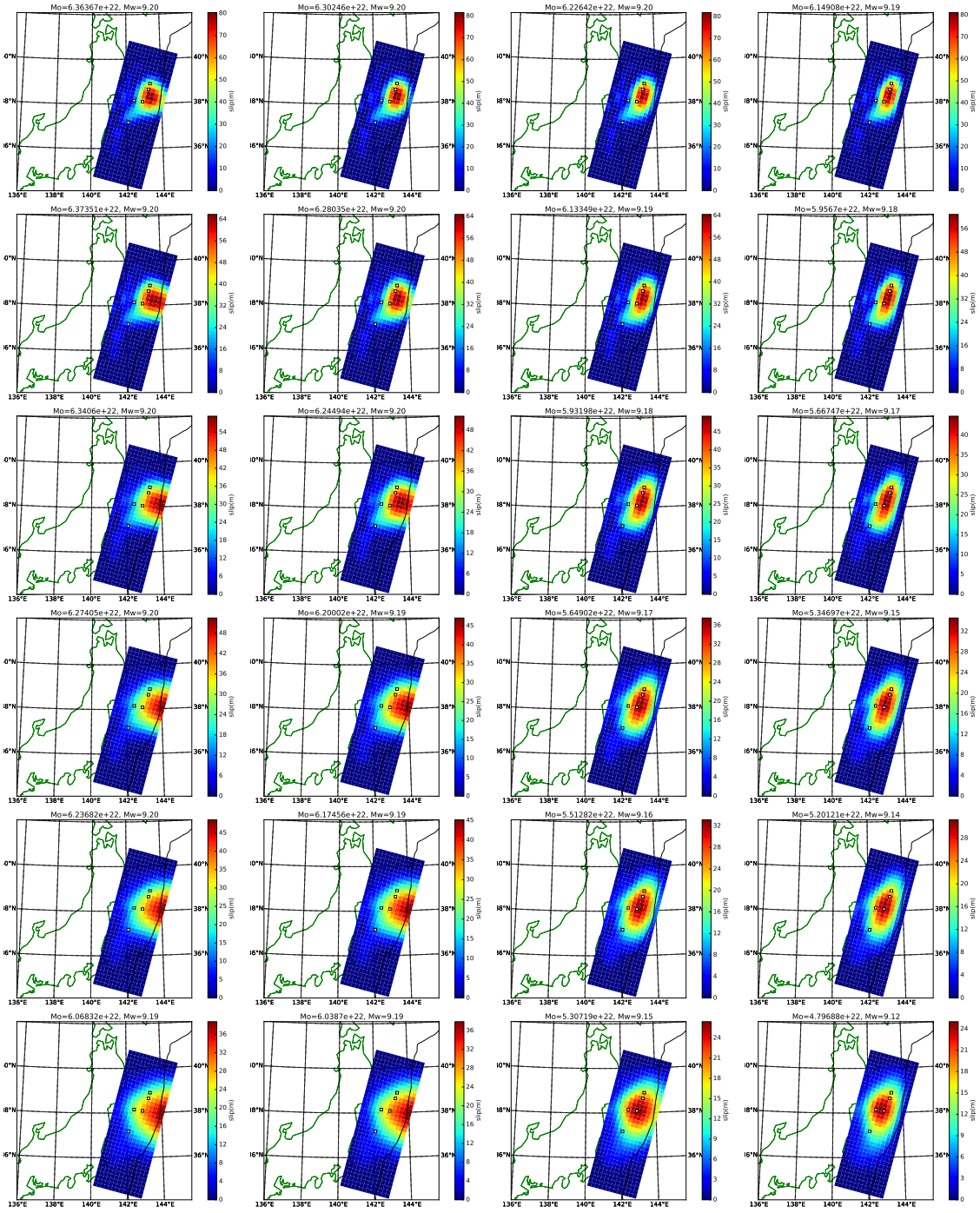

Figure 3.11: $W_{\text{seafloor}} : W_{\text{onshore}} = 0 : 1$. The rest of information is the same as Figure 3.8.

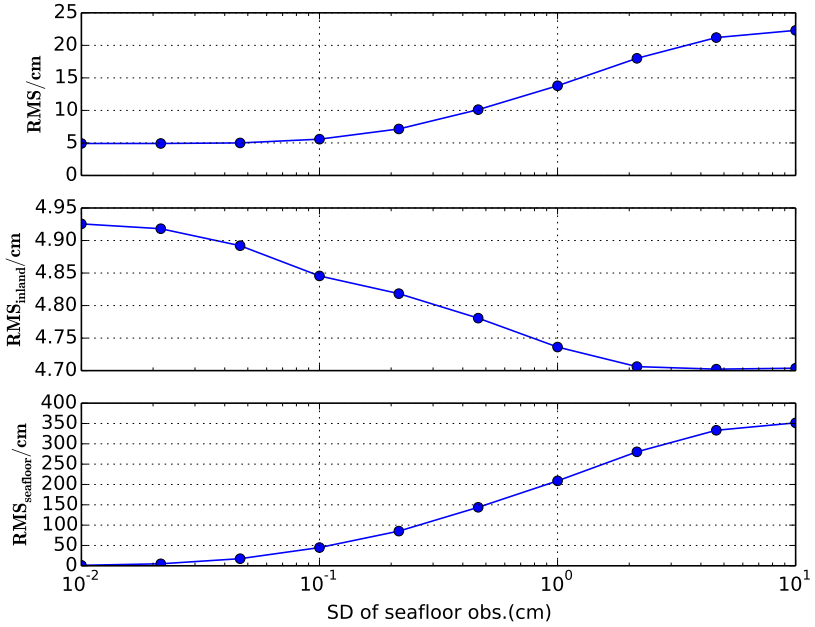

Figure 3.12: Change of standard deviation of seafloor observation versus RMS misfit.

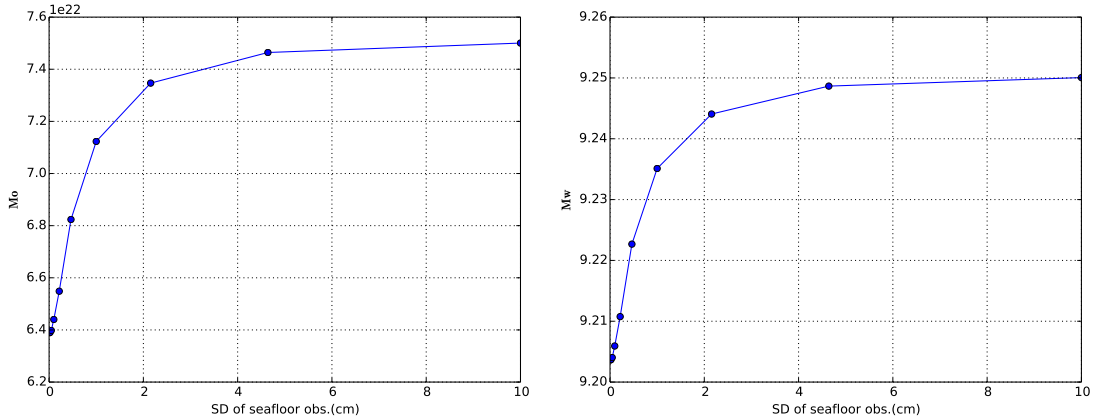

Figure 3.13: Inverted moment (left) and moment magnitude (right) with different standard deviation of seafloor observation.

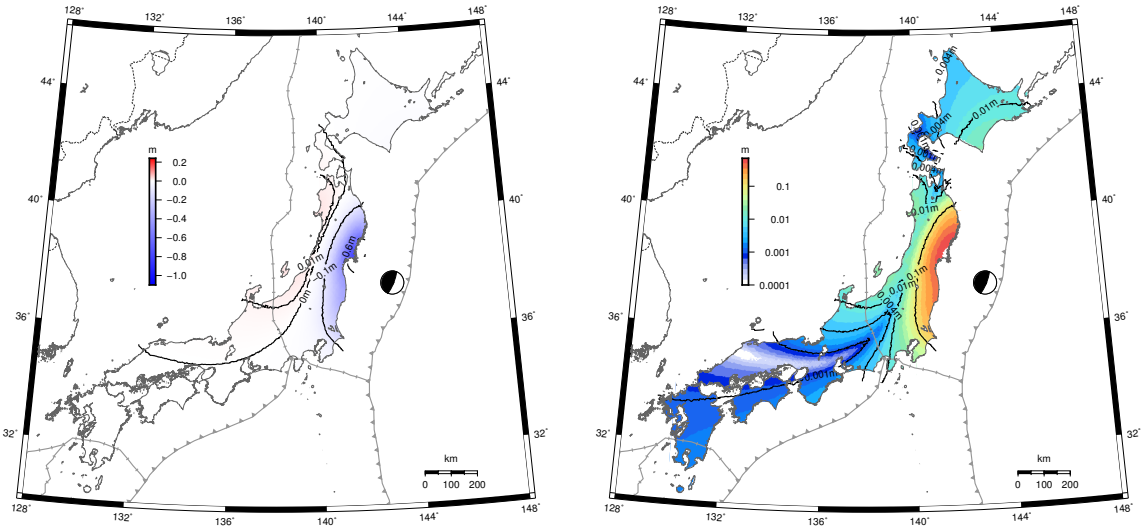

(a) Vertical deformation.

(b) Absolute value of vertical deformation plotted in logarithm scale.

Figure 3.14: Predicted vertical deformation.

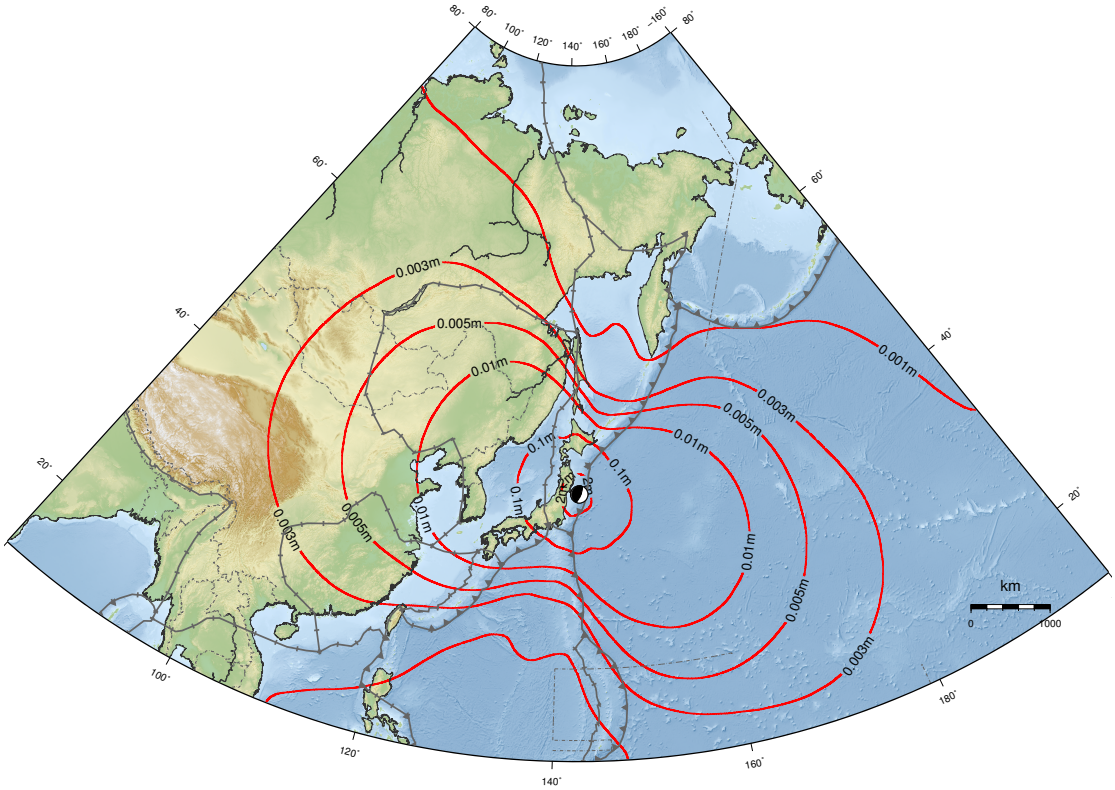

Figure 3.15: Decay of predicted horizontal displacements.

CHAPTER 4

POSTSEISMIC DEFORMATION ANALYSIS: SIMULTANEOUS AFTERSLIP AND VISCOELASTIC RELAXATION PARAMETERS INFERRED FROM NON-LINEAR INVERSION OF GPS DATA

4.1 Introduction

Large earthquakes are followed by transient deformation of the crust over days to years, which is usually referred to as postseismic deformation. Three mechanisms have been proposed to explain this deformation: afterslip, the creeping movement on the fault plane after instantaneous coseismic rupture [*Marone et al.*, 1991; *Perfettini*, 2004, 2005]; viscoelastic relaxation, viscous lower crust and uppermost mantle releasing the stress caused by coseismic slip [*Nur and Mavko*, 1974]; and poroelastic rebound, the deformation induced by pore fluid flow in porous rocks that are deformed by the coseismic stress change [*Peltzer et al.*, 1996, 1998].

A fundamental challenge in postseismic deformation study lies in the multitude of relaxation processes that follow earthquakes. A common view is that the initial fast trend after the earthquake is dominated by afterslip and viscoelastic relaxation is important in the longer trend. Poroelastic rebound is considered as a localized effect, and thus not considered in this thesis.

Postseismic deformation has been observed following the 2011 Tohoku megathrust. Studies have been published in deciding the nature of this deformation. For short time postseismic deformation, most of the earliest studies assume that afterslip is the only mechanism. However, more and more studies realized that viscoelastic relaxation is very important even in the earliest stage of the postseismic

deformation [*Sun et al.*, 2014; *Han et al.*, 2014].

For a large megathrust such as the 2011 Tohoku earthquake, more plausible senario is that viscoelastic relaxation and afterslip co-occur after the mainshock. An ideal model should consider the coupling effect of afterslip and viscoelastic relaxation. *Lubis et al.* [2012] considers the coupled effect for the 2007 Sumatra earthquake. *Diao et al.* [2013] uses a flat earth model to consider the coupled effect for the 2011 Tohoku earthquake for up to ~ 1.5 yr following the main shock. Recent study by *Yamagiwa et al.* [2014] uses the so-called viscoelastic Green's function to decouple the deformation of afterslip and viscoelastic relaxation.

In this study, we develop an integrated model to study the coupled effects of viscoelastic relaxation and afterslip of the 2011 Tohoku earthquake. We employed a spherical layered Earth model and use over 5 years GPS observations from more than 1300 onshore stations, as well as about 3 years GPS/A observations from 6 seafloor stations. An nonlinear inversion method, Occam's algorithm, is employed to invert all these observations for not only the slip history over 3.6 years after the mainshock, but also three nonlinear parameters including the elastic depth, the Maxwell viscosity of lower crust and uppermost mantle, and the rake of slip. The relative magnitudes of different mechanisms of postseismic deformation are also decided.

4.2 Data

We use GPS data mainly from GEONET onshore stations (Figure 2.1), plus several IGS stations at far-field. Daily time series 2 yr before and 3 yr after the 2011 Tohoku earthquake are used to construct time series models. The preseismic time series

model includes a secular linear term accounting for interseismic strain accumulation phase, as well as periodic terms accounting for seasonal and semi-seasonal movement. The postseismic time series are modeled with either two exponentially decaying terms for near-field stations, or one exponentially decaying term for far-field stations Coseismic and postseismic offsets are calculated from the time series models. For details of time series modeling, see Chapter 2.

Former studies have revealed that GPS-Acoustic (GPS/A) observations play an important role in deciding viscoelastic relaxation deformation and afterslip distribution of the earthquake [*Sun et al.*, 2014; *Yamagiwa et al.*, 2014]. In this study, we employ GPS/A coseismic offsets published in *Sato et al.* [2011] and GPS/A postseismic offsets published in *Watanabe et al.* [2014]. (For names and locations of these GPS/A stations, see Figure 4.1.) Similar to inland observations, postseismic offsets of GPS/A observations are modeled with a two-exponential decaying term (Model 2EXPs in Section 2.2), so that postseismic offsets can be obtained at any time after the mainshock.

4.3 Earth and fault model

We employ a spherically layered Earth structure [*Pollitz*, 1992, 1996, 1997]. Figure 4.3 shows the physical properties of the Earth model along depth, where the density, the bulk modulus and the shear modulus all follow the PREM model [*Dziewonski and Anderson*, 1981]. The viscoelastic structure of the Earth model (Figure 4.3d) is similar to that of *Pollitz et al.* [2006]. The top layer with infinite viscosity represents the elastic lithosphere. Its bottom depth H_e is one of the undetermined non-linear parameters. The second layer is from depth H_e to 200 km representing

the lower crust and the uppermost mantle. Its viscosity η is another undetermined nonlinear parameter. The next layer from 200 km to 670 km represents the viscoelastic upper mantle, with the viscosity of $10^{20} Pa \cdot s$. The bottommost layer from 670 km to 2891 km represents the lower mantle, with the viscosity of $10^{21} Pa \cdot s$.

Figure 4.1 is a map view of the fault model. The fault model is composed of 28 (along strike) $\times$ 12 (along dip) square subfaults with the length of 25 km and the strike of 195 $^\circ$. The dip of each subfault gradually varies along dip direction from 7.7 $^\circ$to 28 $^\circ$(Figure 4.2). The depth of the bottom of the fault is 75 km. Two constraints are imposed on both coseismic and postseismic slips: (1)all slips are non-negative (reverse slips only), and (2) all slips have the same rake angle. We solve for the magnitudes of slips, which are linear parameters, as well as the rake angle, which is a nonlinear parameter.

Altogether, beside coseismic slip and afterslip as linear parameters, we also invert for three nonlinear parameters. Two of them are related to the rheological structure of the Earth: the elastic thickness of the lithosphere He and the viscosity of the lower crust and uppermost mantle η. The last one is the rake of all slips r.

4.4 Viscoelastic deformation

Detailed mathematical formulation and analysis of the viscoelastic deformation and its associated nonlinear inversion method can be found in Appendix A and B. We only brief the main ideas in this and next section.

Slip on the fault causes elastic deformation, as well as viscoelastic relaxation within the viscoelastic layers of the Earth when the layers are affected by the stress

change associated with the slip. If we treat slip on the fault as input and resulting displacements at stations as output, the slip-deformation system is linear time invariant system (LTI system), and can be described by the following formula:

$$\mathbf{d}(t) = \sum_{\alpha} \int_{-\infty}^{+\infty} v_{\alpha}(\tau)\, \mathbf{g}_{\alpha}(t-\tau)\, d\tau, \tag{4.4.1}$$

(Equation (B.1.1) in Appendix B).

The vector function $\mathbf{g}_{\alpha}(\cdot)$ in Equation (4.4.1) is the viscoelastic Green's function, which describes how the Earth structure with both elastic and viscoelastic layers responds to a unit slip impulse on the subfault α. It is a summation over two parts: the elastic deformation caused by the unit slip impulse and the viscoelastic deformation relaxing the stress change associated with the unit slip impulse. In this study, these two parts of $\mathbf{g}_{\alpha}(\cdot)$ are computed by methods described in *Pollitz* [1996, 1997] for elastic deformation, and *Pollitz* [1992] for viscoelastic deformation, respectively. The vector $\mathbf{d(t)}$ is the displacements at GPS stations, the values of which can be obtained based on time series analysis (Chapter 2). The notations $v_{\alpha}(t)$ represents slip rate on subfault α, and its time integral is the slip history on that subfault $s_{\alpha}(t)$. Equation (4.4.1) is in the form called convolution of $v_{\alpha}(t)$ and $\mathbf{g}_{\alpha}(\mathbf{t})$. Its inverse problem from $\mathbf{d(t)}$ to invert for $v_{\alpha}(t)$ is often called deconvolution. The aim of this work is to invert observation represented by $\mathbf{d(t)}$ for $v_{\alpha}(t)$ (or equivalently $s_{\alpha}(\cdot)$) based on computed values of $\mathbf{g}_{\alpha}(\mathbf{t})$, or in other words, to deconvolve Equation (4.4.1).

Based on Equation (4.4.1), we can further decompose displacements vector $\mathbf{d(t)}$ into four parts: E_{co} - elastic deformation caused by coseismic slip; E_{aslip} - elastic deformation caused by afterslip; R_{co} - viscoelastic deformation caused by coseismic slip; R_{aslip} - viscoelastic deformation caused by afterslip. Our inversion allow us to decide the magnitude of each components at each station (Appendix B.4).

4.5 Nonlinear inversion - Occam's algorithm

Although the slip history $v_\alpha(t)$ is linear according to Equation 4.4.1, we have also introduced three other nonlinear parameters He, η and r (section 4.3). Therefore, we employ a nonlinear inversion method, Occam's algorithm (*Constable et al.* [1987], *Aster et al.* [2013], and Appendix A.2), to solve for these nonlinear parameters, as well as fault slip. Occam's algorithm is an iterative method based on Newton's method for minimization. It iteratively approaches the minimum value of misfits according to the information provided by the derivatives of the misfits with respect to model parameters. In this study, the derivatives with respect to nonlinear parameters are estimated by numerical differentiation. Finally, the stability of the nonlinear inversion algorithm is tested by starting from various initial values.

Equation (4.4.1) is discretized along time, and the slips on the fault are solved episodically (Appendix B.5). In this study, we discretize the time period from 0 (the day of mainshock) to 1344 days after the mainshock into 28 epochs, where the initial 1.5 year is twice more densely discretized than the rest of time, so that the afterslip at the beginning of the postseismic period can be better resolved. Each epoch has 336 (number of subfaults) slip parameters to solve, so with 28 epochs, there are altogether 9408 slip parameters plus three additional nonlinear parameters to solve.

Three kinds of regularizations are considered for the problem: (1) the smoothness of slip on the fault (2nd order regularization) at each epoch; (2) the smoothness of temporal slip involution on each subfault; (3) the magnitude of afterslip (0th regularization). Each of these regularizations introduce a hyperparameter, the

value of which is decided through an empirical approach.

Following *Ozawa et al.* [2011, 2012], we weigh the horizontal and vertical GPS observations with a ratio of 5:1. We also weigh coseismic and postseismic displacements as 2:1, considering the fact that the postseismic deformation model contains more uncertainties than the coseismic deformation model. Although observation errors of seafloor stations are more than 10 times larger than those of inland [*Sato et al.*, 2011], we set the same weight to them, in order to stress the importance of seafloor observations in constraining near-field features. The weighting is summarized in table 4.1.

	Coseismic disp.		Postseismic disp.		Seafloor disp.	
	horizontal	vertical	horizontal	vertical	horizontal	vertical
weights	10	2	5	1	10	2

Table 4.1: Weighting on observations used in the inversion.

4.6 Results

4.6.1 Non-linear parameters

Three nonlinear parameters are inverted for in this study. Two of them describe the Earth's rheological structure: the Maxwellian viscosity of the lower crust and the uppermost mantle η and the elastic depth H_e. The other one is the rake of fault slip r. The final inverted values are $\eta = 10^{18.9} \approx 7.9 \times 10^{18} Pa \cdot s$, $He = 51km$, and $r = 83°$. Under a reasonable misfit limit, the final values of nonlinear parameters are not affected by regularization. The weighting of seafloor observations doesn't affect the values of nonlinear parameters either.

The viscosity obtained in this work is close to the value obtained by *Ohzono et al.* [2012], where the viscosity value $2.4 \sim 4.8 \times 10^{18} Pa \cdot s$ is proposed by using 2-yr continuous GPS data following the 2008 Iwate-Miyagi Nairiku earthquake. *Suito and Hirahara* [1999] estimates the viscosity of the upper mantle beneath the northeast Japan as $9.3 \times 10^{18} Pa \cdot s$. A similar study by *Diao et al.* [2013] using gird search gets the viscosity value of $2 \times 10^{19} Ps \cdot s$. However, the postseismic time period they consider is much shorter than this study.

The obtained rake of slip is close to major moment tensor solutions, for instance, USGS WPhase moment solution reports rake as 81°(strike as 193°).

4.6.2 Coseismic slip

The solved coseismic slip distribution is presented in the first subplot of Figure 4.4. The maximum slip is about 60 m and found at depths shallower than 22km. The estimated moment release is $6.71 \times 10^{22} Nm$, corresponding to the moment magnitude of 9.22, which is larger than the results of *Ozawa et al.* [2012] and *Yamagiwa et al.* [2014], but consistent with those of *Simons et al.* [2011] and *Minson et al.* [2014].

4.6.3 Afterslip

Figure 4.4 shows the slip history at different time periods. Figure 4.14 shows the total afterslip (in coutours) in 1344 days after the mainshock and its spatial relationshipe with coseismic slip (in colors). Afterslip is complementary to coseismic slip and happens in the down-dip direction to the coseismic slip patch, where most aftershocks occur. This is consistent with the results of *Diao et al.* [2013], *Yamagiwa*

et al. [2014] and *Ozawa et al.* [2012, 2013]. It is located in a belt region which is roughly aligned with the slab contour line of the depth of 40 km. The area where afterslip happens overlap with that where most aftershocks happen. Figure 4.6 presents the inverted moment and moment magnitude of afterslip along time. The total moment released by afterslip is about $1 \times 10^{22} Nm$ during the studied period (1300 days), which corresponds to $M_w = 8.67$.

4.6.4 Predicted displacements

Seafloor stations

Seafloor stations are right above the rupturing fault, thus provide crucial information about the mechanisms of the postseismic deformation. Our model's prediction at seafloor stations are generally in good consistency with the observations (Figure 4.7 and 4.14).

Figure 4.7 compares the time series of the predicted postseismic displacements caused by different mechanisms. The model predicts that viscoelastic relaxation deformation caused by coseismic slip (R_{co}) at station KAMN, KAMS, MYGI, and MYGW show significant landward movement, which is in the opposite direction to the movement caused by afterslip (E_{aslip}). Especially at station KAMS and MYGI, the landward movement is so significant that it surpasses the seaward displacements caused by afterslip, and the stations there eventually show landward movement during the entire postseismic period. *Sun et al.* [2014] interprets that the landward movement at seafloor station KAMN, KAMS, and MYGI are the evidence of viscoelastic relaxation.

Onshore stations

Figure 4.9 to 4.13 present the predicated postseismic time seris versus the observations at stations from five different regions: Honshu, Southwestern Japan, Kyushu, Hokkaido and South Korea, respectively. The locations of these stations are shown in the map of Figure 4.8. Predicted time series of deformation caused by different mechanisms are also shown. The root-mean-square (RMS) of the residuals of all onshore stations is 3.15 cm (reported RMS in *Yamagiwa et al.* [2014] is 3.56cm).

4.7 Discussion

4.7.1 Occam's algorithm

Occam's algorithm is well suited for the problem here. It converges fast. With reasonable initial values, stable results usually can be obtained within $3 \sim 4$ iterations. One drawback of Occam's algorithm is that it is a local optimization method, which means it could miss minimum values that are out of the space covered by the searching path. However, this drawback can be covered by (1) using physical properties of the object parameters to limit the searching space, and (2) testing the final results by starting the iteration from different initial values (i.e. trying various searching paths).

An alternative to nonlinear inversion is the grid search method [*Diao et al.*, 2013]. Although the grid search method can provide a relative more global view in minimization, the nonlinear inversion method has many advantages: (1) Grid search practically can handle only two nonlinear parameters, but nonlinear inver-

sion can easily handle many nonlinear parameters, as we do in this work. (2) Grid search requires that the inversion must be carried out on each grid of a possible combination of nonlinear parameters. This is a formidable task for large scale inversion problems. (3) With nonlinear inversion algorithm, it is possible to start with rougher (thus computationally faster) model, then based on the results obtained, gradually refine to better model. For example, with nonlinear inversion, we can obtain preliminary results based on models with coarser subfault grids, then use these results as the initial values for models with denser subfaults grids to get better results. On the contrary, with the grid search method, whenever model setup is changed, former results have to be discarded and inversions have to done on all grids over again with the new model setup.

4.7.2 Viscoelastic relaxation

According to previous analysis, postseismic deformation can be decomposed into three parts, (1) $E_{\mathbf{aslip}}$, elastic deformation caused by afterslip, (2) $R_{\mathbf{co}}$, viscoelastic deformation induced by coseismic slip, (3) $R_{\mathbf{aslip}}$, viscoelastic deformation induced by afterslip. An interesting question is what are the relative contribution of these three processes? The question is addressed by Figure 4.15, which shows the percentage of different mechanisms contributing to the total deformation (Part a) and deformation in each time section (Part b). Figure 4.15 shows that afterslip is dominant in the beginning of the postseismic deformation, and after about 1 year, viscoelastic deformation starts to take control of the overall deformation. Among all viscoelastic deformation, those caused by afterslip R_{aslip} is only a fraction of those caused by coseismic slip R_{co} ($\sim 20\%$ towards the end of the studied time range).

In Section 2.2, we proposed that the postseismic time series of near field stations can be decomposed into two exponentially decaying terms based on empirical time series analysis (Model 2EXPs). Figure 4.16 compares this decomposition with that is based on model prediction of different deformation mechanisms. The exponential term with a slower decaying trend and a faster decaying trend is corresponding to the viscoelastic relaxation (mainly R_{co}) and the elastic deformation cause by afterslip (R_{aslip}), respectively. Although the correspondence is not exact, but it suggests that multiple exponential terms required to fit postseismic time series can be a sign of multiple postseismic deformation mechanisms.

If we assume all the postseismic deformation is caused by only afterslip (afterslip-only model), the misfit of the model will significantly increase along time. The misfit of afterslip-only model at the day of 1344 after the earthquake is almost 2.5 times larger than the misfit of the coseismic slip model. Figure 4.17 compares the misfit of the coupled model that we study in this chapter with that of the afterslip-only model. The misfit for postseismic displacements is significantly reduced.

While coseismic slip model can successfully explain far-field coseismic displacements, afterslip-only model cannot fit the azimuth of the observation. For example, at southwestern Honshu, Part (a) of Figure 4.18 shows the observed and predicted coseismic displacements. Part (b) of Figure 4.18 shows the observed and afterslip-only model predicted displacements, where comparing with part (a), a systematic azimuthal difference exists between the prediction and observation. If the postseismic displacements is completely caused by afterslip, why the slip model cannot explain the observation as well as it does in the coseismic model? This suggests that there are other mechanism driving the postseismic deformation. Figure 4.18 (c) shows that viscoelastic relaxation and afterslip coupled model

can successfully explain the azimuthal at far-field.

Figure 4.19 shows the magnitudes and patterns of postseismic deformation caused by different mechanisms in a larger spatial scale at 1344 days after the mainshock. The viscous relaxation caused by coseismic slip (Rco, Figure 4.19b) and the elastic deformation caused by afterslip (Easlip, Figure 4.19c) have the similar magnitude within about 1300 km from the epicenter. However, the elastic deformation Easlip spatially attenuates more slowly, and reaches farther westward into the continent than the viscous deformation Rco. The viscous relaxation caused by afterslip (Raslip, Figure 4.19d) is about one magnitude smaller than the other two components, but its absolutely value still reach to centimeters level in near field at most part of Honshu. Figure 4.20 shows the long-term (5 yr, 10 yr, 15 yr, and 20 yr) prediction of the viscoelastic relaxation caused by cumulative slip.

4.7.3 Model misfits and implication for future work

Figure 4.21 to 4.23 demonstrate common misfits in the model. Careful analysis of them provides insights for future improvements. Two kinds of misfits are identified. Figure 4.21 shows the first kind: Offset. The first kind misfit might be caused by the misfit of lateral variation of the Earth structure. The model of this work is a spherically symmetric model. However, the area we model is located in the subduction zone which is structurally complex, with strong variations in elastic and viscous properties owing to the presence of Pacific oceanic lithosphere subducting beneath Japan and juxtaposed against the island arc upper plate. A more realistic modeling of the geometry at subduction zones would require more advanced numerical methods such as Finite Element Method (FEM) [*Sun et al.*, 2014]. How-

ever, with FEM, inversion is practically impossible because of complexity of the geometry and the great computational intensity.

Figure 4.22 and 4.23 show the second kind of misfit: Misfit of curvature. Two reasons might cause this misfit: (1) The Maxwellian rheology of the lower crust of uppermost mantle perhaps is too simple a rheology. Burger's rheology or even nonlinear rheology is needed to explain the misfit. (2) The viscoelastic relaxation might happen in multiple layers of the Earth with different relaxation time. Further modeling that account for lateral variations in Earth structure will be needed to better understand co- and postseismic deformation follow mega-earthquakes.

4.8 Conclusion

An nonlinear inversion method has been developed to deconvolve the coupled effect of afterslip and viscoelastic relaxation. We employ continuous GPS data that is spanning over two years before and three years after the 2011 Tohoku earthquake, as well as seafloor observations, to invert for the viscoelastic structure of the Earth in and around Japan and the afterslip history on the fault.

Our main conclusions include:

1. The Maxwellian viscosity of lower crust and uppermost mantle around Japan is $10^{18.9} \approx 7.9 \times 10^{18} Pa \cdot s$. The elastic depth of this area is 51 km.
2. Afterslip happens mainly in the down-dip direction of the coseismic slip. The total moment released by afterslip is about $1 \times 10^{22} Nm$, which corresponds to $M_w = 8.67$.

3. Afterslip is the dominant mechanism at the beginning of the postseismic deformation, and after about 1 year viscoelastic relaxation starts to dominate the postseismic deformation.

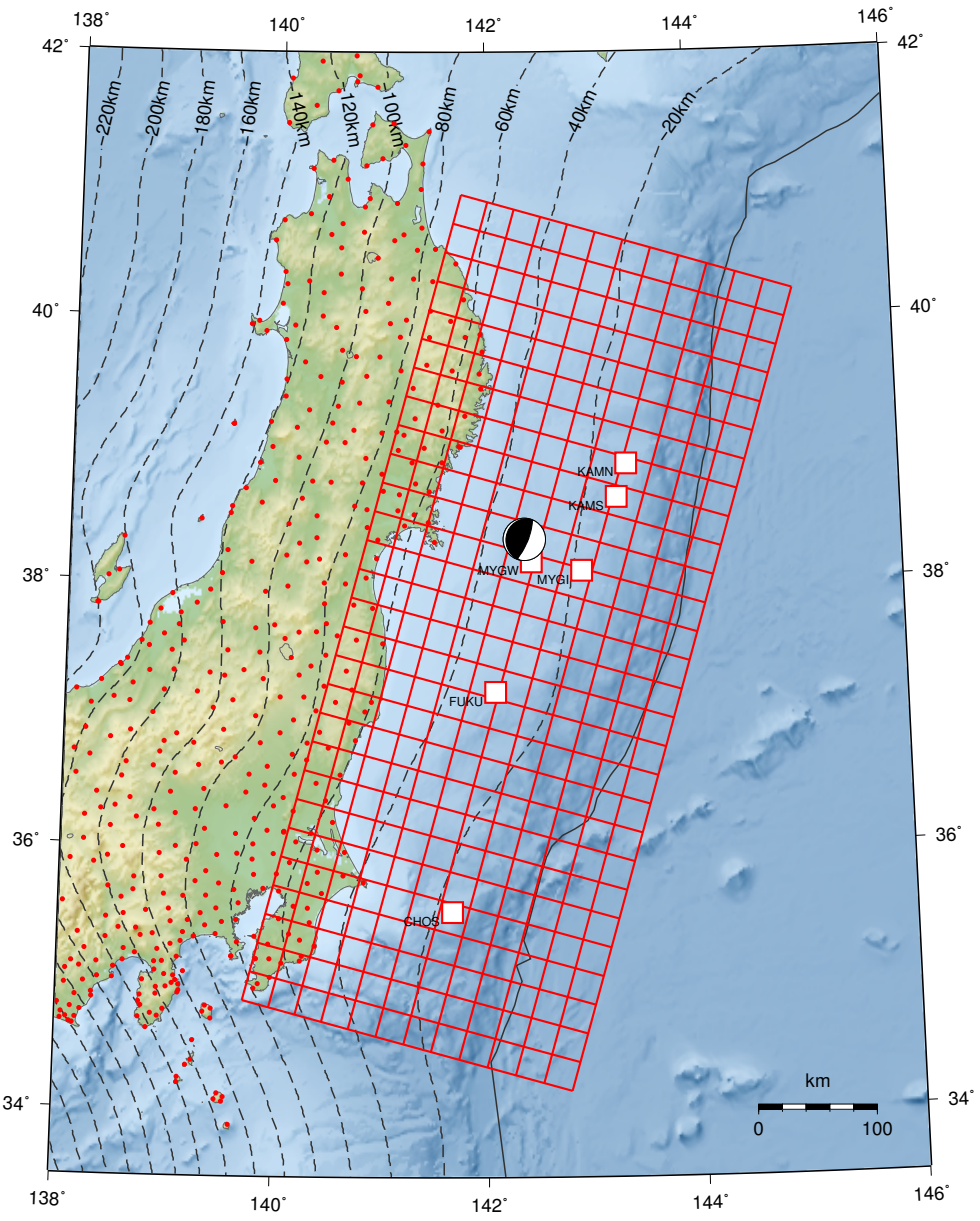

Figure 4.1: Fault model in map view. The red meshes are subfaults. The open squares are seafloor stations. The red dots represent inland GEONET stations. The dashed black lines are slab contours.

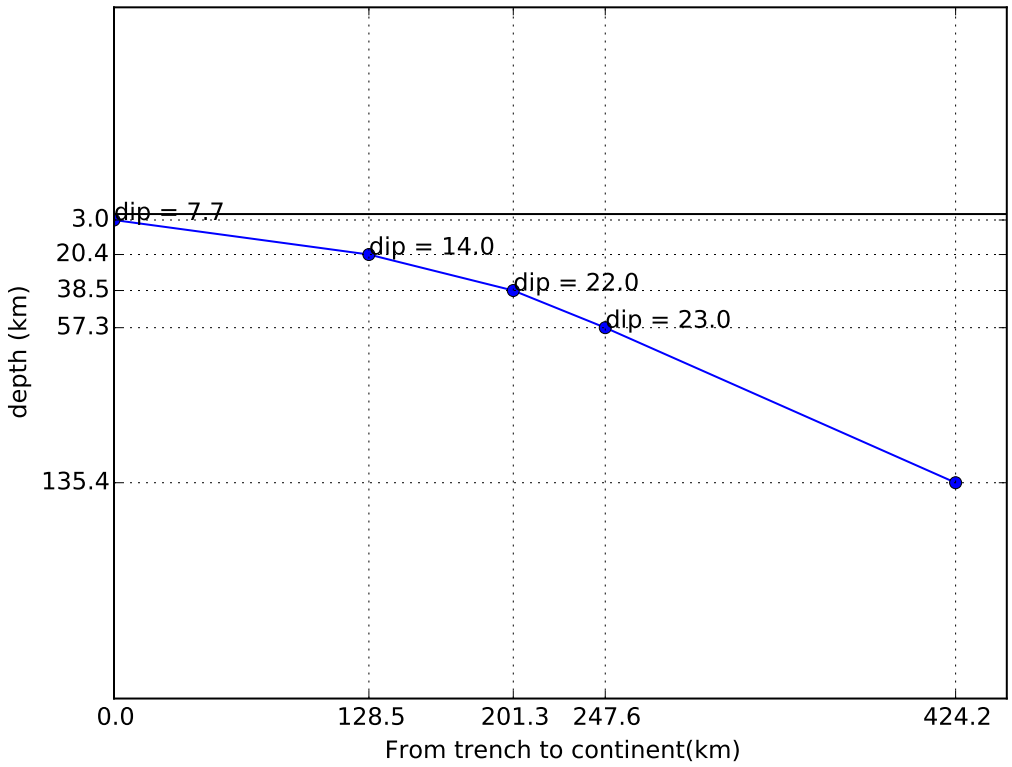

Figure 4.2: Cross section view of the fault model. The x-axis is the distance from the trench to the continent along the dip direction. The y-axis is the depth. Dip angle of each section of the fault is text-labeled.

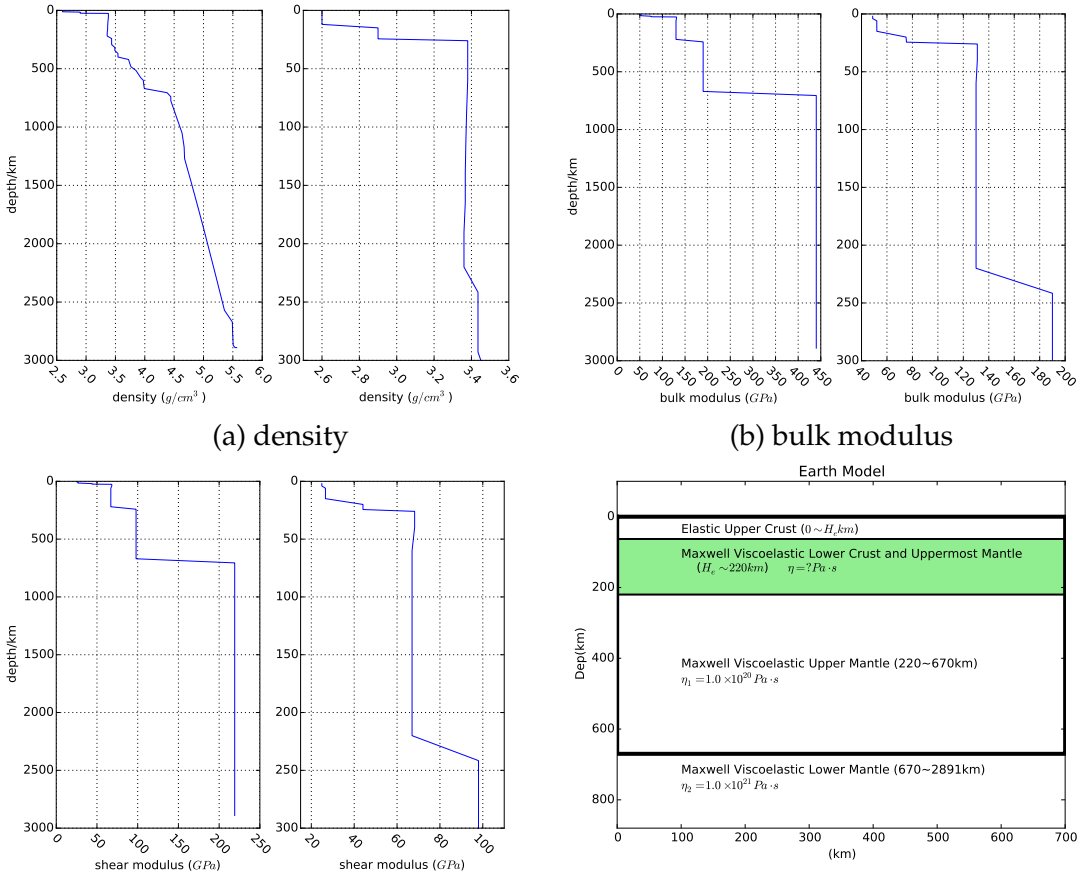

(a) density (b) bulk modulus

(c) shear modulus (d) Maxwell viscosity

Figure 4.3: Properties of the spherical Earth model along depth/radius. Elastic properties (density, bulk modulus, and shear modulus) follow PREM [*Dziewonski and Anderson*, 1981], each of which is plotted with two different depth scales. Subfigure (d) shows viscosities and depth of each viscoelastic layer, where H_e and η are undetermined non-linear parameters.

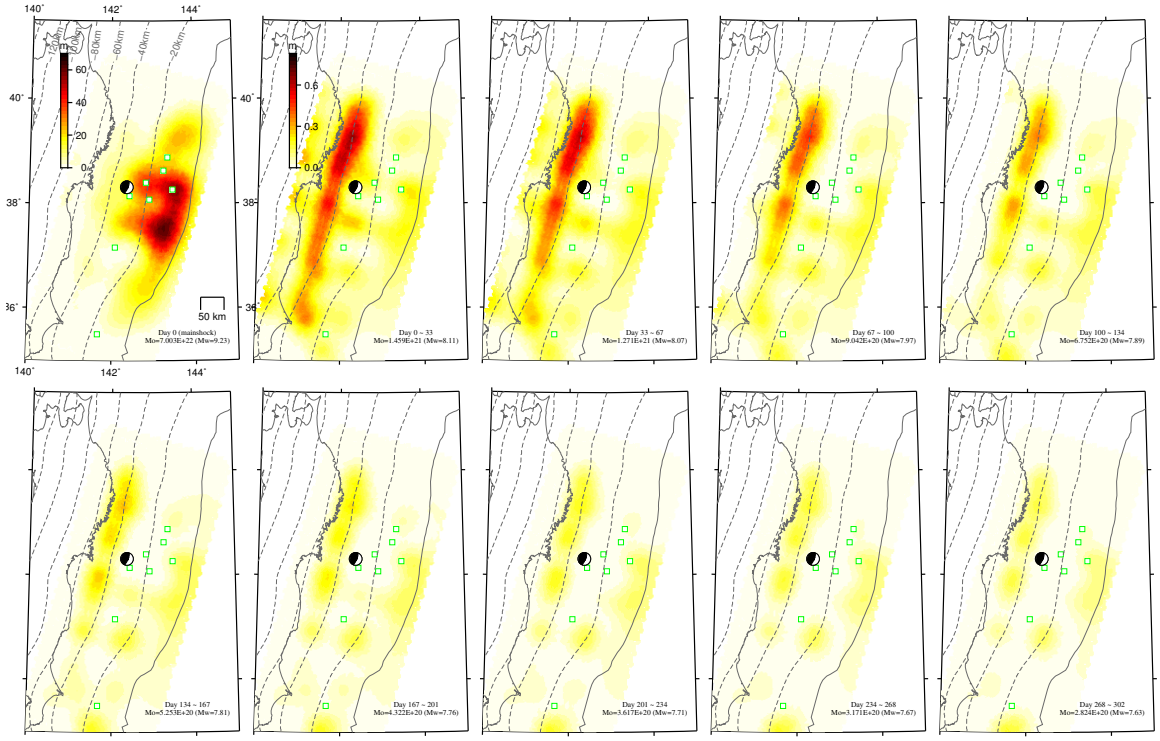

Figure 4.4: Inverted fault slip during different time periods. Open squares are the GPS/A seafloor stations. Note that the first subplot (coseismic slip) uses a different color scale than others.

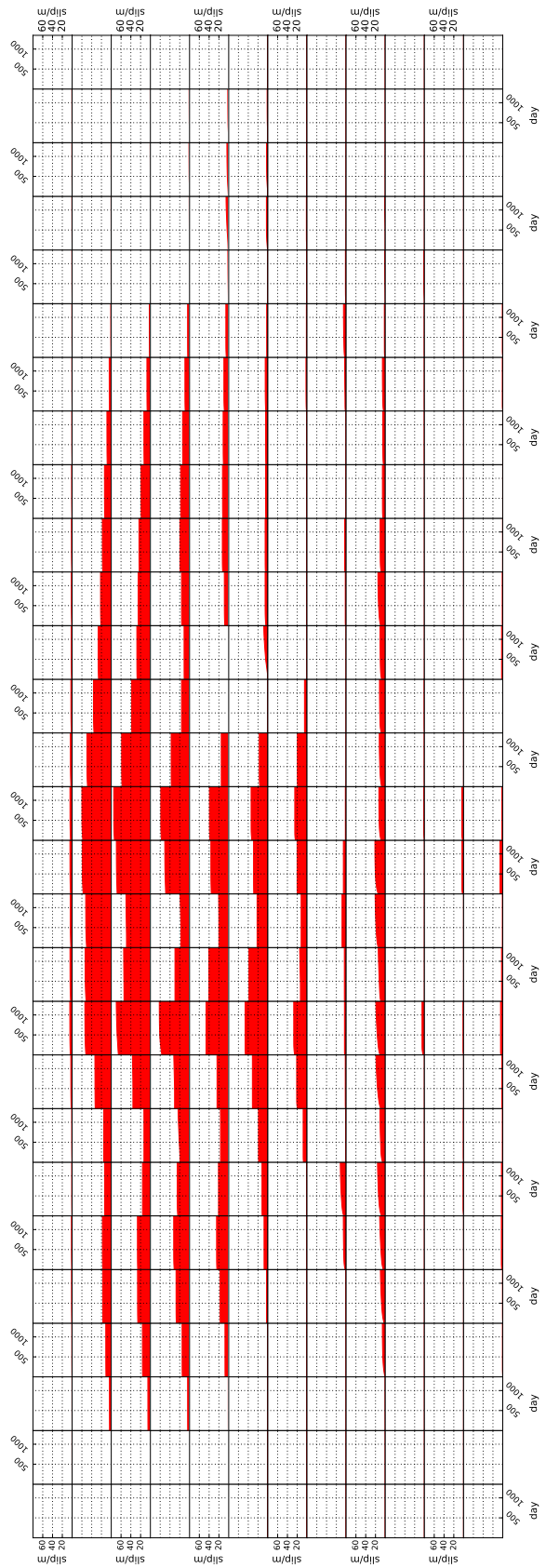

Figure 4.5: Slip history on each subfault. Each subblock depicts slip evolution on the corresponding subfault. The top of the figure corresponds to the trench. The bottom of the figure corresponds to the botthom of the fault. The x axis is the days after the mainshock. The y axis is the slip in cm.

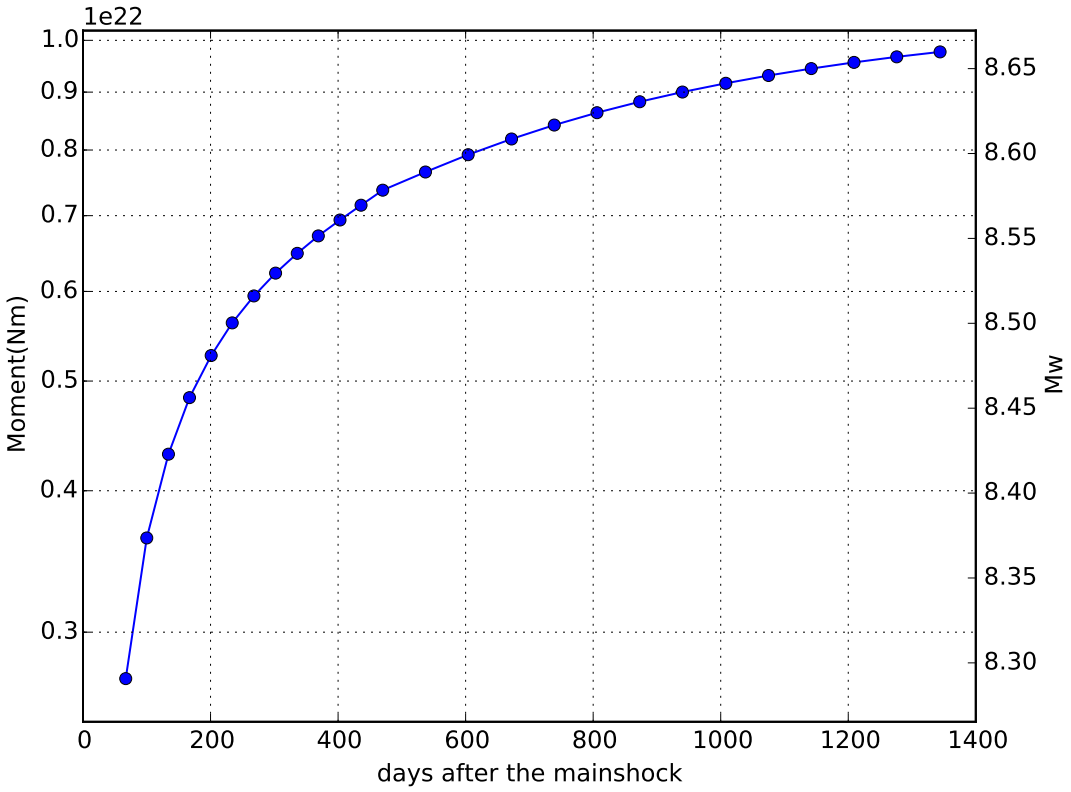

Figure 4.6: Inverted moment and moment magnitude of afterslip. Dots show the epochs where the integral is discretized.

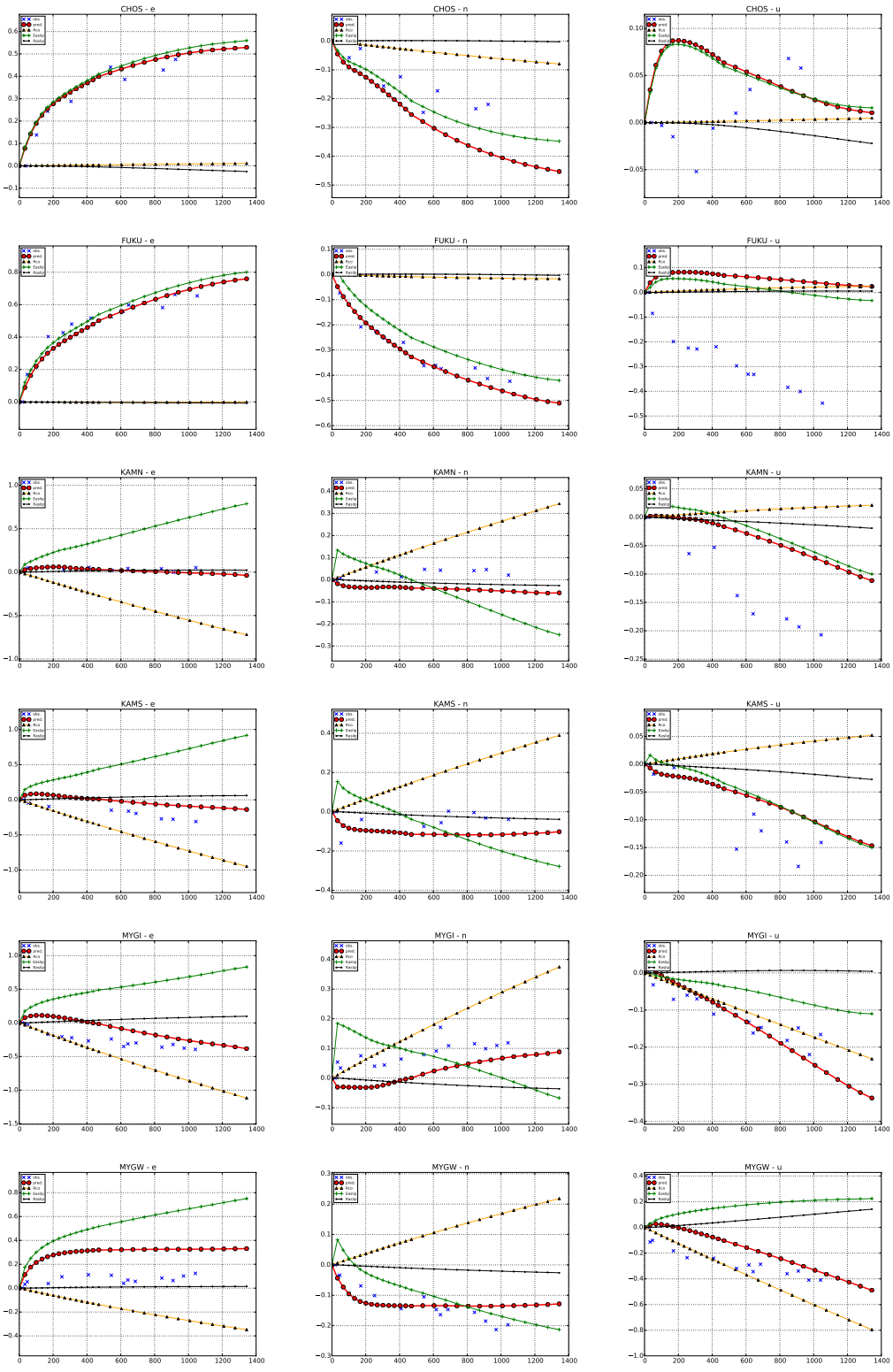

Figure 4.7: Predicated decomposition of seafloor displacements.

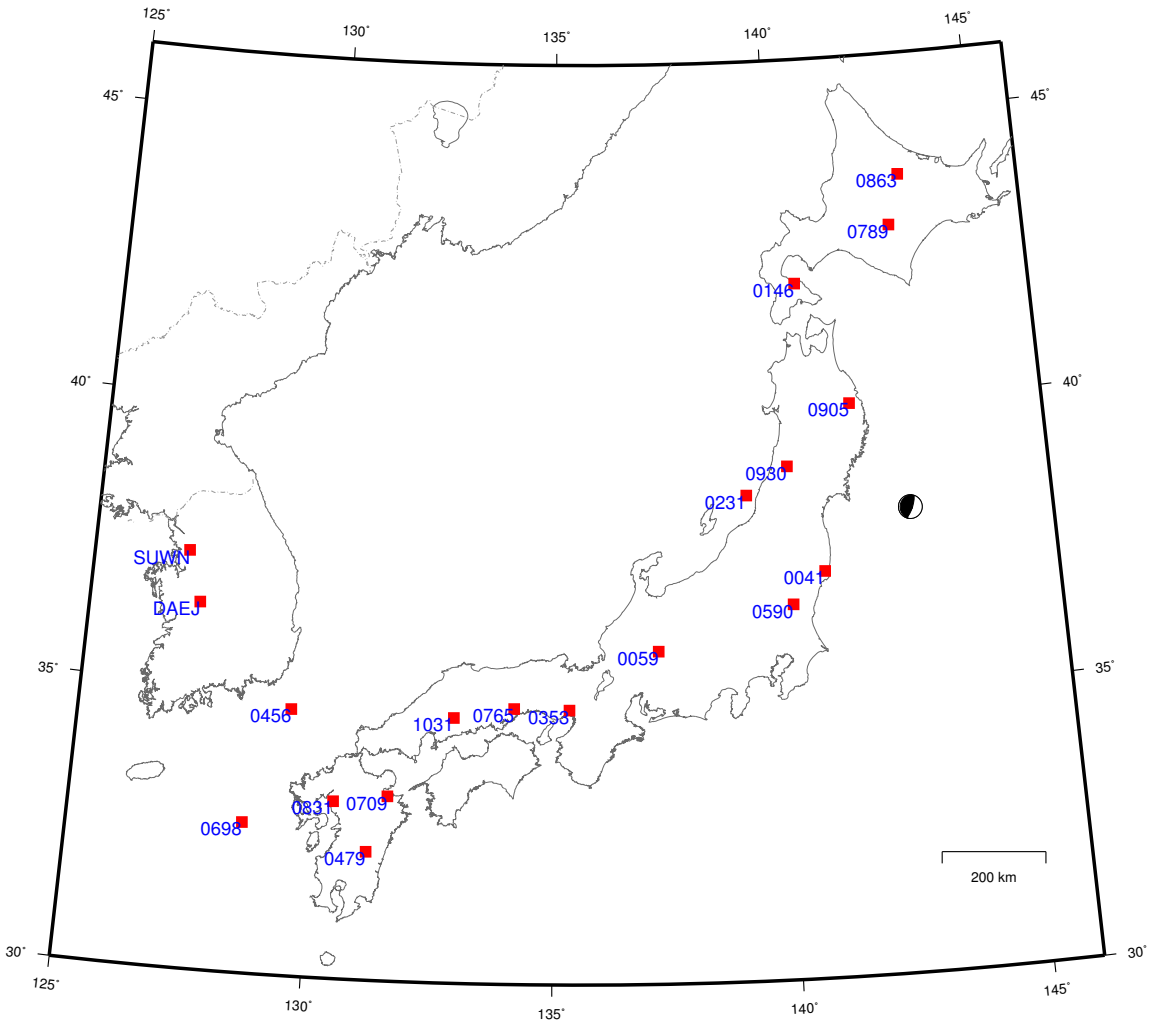

Figure 4.8: Sites map.

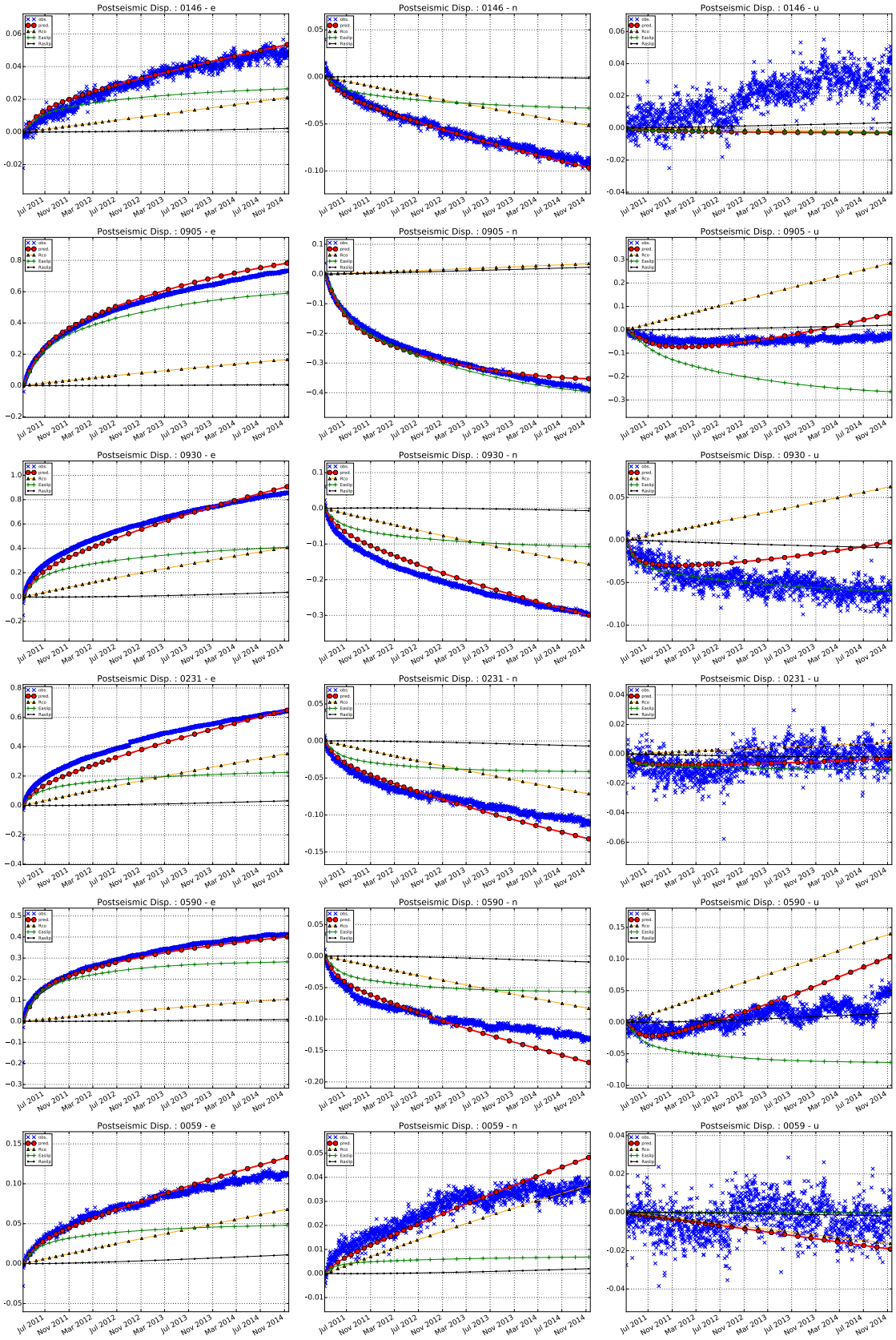

Figure 4.9: Obervation (blue cross) versus predicted time series of onshore GPS stations and its decomposition into different mechanisms. Stations in this plot are located at Honshu.

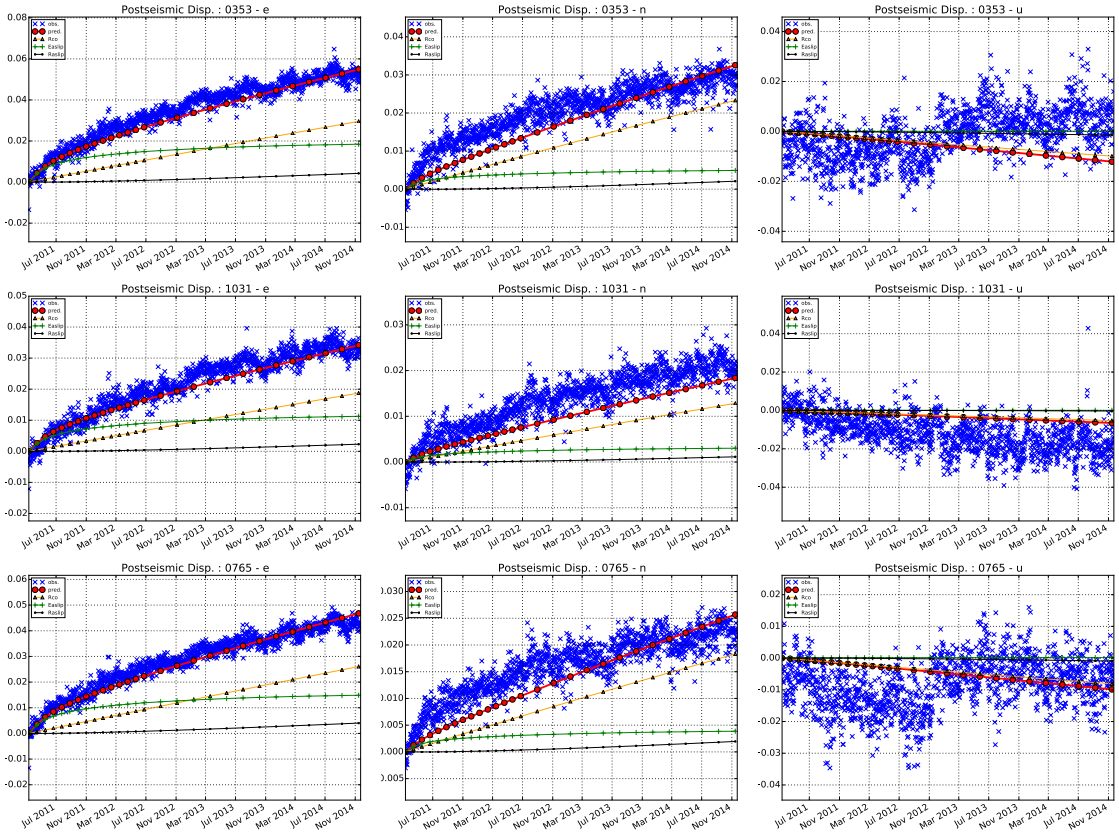

Figure 4.10: The same as Figure 4.9. Stations in this plot are located at Southwest Japan.

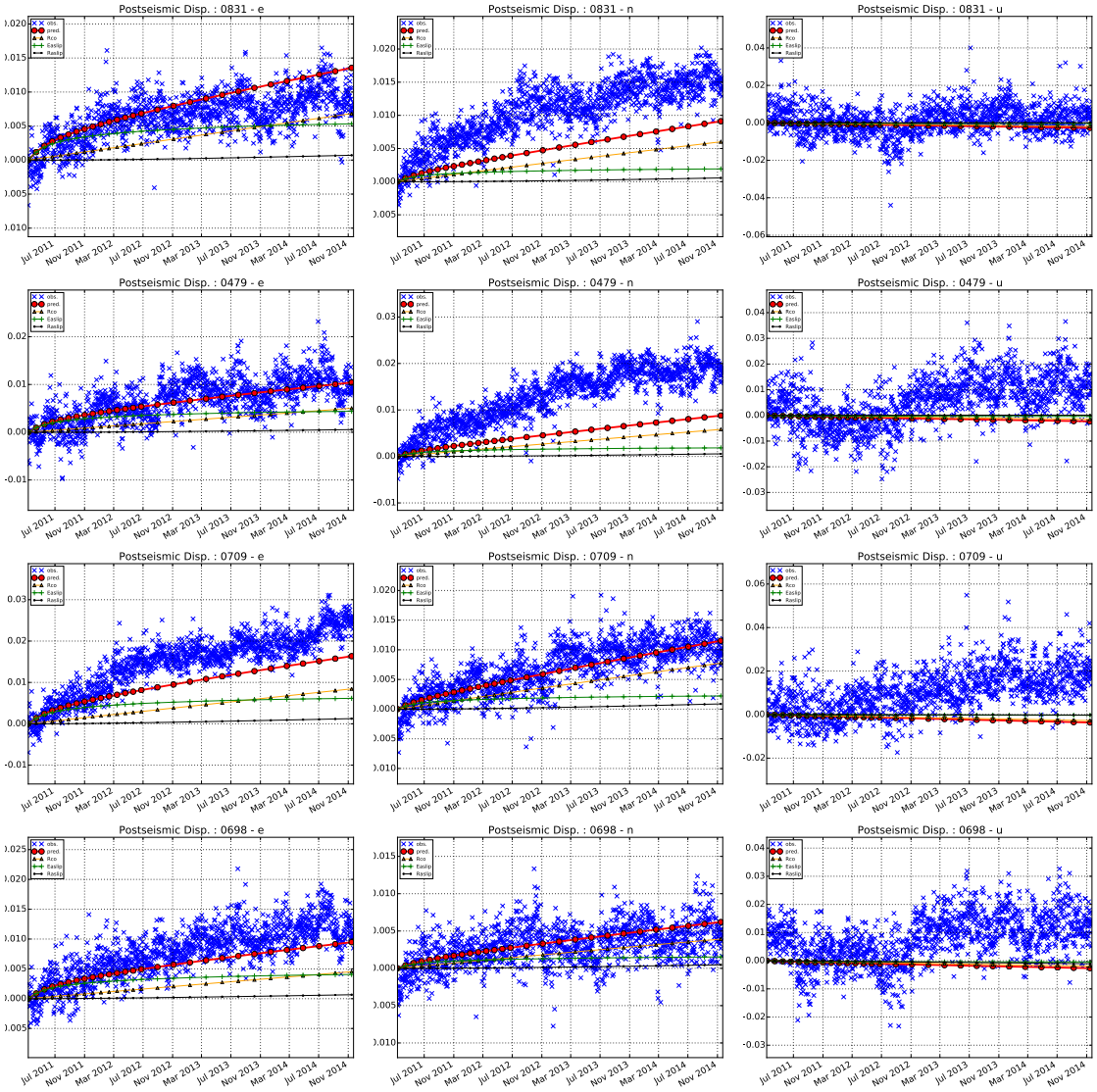

Figure 4.11: The same as Figure 4.9. Stations in this plot are located at Kyushu.

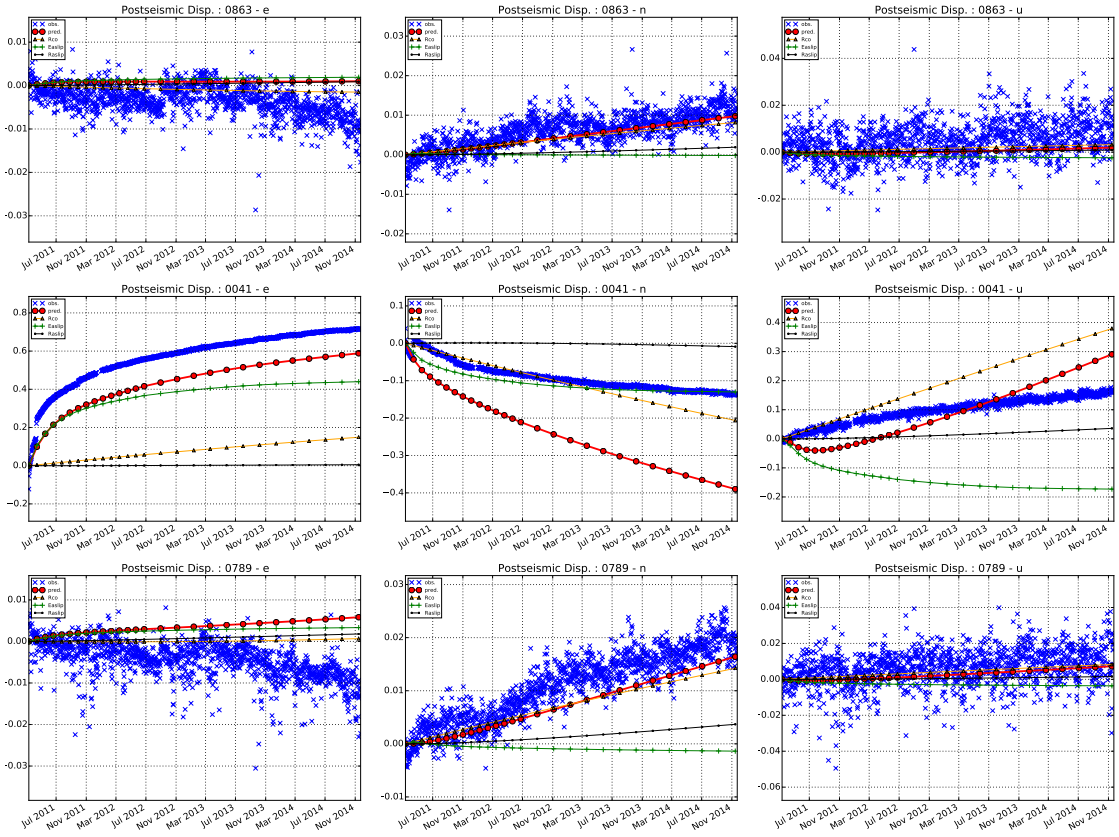

Figure 4.12: The same as Figure 4.9. Stations in this plot are located at Hokkaido.

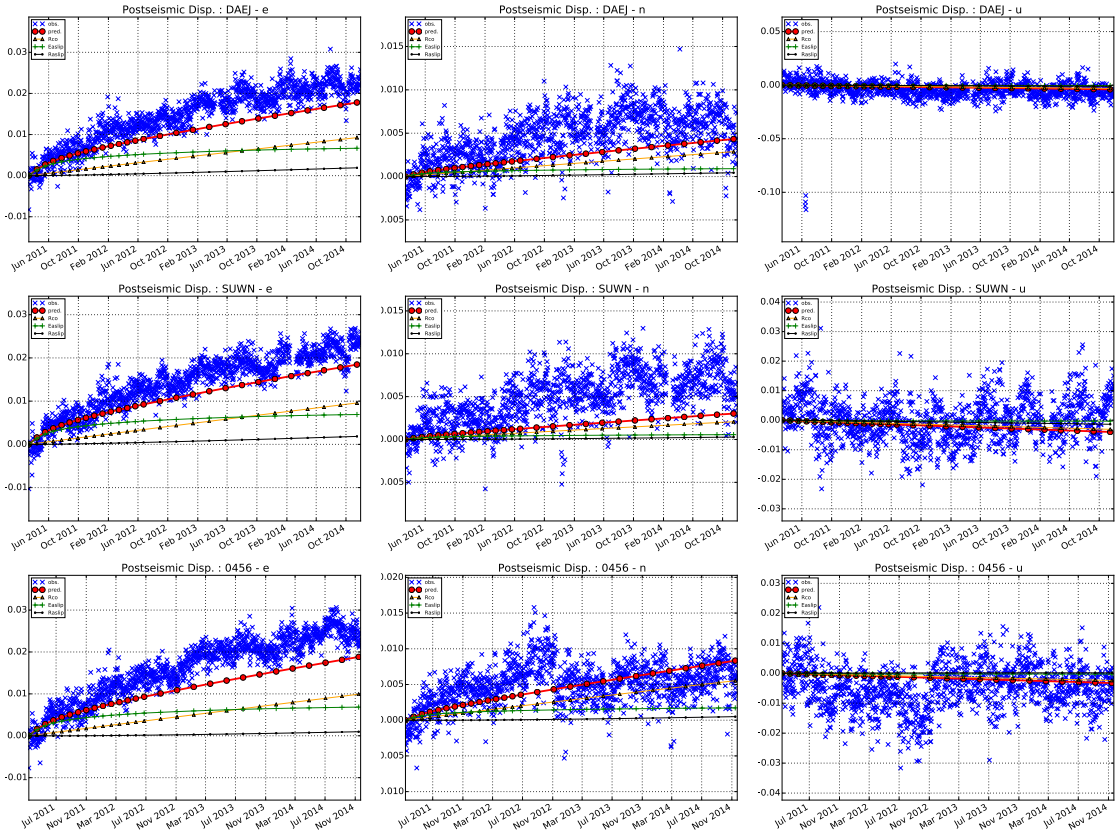

Figure 4.13: The same as Figure 4.9. Stations in this plot are located at South Korea and Korea Strait.

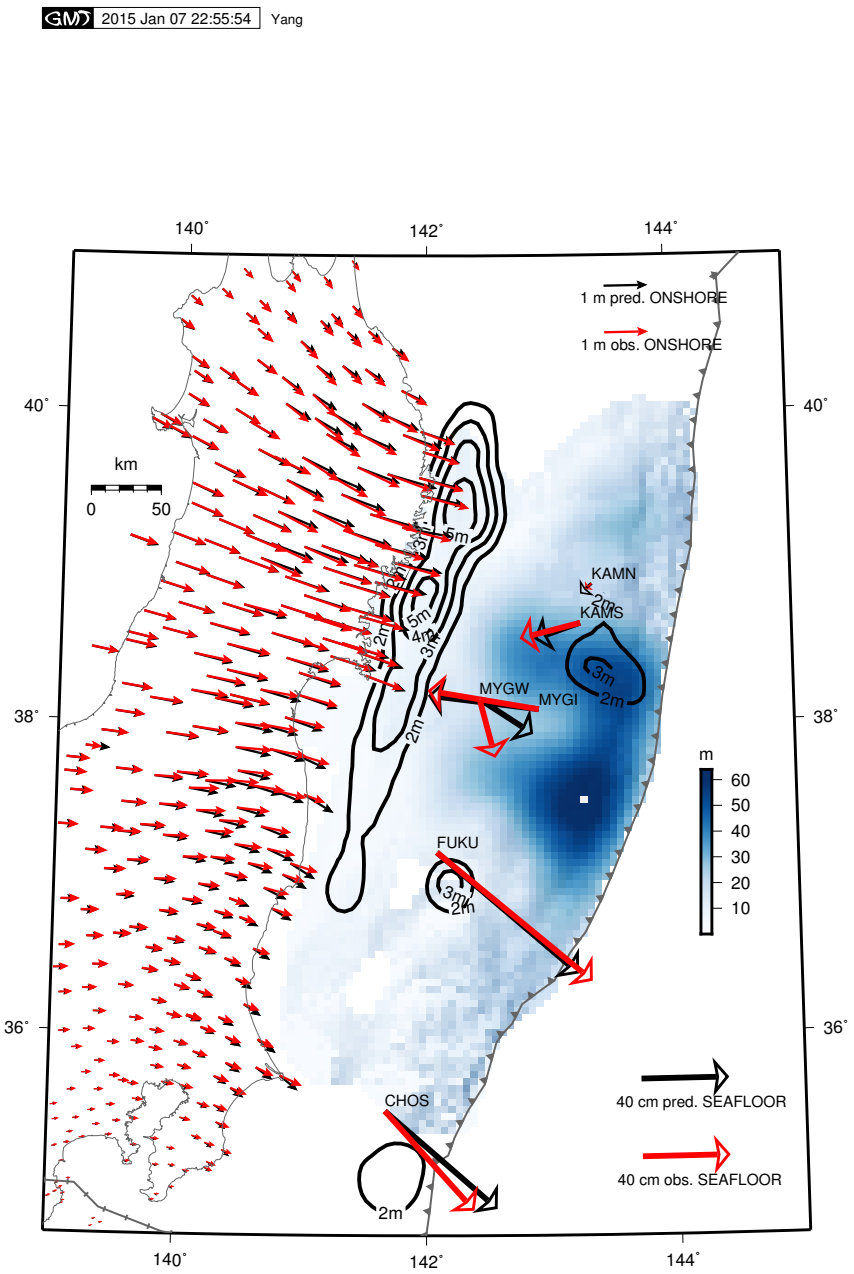

Figure 4.14: Postseismic displacements observed after 1344 days of the mainshock. Black contours show inverted afterslip. Colors show inverted coseismic slip. Onshore (solid head) and seafloor (open head) observations are plotted using different scales. Seafloor station MYGI, KAMS and KAMN show landward movements.

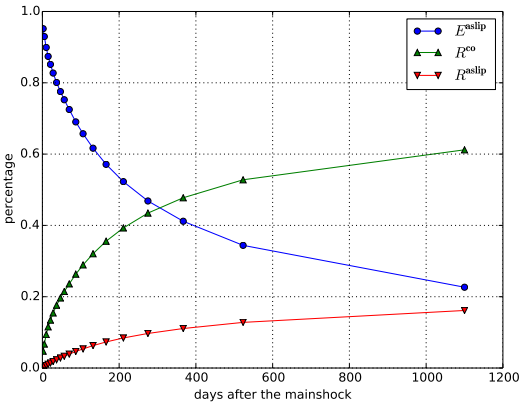

(a) Percentage of cumulative postseismic deformation.

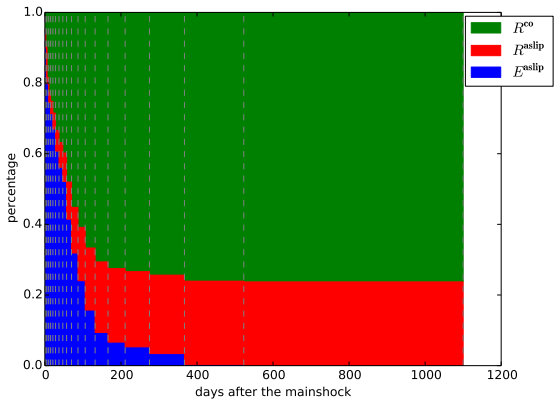

(b) Percentage over each time section.

Figure 4.15: Percentage of postseismic deformation caused by different mechanisms, averaging over all stations. The percentage values are averaged over all stations.

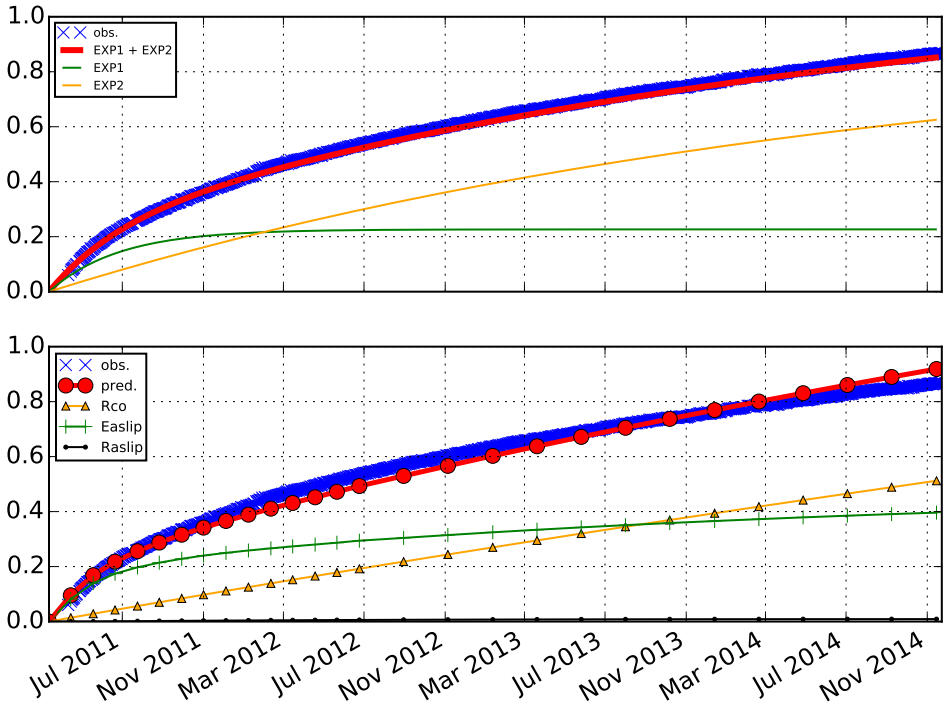

Figure 4.16: Compare the time series modeling result with model prediction of different deformation mechanisms for GEONET station 0550. Blue crosses are the observed postseismic time series of the east component of station 0550. In the upper subplot, thick red line is prediction of Model 2EXPs, which is composed of two exponentional terms (brown and green lines). In the lower subplot, model predicted time series (red line with dots) is composed of elastic deformation caused by afterslip (E_{aslip}, green line with crosses), viscous relaxation caused by coseismic slip (R_{co}, brown line with triangles), and viscous relaxation caused by afterslip (R_{aslip}, black line with dots).

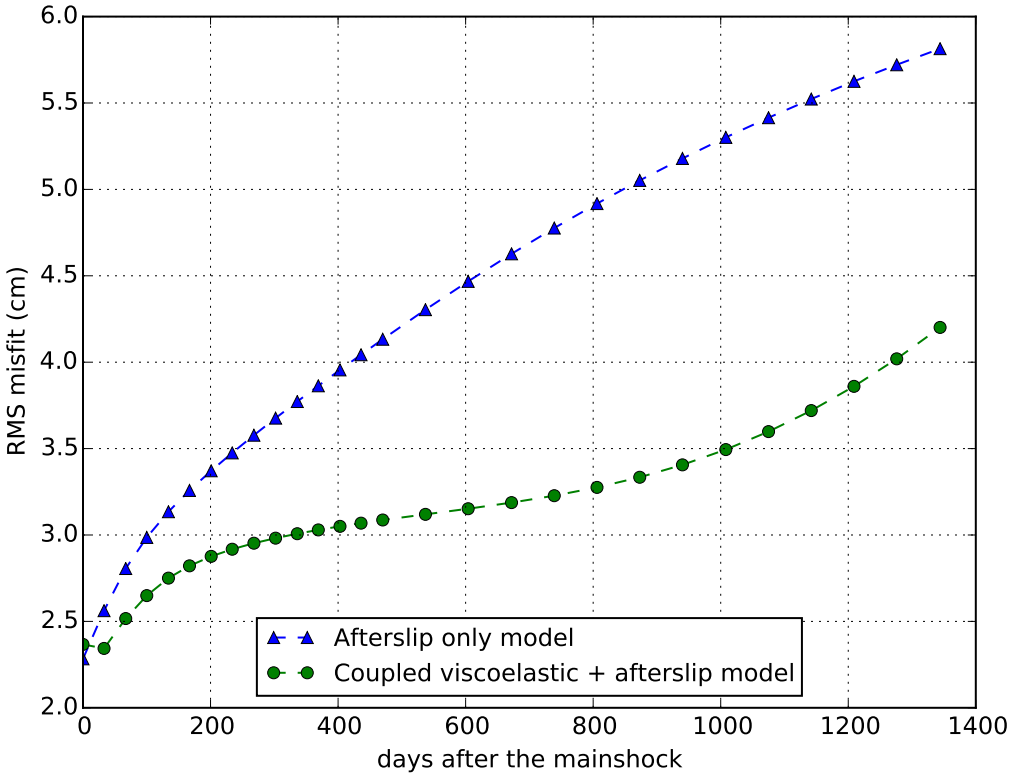

Figure 4.17: RMS misfits of afterslip-only model (triangle line) and coupled viscoelastic relaxation and afterslip model (dot line).

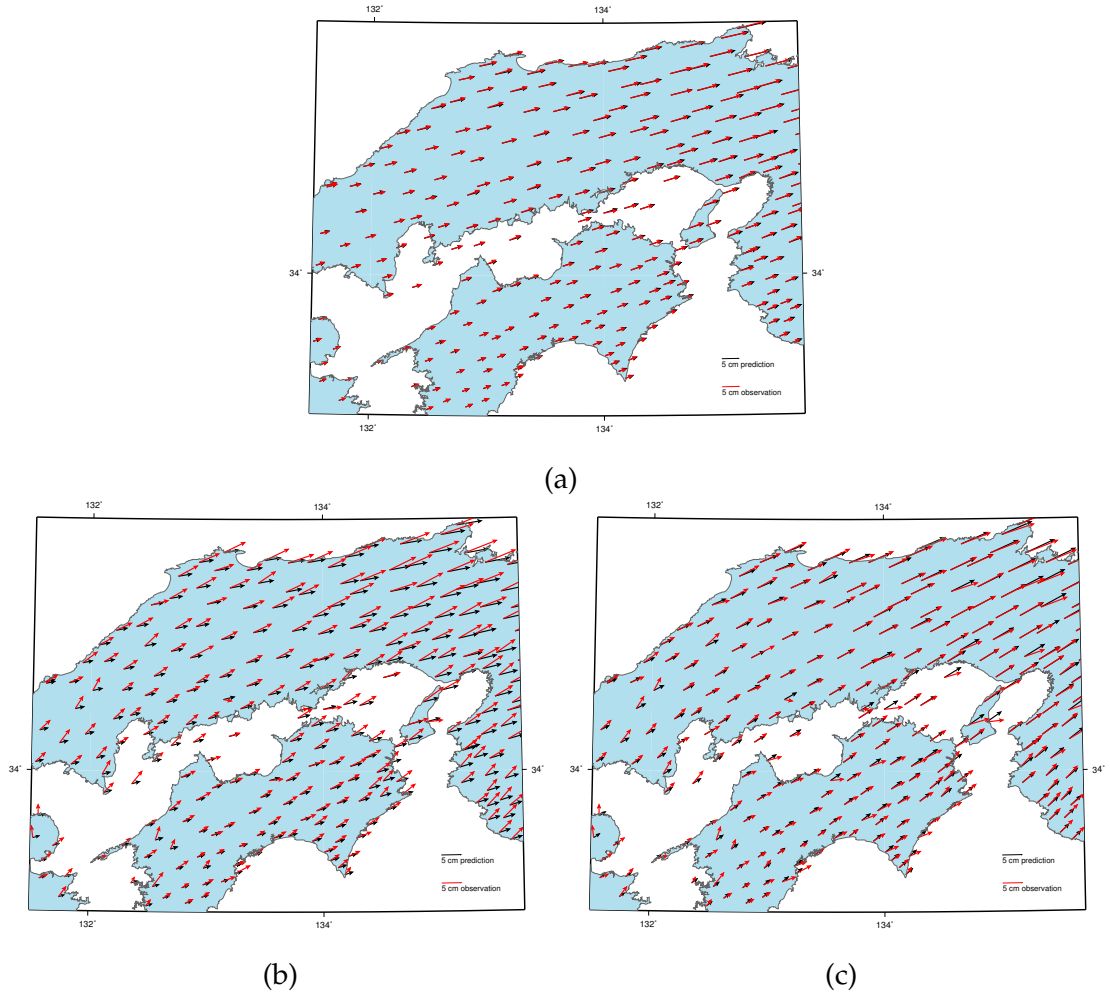

(a)

(b) (c)

Figure 4.18: At southwest Honshu: (a) Observed (red vectors) versus predicted (black vectors) coseismic displacements. (b) Observed postseismic displacements (red vectors) versus afterslip-only model predicted postseismic displacements (black vectors). (c) Observed postseismic displacements (red vectors) versus coupled model predicted postseismic displacements (black vectors). Postseismic displacements in (b) and (c) are 1344 days after the mainshock. For postseismic modeling, while there is a systematic azimuthal misfit for afterslip-only model (b), viscoelastic relaxation and afterslip coupled model provides a much better fit (c).

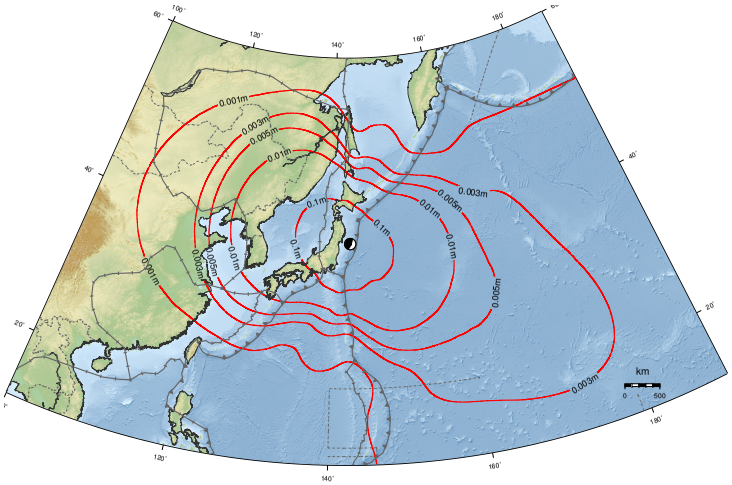

(a) Total postseismic displacements (Rco+Easlip+Raslip)

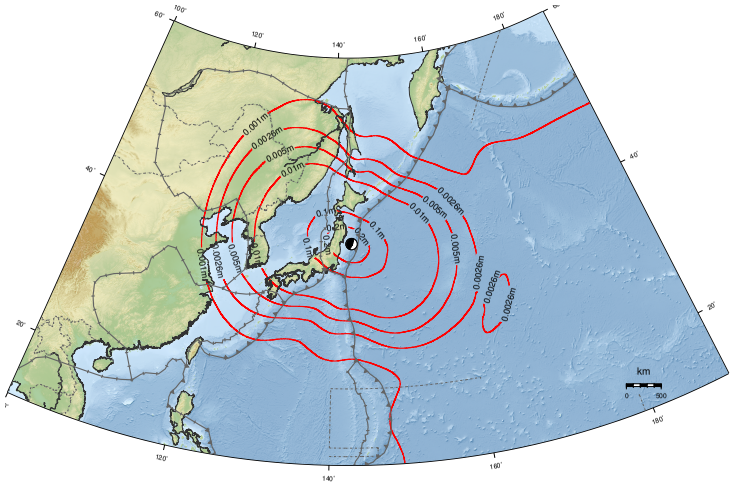

(b) Rco - viscoelastic relaxation caused by coseismic slip

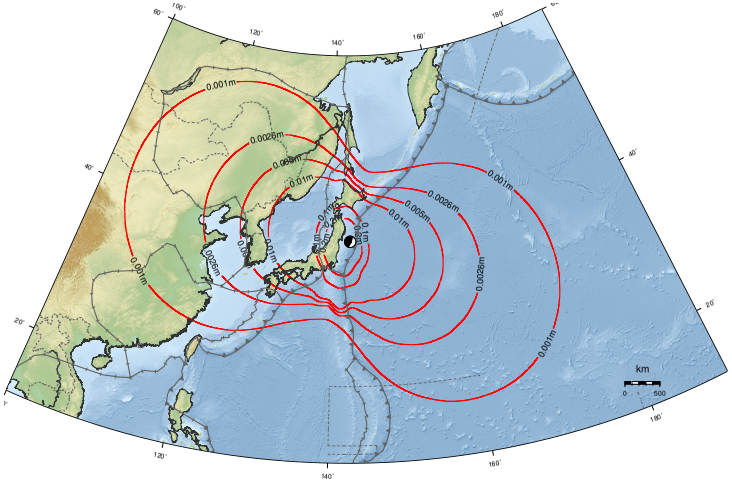

(c) Easlip - elastic deformation caused by afterslip

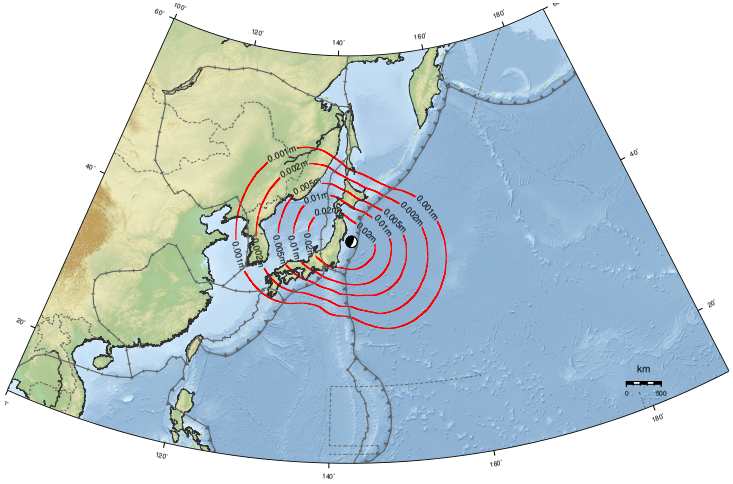

(d) Raslip - viscoelastic relaxation caused by afterslip

Figure 4.19: Contours of horizontal postseismic displacements caused by different mechanisms at 1344 days after the mainshock.

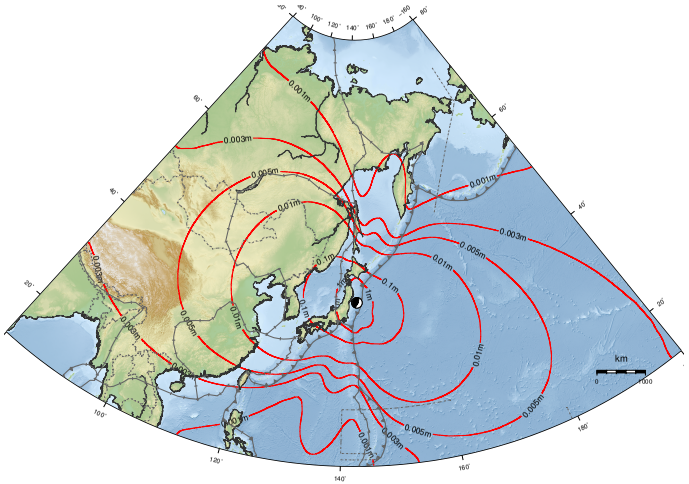

(a) 5 yr

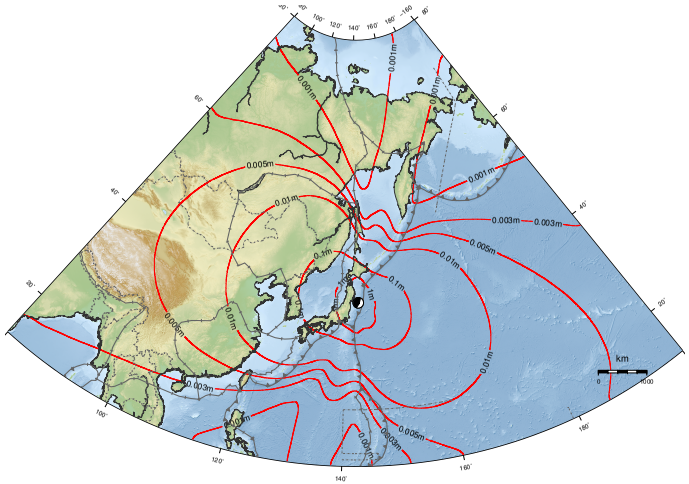

(b) 10 yr

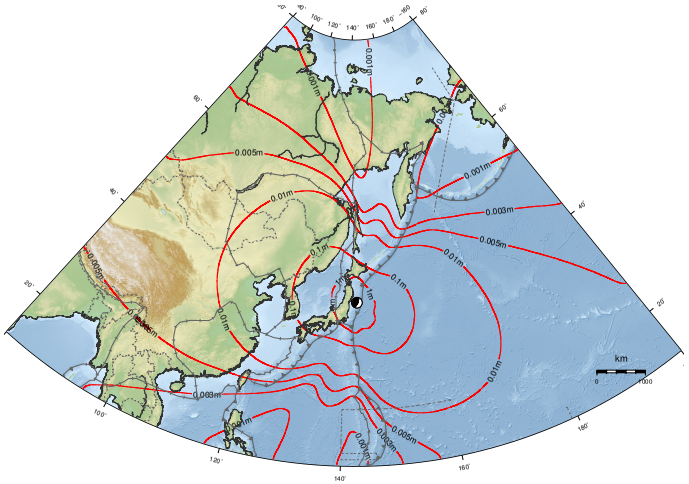

(c) 15 yr

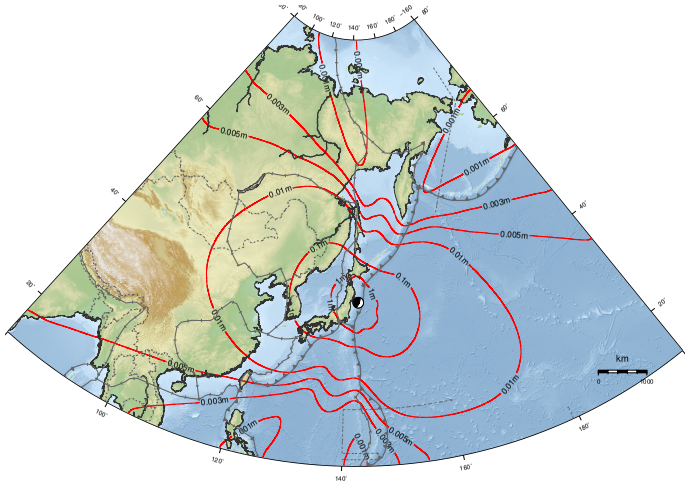

(d) 20 yr

Figure 4.20: Long term viscous relaxation predicted by the model, assuming no more afterslip after 1344 days of the mainshock.

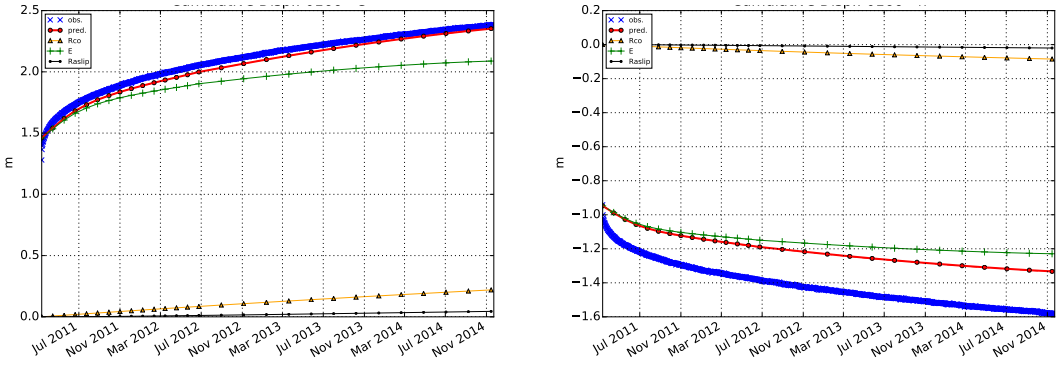

(a) East component. (b) North component.

Figure 4.21: Misfit demonstration: Type 1 - Offsets. Observed postseismic time series (blue crosses) of stations 0116 versus model prediction (red line with dots) and its decomposition into different mechanisms. While the east component fits very well (a), there is an offset misfit in the north component (b).

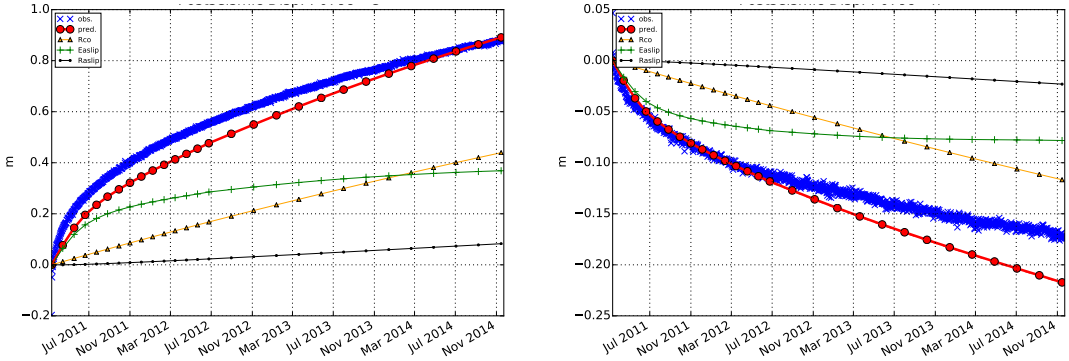

(a) East component. (b) North component.

Figure 4.22: Misfit demonstration: Type 2 - Misfit of Curvature. Observed postseismic time series (blue crosses) of stations 0799 versus model prediction (red line with dots) and its decomposition into different mechanisms. East component fails to fit the curvature in the middle. North component fails to fit the curvature towards the end of the time series.

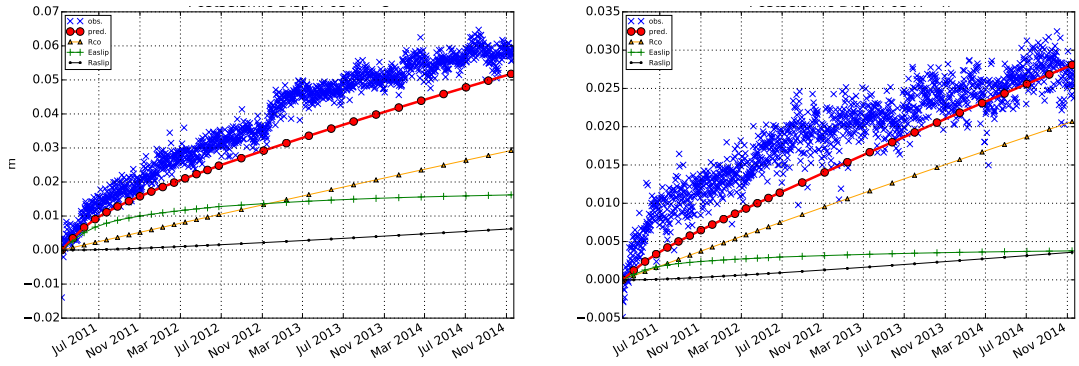

(a) East component.

(b) North component.

Figure 4.23: Misfit demonstration: Type 2 - Misfit of Curvature. Observed cumulative postseismic time series (blue crosses) of stations 0347 versus model prediction (red line with dots) and its decomposition into different mechanisms. The north component failed to fit the initial fast trend.

CHAPTER 5

CONCLUSION

The 2011 Tohoku Earthquake is the largest earthquake ever hit Japan in modern times, and it has been well recorded by various modern observational techniques. This thesis focuses on the GPS observation of this earthquake. Time series analysis is carried out to obtain coseismic and postseismic displacements information. Two different postseismic time series models (Model 2EXPs and Model EXP) are used to fit postseismic time series. Coseismic displacements is inverted for coseismic slip, as well as its rake, through a non-linear inversion method - Occam's algorithm. Characteristics of vertical and horizontal displacements of coseismic deformation have been examined. For postseismic deformation, the coupled effect of afterslip and viscoelastic relaxation is formulated as a LTI system. Occam's algorithm is used to invert for nonlinear parameters including viscosity of lower crust and uppermost mantle($10^{18.9} \approx 7.9 \times 10^{18} Pa \cdot s$), elastic thickness (51 km), and the rake of fault slip (83 $^\circ$). The percentage of deformation caused by different mechanisms are obtained. Deformation caused by afterslip dominates in the first 1 year after the mainshock, and viscoelastic deformation dominates at later stage of deformation.

APPENDIX A
MATHEMATICAL FORMULATION FOR LINEAR AND NONLINEAR INVERSION

A.1 Linear inversion

The basic formation that connects the slip on the fault and the observed displacements is $\mathbf{d} = \mathbf{Gm}$, where $\mathbf{d}$ and $\mathbf{m}$ are data and model parameters, respectively, and matrix $\mathbf{G}$ contains Green's functions. The corresponding inverse problem can be formulated as:

$$\min_{\mathbf{m}} \left\{ \|\mathbf{Gm} - \mathbf{d}\| + \sum_i \alpha_i \|\mathbf{L}_i \mathbf{m}\| \right\} \tag{A.1.1}$$

The second term represents all the necessary regularizations. For slip inversion, three regularizations are considered: 0th order regularization (damping) [*Evans and Meade*, 2012; *Iinuma et al.*, 2012], 2nd order regularization (smoothing) [*Yabuki and Matsu'ura*, 1992; *Matsu'ura et al.*, 2007] and boundary regularization [*Iinuma et al.*, 2012]. Each regularization introduce a hyper-parameter (regularization parameter). Note that *Iinuma et al.* [2012] uses all these three regularizations to study the coseismic slip of the 2011 Tohoku earthquake. For deconvolution inversion, temporal regularization on slip at each subfault is also considered to enforce temporal smoothness of slip evolution.

Regularizations represent a priori information we impose on the model parameters in order to overcome the ill-conditionedness of the inversion problem (indirect a priori information *Matsu'ura et al.* [2007]). An important aspect of inversion is to choose proper regularization parameters. The values of regularization parameters suggest the importance of each piece of a priori information in deciding the final results. An frequently used empirical way of deciding regularization parameters is called L-curve method. [*Aster et al.*, 2013; *Frasso*, 2012]. *Silverii et al.* [2014]

uses this method to study the afterslip of the 2011 Tohoku earthquake. Another often used method is called Bayesian information criterion [*Yabuki and Matsu'ura*, 1992], which is a more objective way of deciding the hyper-parameters, and it has also been used in the inversion for the coseismic slip of the 2011 Tohoku earthquake [*Ozawa et al.*, 2012]. In this study, we use an empirical approach, L-curve method, to choose hyper-parameters.

Weighting matrix and basis matrix are some other factors that are often introduced into equation A.1.1. Weighting matrix are introduced into equation A.1.1 to give different observation different importance. Furthermore, various basis functions can be used in the inversion. They are different orthogonal bases of the functional space, where the model parameter finds its value. Because the value of model parameter is a linear combination of the basis function, nice properties of the basis function such as continuity, smoothness or zero boundary slips, etc., can be adopted by the model parameter. Frequently used basis functions include boxcar functions, B-spline functions [*Yabuki and Matsu'ura*, 1992], and Hermite polynomials [*Pollitz et al.*, 1998]. If we assume matrix $\mathbf{G}$ is always the displacements corresponding to step slip on each subfaults, choosing different basis functions is equivalent to introducing another matrix B (basis matrix) in the equation A.1.1. In this study, we use B-spline function introduced in [*Yabuki and Matsu'ura*, 1992]. However, we modify the slip generation rule to allow maximum slip at boundaries of the fault, so that the effect of boundary slip can be evaluated independently.

With weighting matrix and basis matrix, A.1.1 becomes:

$$\min_{\mathbf{m}} \left\{ \|\mathbf{WGBm} - \mathbf{Wd}\| + \sum_i \alpha_i \|\mathbf{L}_i\mathbf{Bm}\| \right\} \tag{A.1.2}$$

Instead of using regularization, another approach of considering a priori information is to use Bayesian method, where a priori information and model parameters are treated as random variables with probability distributions [*Aster et al.*,

2013; *Minson*, 2010; *Minson et al.*, 2014]. However, this method is usually computationally expensive.

A.2 Nonlinear inversion and Occam's algorithm

Inversions carried out in this study also include a number of nonlinear parameters, including the slip rake, the elastic thickness and the viscosity of the lower crust and the uppermost mantle. In this section, a popular nonlinear inversion algorithm - Occam's algorithm is introduced and tailored for applications in this thesis.

Occam's algorithm [*Constable et al.*, 1987] is based on a similar idea to Newton's method: iteratively apply local linearization to approximate local minimum. Taylor's theorem is applied to obtain local approximation,

$$\mathbf{G}\left(\mathbf{m}+\Delta\mathbf{m}\right) \approx \mathbf{G}\left(\mathbf{m}\right)+\mathbf{J}\left(\mathbf{m}\right)\Delta\mathbf{m}, \tag{A.2.1}$$

where $\mathbf{J}(\mathbf{m})$ is the Jacobian,

$$\mathbf{J}\left(\mathbf{m}\right)=\begin{bmatrix} \frac{\partial G_1\left(\mathbf{m}^k\right)}{\partial m_1} & \cdots & \frac{\partial G_1\left(\mathbf{m}^k\right)}{\partial m_n} \\ \vdots & \ddots & \vdots \\ \frac{\partial G_m\left(\mathbf{m}^k\right)}{\partial m_1} & \cdots & \frac{\partial G_m\left(\mathbf{m}^k\right)}{\partial m_n} \end{bmatrix}. \tag{A.2.2}$$

Using Equation (A.2.1), the regularized least square problem

$$\min_{\mathbf{m}}\left\{\left\|\mathbf{G}\left(\mathbf{m}\right)-\mathbf{d}\right\|_2^2+\alpha^2\left\|\mathbf{L}\mathbf{m}\right\|_2^2\right\}$$

becomes

$$\min_{\mathbf{m}}\left\{\left\|\mathbf{G}\left(\mathbf{m}\right)+\mathbf{J}\left(\mathbf{m}\right)\Delta\mathbf{m}-\mathbf{d}\right\|_2^2+\alpha^2\left\|\mathbf{L}\left(\mathbf{m}+\Delta\mathbf{m}\right)\right\|_2^2\right\} \tag{A.2.3}$$

where the variable is $\Delta\mathbf{m}$ and $\mathbf{m}$ is constant. Changing the variable of Equation (A.2.3) into $\mathbf{m}'=\mathbf{m}+\Delta\mathbf{m}$, and letting

$$\widehat{\mathbf{d}}\left(\mathbf{m}\right)=\mathbf{d}-\mathbf{G}\left(\mathbf{m}\right)+\mathbf{J}\left(\mathbf{m}\right)\mathbf{m}, \tag{A.2.4}$$

gives

$$\min_{\mathbf{m}} \left\{ \|\mathbf{J}(\mathbf{m})(\mathbf{m}+\Delta\mathbf{m}) - (\mathbf{d} - \mathbf{G}(\mathbf{m}) + \mathbf{J}(\mathbf{m})\mathbf{m})\|_2^2 + \alpha^2 \|\mathbf{L}(\mathbf{m}+\Delta\mathbf{m})\|_2^2 \right\}, \tag{A.2.5}$$

or

$$\min_{\mathbf{m}'} \left\{ \left\| \mathbf{J}(\mathbf{m})\mathbf{m}' - \widehat{\mathbf{d}}(\mathbf{m}) \right\|_2^2 + \alpha^2 \|\mathbf{L}\mathbf{m}'\|_2^2 \right\}. \tag{A.2.6}$$

Because $\mathbf{J}(\mathbf{m})$ and $\widehat{\mathbf{d}}(\mathbf{m})$ don't change value within a given iteration, Equation (A.2.6) is in the form of a regularized linear least squares problem.

The algorithm is stated in Algorithm 1 following [*Aster et al.*, 2013], where χ^2 and δ^2 is the model misfit in the current iteration and the model misfit expected to reach, respectively. In this work, the minimization problem described by Equation (A.2.7) is solved by the python software Python Software for Convex Optimization (CVXOPT) [*Andersen et al.*, 2014].

Algorithm 1 Occam's Algorithm.

Beginning with an initial solution, $\mathbf{m^0}$, repeat the following steps to compute a sequence of solutions $\mathbf{m^k}$. Stop if and when the sequence converges to a solution with $\chi^2 = \delta^2$.

1. Calculate the Jacobian $\mathbf{J}\left(\mathbf{m}^k\right)$ and the vector $\widehat{\mathbf{d}}\left(\mathbf{m}^k\right)$.
2. Calculate updated models corresponding to a range of regularization parameter values, α,

$$\min_{\mathbf{m}^{k+1}} \left\{ \left\| \mathbf{J}\left(\mathbf{m}^k\right)\mathbf{m}^{k+1} - \widehat{\mathbf{d}}\left(\mathbf{m}^k\right) \right\|_2^2 + \alpha^2 \left\|\mathbf{L}\mathbf{m}^{k+1}\right\|_2^2 \right\}. \tag{A.2.7}$$

3. Choose the particular $\mathbf{m^{k+1}}$ with the largest value of α such that $\chi^2\left(\mathbf{m^{k+1}}\right) \leq \delta^2$. If no such value exists, then use the value of that minimizes $\chi^2\left(\mathbf{m^{k+1}}\right)$.
4. Let k = k + 1.

Separate linear and nonlinear parameters

For nonlinear slip inversion problems discussed in this thesis, the large majority of parameters are slips on the fault, which are linear. Only a few geometrical and material parameters are nonlinear. Therefore, Equation (A.2.6) can be further reformulated to separate linear and nonlinear parameters. This analysis can greatly enhance the clarity of programming.

Suppose the model parameter vector $\mathbf{m}$ contains linear components represented by $\mathbf{q}$, and nonlinear components represented by θ, and $\mathbf{m} = \begin{pmatrix} \mathbf{q} & \theta \end{pmatrix}^T$. In terms of $\mathbf{q}$ and θ, $\mathbf{G}(\mathbf{m})$ and $\mathbf{G}(\mathbf{m} + \boldsymbol{\Delta}\mathbf{m})$ can be interpreted as

$$\mathbf{G}\left(\mathbf{m}\right) = \mathbf{G}\left(\theta\right)\mathbf{q} \tag{A.2.8}$$

and

$$\mathbf{G}\left(\mathbf{m} + \Delta\mathbf{m}\right) = \mathbf{G}\left(\theta + \Delta\theta\right)\left(\mathbf{q} + \Delta\mathbf{q}\right) \tag{A.2.9}$$

respectively.

Using Taylor's theorem, the nonlinear part of Equation (A.2.9) can be expanded as:

$$\mathbf{G}\left(\theta + \Delta\theta\right) \approx \mathbf{G}\left(\theta\right) + \partial_\theta \mathbf{G}\left(\theta\right) \cdot \Delta\theta, \tag{A.2.10}$$

where, the notation $\partial_\theta \mathbf{G}\left(\theta\right)$ represents the derivative with respect to each component of θ. If θ has i components, $\partial_\theta \mathbf{G}\left(\theta\right) \cdot \Delta\theta$ is understood in the same fashion as in the vector dot product

$$\begin{aligned} &\begin{pmatrix} \partial_{\theta_1}\mathbf{G}\left(\theta\right) & \partial_{\theta_2}\mathbf{G}\left(\theta\right) & \cdots & \partial_{\theta_i}\mathbf{G}\left(\theta\right) \end{pmatrix} \begin{pmatrix} \Delta\theta_1 \\ \Delta\theta_2 \\ \vdots \\ \Delta\theta_i \end{pmatrix} \\ &= \partial_{\theta_1}\mathbf{G}\left(\theta\right) \cdot \Delta\theta_1 + \partial_{\theta_2}\mathbf{G}\left(\theta\right) \cdot \Delta\theta_2 + \cdots + \partial_{\theta_i}\mathbf{G}\left(\theta\right) \cdot \Delta\theta_i \end{aligned} \tag{A.2.11}$$

Using Equation (A.2.10) to expand Equation (A.2.9) and leaving out the second order differential gives

$$\begin{aligned}
&\mathbf{G}\left(\mathbf{m}+\Delta\mathbf{m}\right)\\
&=\mathbf{G}\left(\theta+\Delta\theta\right)\left(\mathbf{q}+\Delta\mathbf{q}\right)\\
&\approx\left[\mathbf{G}\left(\theta\right)+\partial_{\theta}\mathbf{G}\left(\theta\right)\cdot\Delta\theta\right]\left(\mathbf{q}+\Delta\mathbf{q}\right)\\
&\approx\mathbf{G}\left(\theta\right)\mathbf{q}+\mathbf{G}\left(\theta\right)\Delta\mathbf{q}+\partial_{\theta}\left[\mathbf{G}\left(\theta\right)\mathbf{q}\right]\cdot\Delta\theta
\end{aligned}. \tag{A.2.12}$$

Rewrite Equation (A.2.12), so that the relation between Equation (A.2.12) and Equation (A.2.1) can be seen more clearly,

$$\begin{aligned}
&\mathbf{G}\left(\mathbf{m}+\Delta\mathbf{m}\right)=\mathbf{G}\left(\theta+\Delta\theta\right)\left(\mathbf{q}+\Delta\mathbf{q}\right)\\
&\approx\mathbf{G}\left(\theta\right)\mathbf{q}+\begin{pmatrix}\mathbf{G}\left(\theta\right) & \partial_{\theta}\left[\mathbf{G}\left(\theta\right)\mathbf{q}\right]\end{pmatrix}\begin{pmatrix}\Delta\mathbf{q}\\ \Delta\theta\end{pmatrix}
\end{aligned} \tag{A.2.13}$$

Comparing the above equation (A.2.13) with Equation (A.2.1) shows that the Jacobian in Equation (A.2.2) is

$$\mathbf{J}\left(\mathbf{m}\right)=\mathbf{J}\left(\mathbf{q},\theta\right)=\begin{pmatrix}\mathbf{G}\left(\theta\right) & \partial_{\theta}\left[\mathbf{G}\left(\theta\right)\mathbf{q}\right]\end{pmatrix} \tag{A.2.14}$$

Let

$$\mathbf{m}'=\mathbf{m}+\Delta\mathbf{m}=\begin{pmatrix}\mathbf{q}'\\ \theta'\end{pmatrix}=\begin{pmatrix}\mathbf{q}\\ \theta\end{pmatrix}+\begin{pmatrix}\Delta\mathbf{q}\\ \Delta\theta\end{pmatrix}, \tag{A.2.15}$$

where $\mathbf{m}=\begin{pmatrix}\mathbf{q} & \theta\end{pmatrix}^{T}$ and $\Delta\mathbf{m}=\begin{pmatrix}\Delta\,\mathbf{q} & \Delta\theta\end{pmatrix}^{T}$. Substituting Equation (A.2.15), (A.2.14) and (A.2.8) into Occam's algorithm Equation (A.2.6) gives the formulation of Occam's algorithm where linear and nonlinear parameters are separated

$$\begin{cases}
\min\limits_{(\mathbf{q}',\theta')}\left\{\left\|\begin{pmatrix}\mathbf{G}\left(\theta\right) & \partial_{\theta}\left[\mathbf{G}\left(\theta\right)\mathbf{q}'\right]\end{pmatrix}\begin{pmatrix}\mathbf{q}'\\ \theta'\end{pmatrix}-\widehat{\mathbf{d}}\left(\mathbf{q},\theta\right)\right\|_{2}^{2}+\alpha^{2}\left\|\mathbf{L}\begin{pmatrix}\mathbf{q}'\\ \theta'\end{pmatrix}\right\|_{2}^{2}\right\}\\
\widehat{\mathbf{d}}\left(\mathbf{q},\theta\right)=\mathbf{d}+\partial_{\theta}\left[\mathbf{G}\left(\theta\right)\mathbf{q}\right]\cdot\theta
\end{cases}. \tag{A.2.16}$$

If regularizations of the inversion only target slip parameters, and nonlinear parameters are not regulated, the above equation (A.2.16) becomes:

$$\begin{cases} \min\limits_{(\mathbf{q}',\theta')} \left\{ \left\| \begin{pmatrix} \mathbf{G}(\theta) & \partial_\theta [\mathbf{G}(\theta)\,\mathbf{q}'] \end{pmatrix} \begin{pmatrix} \mathbf{q}' \\ \theta' \end{pmatrix} - \widehat{\mathbf{d}}(\mathbf{q},\theta) \right\|_2^2 + \alpha^2 \|\mathbf{L}\mathbf{q}'\|_2^2 \right\} \\ \widehat{\mathbf{d}}(\mathbf{q},\theta) = \mathbf{d} + \partial_\theta [\mathbf{G}(\theta)\,\mathbf{q}] \cdot \theta \end{cases}, \quad \text{(A.2.17)}$$

and in another equivalent form

$$\begin{cases} \min\limits_{(\mathbf{q}',\theta')} \left\{ \left\| \mathbf{G}(\theta)\,\mathbf{q}' + \partial_\theta [\mathbf{G}(\theta)\,\mathbf{q}'] \cdot \theta' - \widehat{\mathbf{d}}(\mathbf{q},\theta) \right\|_2^2 + \alpha^2 \|\mathbf{L}\mathbf{q}'\|_2^2 \right\} \\ \widehat{\mathbf{d}}(\mathbf{q},\theta) = \mathbf{d} + \partial_\theta [\mathbf{G}(\theta)\,\mathbf{q}] \cdot \theta \end{cases}. \quad \text{(A.2.18)}$$

APPENDIX B

MATHEMATICAL FORMULATION FOR VISCOELASTIC DEFORMATION

Earthquake rupture causes elastic deformation, as well as viscoelastic relaxation if the viscoelastic layer is affected by the coseismic stress change. *Pollitz* [1996, 1997] formulate these two problems on a spherically symmetric Earth model. Putting his formulation together, if we treat slip on the fault as input, and observed total deformation (including both elastic and viscous) on the ground as output, the input-output pair forms the so-called linear time-invariant system (LIT system). In this section, we will first discuss the basic formulation of this system (section B.1). Based on it, we then will further decompose the coseismic and postseismic deformation into four parts (section B.2, B.3, and B.4). The mathematical formulation discussed in this section provides the basis for slip inversion and results analysis in the following sections.

B.1 Earth media response to fault slip as an LTI system

Let $\mathbf{d}(t)$ be the data vector representing displacement at GPS sites, $s_\alpha(t)$ be the reverse slip on subfaults α, and $v_\alpha(t) = \dot{s_\alpha}(t)$ is the corresponding slip rate. The viscoelastic Earth media responds to fault slips at depth, and the deformation on the surface is recorded by GPS stations. If we treat fault slip rate $v_\alpha(t)$ as input and observed time series $\mathbf{d}(t)$ as output, the system forms the so-called linear time-invariant system (LTI system).

The impulse input of the LTI system is $v_\alpha(t) = \delta(t)$, where $\delta(t)$ is the Dirac delta function. The corresponding slip input for impulse slip rate input is $s_\alpha(t) = H(t)$, where $H(t)$ is the Heaviside step function. For a given impulse input $v_\alpha(t) = \delta(t)$, represent the impulse response recorded at sites as $\mathbf{g}_\alpha(t)$. Because the system is

linear time-invariant, it can be described by the following formula

$$\mathbf{d}(t) = \sum_{\alpha} \int_{-\infty}^{+\infty} v_{\alpha}(\tau)\, \mathbf{g}_{\alpha}(t-\tau)\, d\tau, \tag{B.1.1}$$

where the summation sign $\sum_{\alpha}$ means summation over all subfaults.

For convenience of numerical computation, equation (B.1.1) can be rewritten in vector/matrix form:

$$D(t) = \int_{-\infty}^{+\infty} G(t-\tau)\, V(\tau)\, d\tau, \tag{B.1.2}$$

where $D(t)$ is a column vector representing all observations at time t; notation $V(t)$ is a column vector representing slip velocities across subfaults at time t; and notation $G(t)$ is a matrix, which is often called Green's function of impulse input at time t. If the shape of the column vector $D(t)$ is $m \times 1$ and the shape of the column vector $V(t)$ is $n \times 1$, then the size of matrix $G(t)$ is $m \times n$.

We assume the earthquake happens at $t = 0$, and fault slips only happen when $t \geq 0$. This means that $V(t) = \mathbf{0}$, when $t < 0$. The system is causal, which means $G(t) = \mathbf{0}$, when $t < 0$. With these assumptions, the infinite interval of the integral (B.1.2) can be refined to $[0, t]$:

$$D(t) = \int_{0-}^{t} G(t-\tau)\, V(\tau)\, d\tau, \tag{B.1.3}$$

where the minus sign after 0 is used to stress the fact that, at $t = 0$, when coseismic slip happens instantaneously, $V(0)$ is a delta function (see equation (B.3.1)) and is included in the integral.

In equation (B.1.3), the Green's function $G(t)$ can be decomposed into two parts, elastic and viscous part, based on the nature of the deformation, and the slip input $V(t)$ can be decomposed into two parts as well: coseismic slip and afterslip, based on the timing of slips. Thus the deformation term $D(t)$ ultimately has four parts. The following sections (section B.2, B.3, and B.4) will elaborate on this.

B.2 Elastic deformation versus viscous flow

For an Earth model with both elastic and viscoelastic layer, when slip (no matter coseismic slip or afterslip) happens across the faults, two kinds of deformation will be triggered. The first kind is elastic deformation due to static dislocation. The second kind is viscous flow within the viscoelastic layer resulting from stress change. For a spherically layered earth model, the elastic and viscous deformation can be computed with the method proposed by *Pollitz* [1996, 1997] and *Pollitz* [1992], respectively. The corresponding software packages are called STATIC1D and VISCO1D, respectively, which are all available online. Therefore, the Green's function $G(t)$ in Equation (B.1.3) can be separated into two parts, G^E, the elastic response, and $G^R(t)$, the viscous response

$$G(t) = G^E + G^R(t) \tag{B.2.1}$$

Note that the elastic response of the earth is instantaneous, thus G^E is not a function of time, while viscous relaxation is a stress triggered temporal process, thus $G^R(t)$ is a function of time.

Substitute Equation (B.2.1) into Equation (B.1.2), we obtain

$$D(t) = E(t) + R(t) \tag{B.2.2a}$$

$$E\,(t) \equiv G^E S\,(t) \tag{B.2.2b}$$

$$R\,(t) \equiv \int_{0-}^{t} G^R\,(t-\tau)\,V\,(\tau)\,d\tau \tag{B.2.2c}$$

where $E(t)$ is called elastic deformation, $R(t)$ is called viscous deformation, and $S\,(t) = \int_{0-}^{t} V\,(\tau)\,d\tau$ is the total slip (coseismic slip + afterslip) across the fault plane.

B.3 Coseismic slip versus afterslip

We haven't distinguished between coseismic slip and afterslip in the above formulation. The main difference between these two is that coseismic slip happens instantaneously at the time of the earthquake ($t = 0$), while afterslip is a creeping movement that happens continuously at $t > 0$. Mathematically, this means that coseismic slip is represented by a discontinuity in the slip function, or equivalently, a delta function in the slip rate function. Suppose the coseismic slip magnitude is S^{co}, then $V(t)$ can be written into two parts,

$$V(t) = \begin{cases} S^{\text{co}}\delta(t) & (t = 0) \\ V^{\text{aslip}}(t) & (t > 0) \end{cases}, \tag{B.3.1}$$

where $V^{\text{aslip}}(t)$ is the afterslip rate. The time integral of $V(t)$ is slip $S(t)$. The relation between $V(t)$ and $S(t)$ is described in

$$S(t) = \int_{0-}^{t} V(\tau)\, d\tau \tag{B.3.2a}$$

$$S(t) = S^{co} + S^{\text{aslip}}(t) \tag{B.3.2b}$$

$$S^{aslip}(t) \equiv \int_{0+}^{t} V^{\text{aslip}}(\tau)\, d\tau \tag{B.3.2c}$$

.

Substitute equation (B.3.1) into equation (B.1.3), we get

$$D(t) = D^{\text{co}}(t) + D^{\text{aslip}}(t) \tag{B.3.3a}$$

$$D^{\text{co}}(t) \equiv S^{\text{co}} G(t) \tag{B.3.3b}$$

$$D^{\text{aslip}}(t) \equiv \int_{0+}^{t} G(t-\tau)\, V^{\text{aslip}}(t)\, d\tau \tag{B.3.3c}$$

, where $D^{co}(t)$ is called coseismic slip triggered deformation and $D^{\text{aslip}}(t)$ is called afterslip triggered deformation. Note that the plus sign after zero means that the integral doesn't include coseismic slip rate impulse.

B.4 Four parts of deformation

Based on the discussion in the last two sections (Section B.2 and B.3), the overall deformation can be decomposed into four parts: (1) E^{co}, coseismic slip caused elastic deformation; (2) $E^{\text{aslip}}(t)$, afterslip caused elastic deformation; (3) $R^{\text{co}}(t)$, coseismic slip triggered viscous deformation; (4) $R^{\text{aslip}}(t)$, afterslip triggered viscous deformation:

$$D(t) = E^{\text{co}} + E^{\text{aslip}}(t) + R^{\text{co}}(t) + R^{\text{aslip}}(t) \tag{B.4.1a}$$

$$E^{\text{co}} \equiv G^{\text{E}} S^{co} \tag{B.4.1b}$$

$$E^{\text{aslip}}(t) \equiv G^{E} S^{\text{aslip}}(t) \tag{B.4.1c}$$

$$R^{\text{co}}(t) \equiv S^{\text{co}} G^{R}(t) \tag{B.4.1d}$$

$$R^{\text{aslip}}(t) \equiv \int_{0+}^{t} G^{R}(t-\tau)\, V^{\text{aslip}}(t)\, d\tau \tag{B.4.1e}$$

Equations (B.4.1) can be obtained by either substitute Equation (B.2.1) into Equation (B.3.3) or substitute Equation (B.3.1) into Equation (B.2.2).

B.5 Discretization of the convolutional integral

Equation (B.1.3) is in a form that is often called time convolution. Vector $D(t)$ is the so-called cumulative postseismic displacement (coseismic + postseismic displacements), which can be extracted from continuous GPS position time series. With the Green's function $G(t)$ computed by methods developed by *Pollitz* [1992, 1996, 1997], we can invert GPS observations for the slip history ($V(t)$ and $S(t)$) on the fault plane. The inversion based on convolution Equation (B.1.3) is also known as deconvolution. In this section, we discuss how to numerically deconvolve the integral equation (B.1.3) by discretizing it into matrix equations.

Suppose the considered deformation period is $[0, T]$, and it can be discretized

into r time sections:

$$t_0, t_1, t_2, \cdots, t_r.$$

The corresponding intervals are:

$$\Delta_1 = t_1 - t_0, \Delta_2 = t_2 - t_1, \cdots, \Delta_r = t_r - t_{r-1}. \tag{B.5.1}$$

Since coseismic slip and afterslip is already separated in Equation (B.3.3), we use it as the starting point of the discretization, and rewrite it as:

$$D(t) = S^{\text{co}} G(t) + \int_{0+}^{t} G(t-\tau)\, V^{\text{aslip}}(t)\, d\tau \tag{B.5.2}$$

Apply the intervals defined in (B.5.1) to Equation (B.5.2), and we have

$$D(t_i) = S^{co} G(t_0) + \sum_{j=1,\cdots,i} G(t_i - t_j)\, V^{\text{aslip}}(t_j)\, \Delta_j \quad (i = 0, \cdots, r)\ . \tag{B.5.3}$$

Define $T_i (i = 0, \cdots, r)$ as

$$\begin{cases} T_0 = S^{\text{co}} \\ T_i = V^{\text{aslip}}(t_i)\, \Delta_i \end{cases}.$$

The notation $T_i (i > 0)$, represent the slip in time interval Δ_i, and T_0 is coseismic slip. Let $D_i = D(t_i)$, and equation (B.5.3) can be written in more unified form

$$D_i = \sum_{j=0,\cdots,i} G(t_i - t_j)\, T_j \quad (i = 0, \cdots, r) \tag{B.5.4}$$

Rewrite equation (B.5.4) into matrix form:

$$\begin{pmatrix} D_0 \\ D_1 \\ D_2 \\ D_3 \\ \vdots \\ D_r \end{pmatrix} = \begin{pmatrix} G(0) & 0 & 0 & 0 & \cdots & 0 \\ G(t_1) & G(0) & 0 & 0 & \cdots & 0 \\ G(t_2) & G(t_2 - t_1) & G(0) & 0 & \cdots & 0 \\ G(t_3) & G(t_3 - t_1) & G(t_3 - t_2) & G(0) & & 0 \\ \vdots & \vdots & \vdots & \vdots & & \vdots \\ G(t_r) & G(t_r - t_1) & G(t_r - t_2) & G(t_r - t_3) & \cdots & G(0) \end{pmatrix} \begin{pmatrix} T_0 \\ T_1 \\ T_2 \\ T_3 \\ \vdots \\ T_r \end{pmatrix} \tag{B.5.5}$$

Let $\mathbb{D} = \begin{pmatrix} D_0 & D_1 & D_2 & D_3 & \cdots & D_r \end{pmatrix}^T$, $\mathbb{T} = \begin{pmatrix} T_0 & T_1 & T_2 & T_3 & \cdots & T_r \end{pmatrix}^T$, and

$$\mathbb{G} = \begin{pmatrix} G(0) & 0 & 0 & 0 & \cdots & 0 \\ G(t_1) & G(0) & 0 & 0 & \cdots & 0 \\ G(t_2) & G(t_2 - t_1) & G(0) & 0 & \cdots & 0 \\ G(t_3) & G(t_3 - t_1) & G(t_3 - t_2) & G(0) & & 0 \\ \vdots & \vdots & \vdots & \vdots & & \vdots \\ G(t_r) & G(t_r - t_1) & G(t_r - t_2) & G(t_r - t_3) & \cdots & G(0) \end{pmatrix}.$$

Equation (B.5.5), represented as $\mathbb{D} = \mathbb{G}\mathbb{T}$, forms the basis of inversion. In the context of inversion theory, vector $\mathbb{D}$ is called data, vector $\mathbb{T}$ is called model parameters, and matrix $\mathbb{G}$ is called data kernel, which is the operator that connects data and model parameters.

APPENDIX C

SOME PUBLISHED COSEISMIC SLIP INVERSION RESULTS

C.1 *Ozawa et al.* [2011]

Data: GPS coseismic offsets

Max Slip: 27m

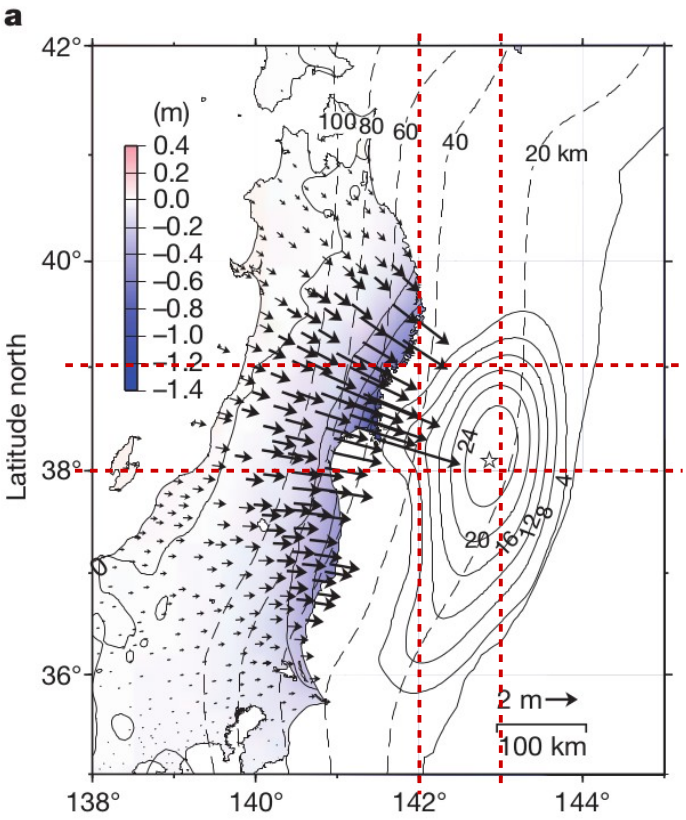

Figure C.1: *Ozawa et al.* [2011]

C.2 *Ozawa et al.* [2012]

Data: Onshore GPS and seafloor GPS

Max Slip: Approximately 60 m.

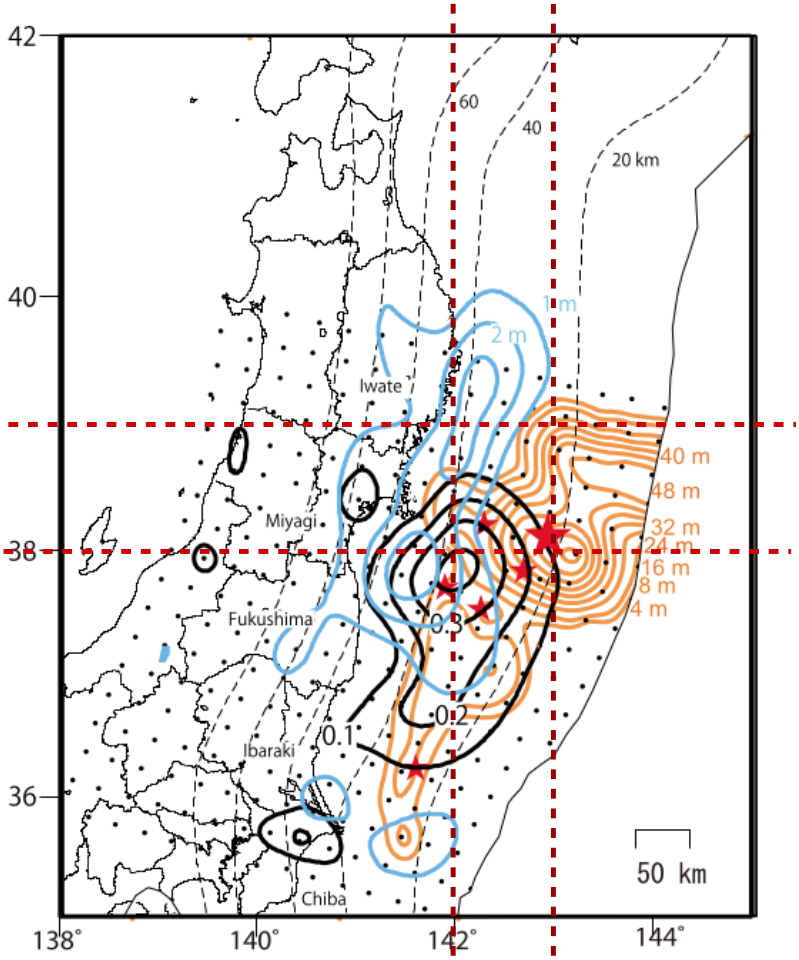

Figure 12. Preceding aseismic slip (black contours with an interval of 0.1 m), coseismic slip of the Tohoku earthquake (red contours with an interval of 8 m), and afterslip of the Tohoku earthquake (blue contours with an interval of 1 m). Since the slip magnitude is very different among the three events, we varied the contour interval as shown in this figure. The center of the preceding aseismic slip is located between the centers of the coseismic slip and afterslip of the Tohoku earthquake. Small stars indicate the epicenters of the five subduction earthquakes (see text). The large star shows the epicenter of the Tohoku earthquake.

Figure C.2: *Ozawa et al.* [2012]

C.3 *Pollitz et al.* [2011]

Data: Onshore GPS and seafloor GPS

Max Slip: 33 m.

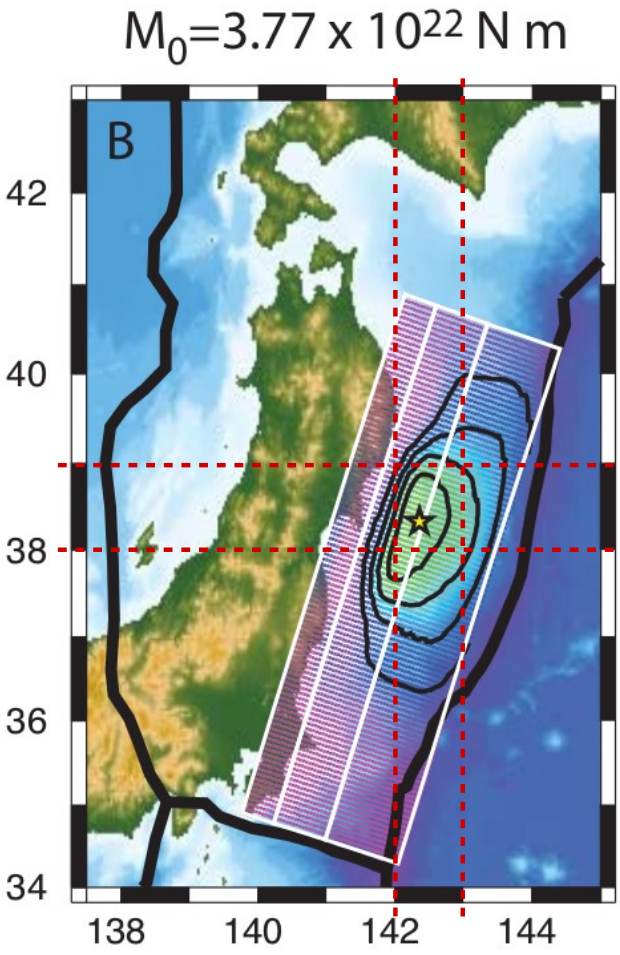

Figure C.3: *Pollitz et al.* [2011]

C.4 *Yokota et al.* [2011]

Data: Strong motion, teleseismic, geodetic, tsunami

	Strong Motion	Teleseismic	Geodetic	Tsunami	Joint
Max slip(m)	31	25	31	38	35
Moment($Pa \cdot s$)	4.2×10^{22}	4.3×10^{22}	4.0×10^{22}	3.4×10^{22}	4.2×10^{22}
M_w	9.08	9.09	9.06	9.02	9.08

Table C.1: *Yokota et al.* [2011] coseismic slip inversion results summarized.

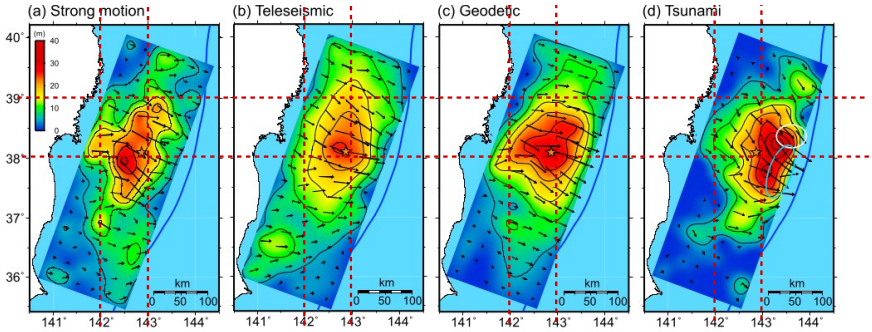

Figure 3. Slip distributions obtained by the separate inversions of (a) strong motion, (b) teleseismic, (c) geodetic, and (d) tsunami datasets. Arrows indicate the subfault slips on the hanging wall. The white circle and the sky-blue ellipse in Figure 3d denote the compact shallow rupture and the area to its south, respectively.

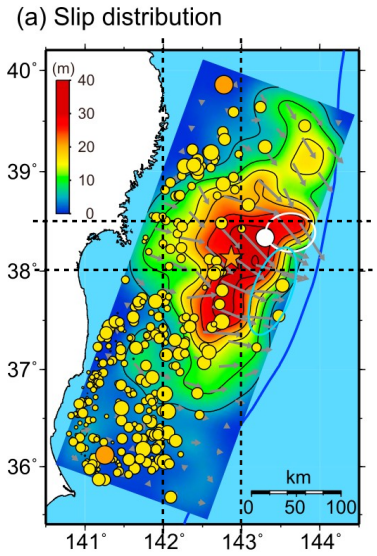

Figure C.4: *Yokota et al.* [2011]

C.5 *Ito et al.* [2011]

Max slip: 60 m

Mo: 4.1E23 Nm (typo here?)

Mw: 9.0

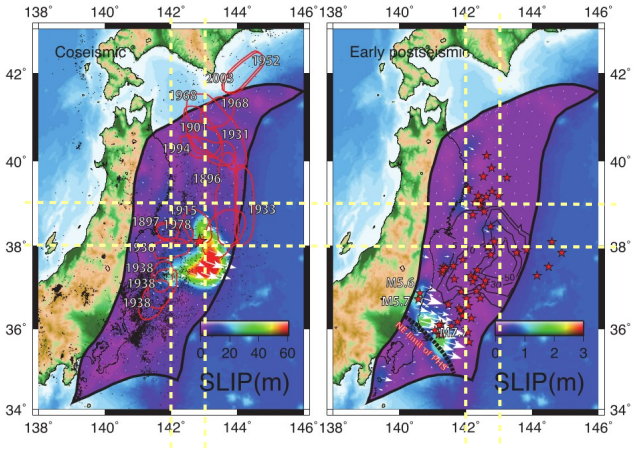

Fig. 2. Estimated coseismic (left) and postseismic (right) slip distribution. Colors and white arrows denote the absolute amount and direction of the fault slip, respectively. Red ellipses in the left panel are the estimated source regions of past earthquakes (The Headquarters for Earthquake Research Promotion, 1999). Red star and black dots are the hypocenter of the main shock and aftershocks determined by JMA. The contour lines in the right panel show the coseismic slip distribution, and the black broken line shows the northeastern end of the Philippine Sea plate. Red stars are aftershock epicenters lager than *M* 5.5 from 14:55 to 23:00 on 11 March.

Figure C.5: *Ito et al.* [2011]

C.6 *Simons et al.* [2011]

Note that Minson is the second author, therefore results reported here are very similar to (Minson et al., 2014).

Data used: GPS coseismic off-sets, sea-floor pressure gauge data.

Max slip: with peak displacement of around 60m

Inverted moment: 8.8 to 9.2 We estimated probability distributions for derived scalar rupture quantities including rupture are, potency, scalar seismic moment, and static stress drop.

Estimates of moment magnitude range from 8.8 to 9.2

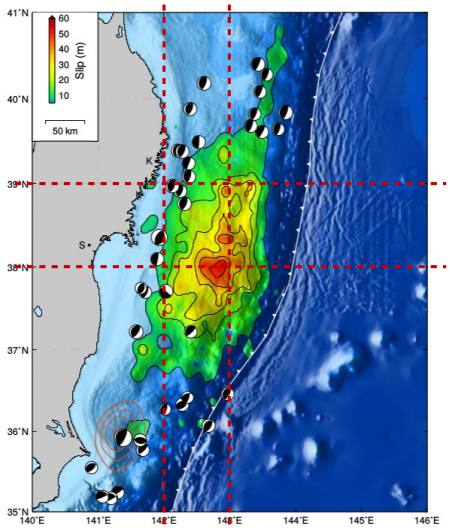

Fig. S2
Inferred distribution of subsurface fault slip (color with superimposed contours at 8 m intervals) constrained by GPS and tsunami observations and derived from an unregularized Bayesian estimation method (*6, 41*). The black focal mechanisms are GCMT solutions for a period of 34 days following the mainshock. Only events with thrust mechanisms are shown.

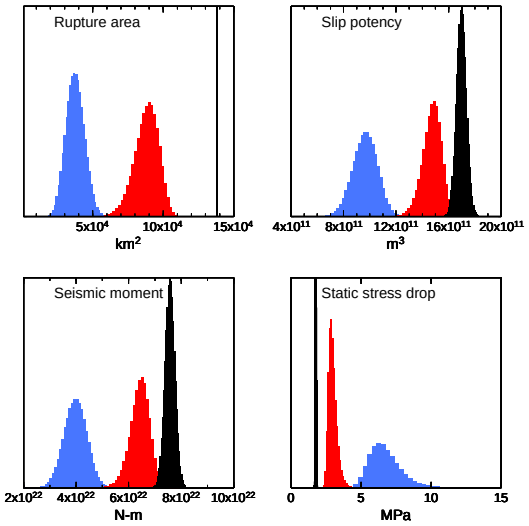

Fig. S4
A posteriori PDFs for derived quantities including rupture area, potency, scalar seismic mome and static stress drop. We consider three different thresholds to define the extent of the earthquake rupture: the entire fault model (black), areas that slipped in excess of 10% of the maximum slip (red), and in excess of 20% of the maximum slip (blue).

Figure C.6: *Simons et al.* [2011]

C.7 *Minson et al.* [**2014**]

Data: 1Hz kinematic GPS, static GPS offsets, seafloor geodesy and near-field and far-field tsunami data

Moment release: Mw 9.2

Slip distribution:

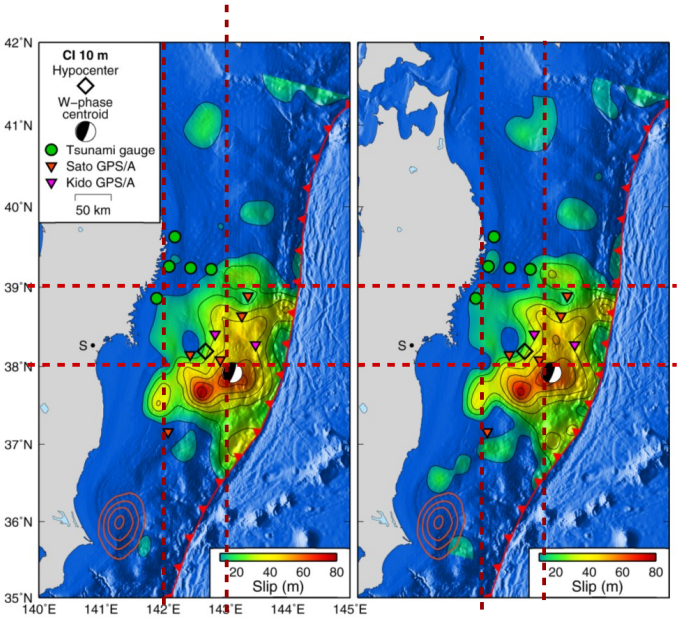

Figure 2. Mean posterior slip distribution from static inversion (left-hand panel) and joint kinematic-static inversion (right-hand panel). The mean of the posterior PDF for the static displacements on the fault plane is shown. Green circles, red triangles, and pink triangles mark the locations of seafloor geodesy and near-field tsunami records. The black diamond is the location of the Chu *et al.* (2011) hypocentre. The W-phase focal mechanism of Duputel *et al.* (2011) is shown at its centroid location. Red contour lines denote slip model for largest aftershock from Simons *et al.* (2011) shown with a contour interval of 1 m. The location of the city of Sendai is marked by the letter S.

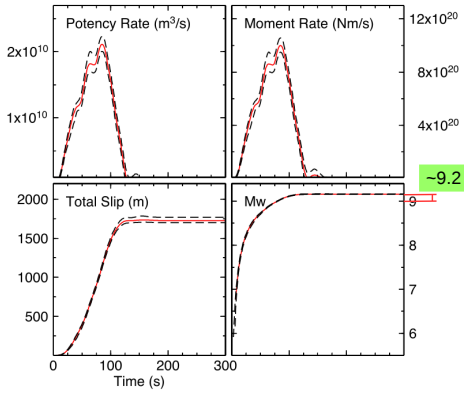

Figure 16. History of moment release. The mean potency rate function, moment rate function, total slip accumulated, and total moment magnitude released are plotted as a function of time with red lines. The black dashed lines represent 95 per cent credibility intervals calculated from the posterior PDF.

Figure C.7: *Minson et al.* [2014]

APPENDIX D

COSEISMIC DISPLACEMENTS

Coseismic displacements estimated based on time series modeling are listed in the following table (Table D.1).

ID	Latitude	Longitude	EW(m)	NS(m)	UD(m)	ID	Latitude	Longitude	EW(m)	NS(m)	UD(m)
019B	139.5477	39.1856	0.7932	-0.3131	0.0389	AIRA	130.6000	31.8240	0.0124	0.0058	-0.0034
BADG	102.2350	51.7697	0.0026	-0.0014	-0.0011	BJFS	115.8920	39.6090	0.0062	0.0003	0.0002
CCJ2	142.2000	27.0700	0.0035	-0.0001	-0.0017	CHAN	125.4440	43.7910	0.0184	-0.0085	0.0013
CNMR	145.7430	15.2300	-0.0025	0.0005	-0.0005	CUSV	100.5339	13.7359	-0.0032	-0.0024	-0.0032
DAEJ	127.3740	36.3990	0.0225	0.0031	0.0008	1000	135.9283	33.8770	0.0314	0.0141	0.0034
1001	135.0876	35.4195	0.0663	0.0165	0.0058	1002	135.3407	35.3335	0.0666	0.0185	0.0116
1003	135.6342	35.1552	0.0615	0.0167	0.0080	1004	135.2199	34.3265	0.0383	0.0127	0.0004
1006	134.3761	34.7604	0.0430	0.0130	0.0031	1007	136.0419	34.7106	0.0520	0.0153	0.0031
1008	136.1731	34.4939	0.0450	0.0170	0.0054	1009	136.0026	34.2929	0.0405	0.0169	0.0014
1010	135.8548	34.2420	0.0387	0.0121	0.0051	1011	135.5540	33.9408	0.0322	0.0137	0.0024
1012	135.8821	33.6688	0.0287	0.0111	0.0018	1013	135.5338	33.6583	0.0278	0.0082	-0.0033
1014	134.1953	35.5299	0.0573	0.0128	0.0036	1015	133.4951	35.5069	0.0502	0.0106	0.0009
1016	133.8698	35.4932	0.0533	0.0127	0.0032	1017	134.1559	35.3406	0.0514	0.0132	0.0007
1018	132.9220	35.4919	0.0501	0.0131	-0.0009	1019	133.1921	35.3107	0.0490	0.0148	-0.0022
1020	132.9027	35.3097	0.0475	0.0125	-0.0013	1021	132.6690	35.2331	0.0440	0.0134	-0.0036
1022	132.3856	35.0319	0.0399	0.0123	0.0003	1023	132.6852	34.8567	0.0397	0.0120	-0.0054
1024	132.1095	34.7779	0.0354	0.0107	-0.0023	1025	131.8103	34.6243	0.0331	0.0067	-0.0033
1026	133.6808	35.2830	0.0488	0.0142	0.0048	1027	133.9127	35.1050	0.0482	0.0154	0.0007
1028	133.8004	34.7381	0.0388	0.0110	0.0010	1029	133.9726	34.5903	0.0380	0.0108	0.0003
1030	132.9021	35.0352	0.0414	0.0126	-0.0005	1031	132.9081	34.6337	0.0377	0.0127	-0.0022
1032	133.3413	34.6122	0.0392	0.0156	-0.0053	1033	133.1402	34.5156	0.0362	0.0120	-0.0020
1035	132.6920	34.1846	0.0332	0.0102	0.0017	1036	132.5316	34.0692	0.0300	0.0103	-0.0007
1037	131.7353	34.1953	0.0301	0.0082	-0.0014	1038	132.0527	34.0901	0.0292	0.0091	-0.0030
1039	131.1130	34.0205	0.0259	0.0078	-0.0014	1040	132.1200	33.8459	0.0278	0.0067	-0.0034
1041	134.4573	33.9937	0.0319	0.0129	0.0042	1042	134.2112	33.9346	0.0305	0.0123	-0.0001
1044	134.1760	34.4785	0.0372	0.0104	0.0024	1045	133.8994	34.3259	0.0338	0.0104	0.0015
1046	133.3507	33.9742	0.0297	0.0135	-0.0025	1047	133.0474	33.8841	0.0267	0.0121	-0.0040
1048	132.7985	33.6427	0.0268	0.0078	-0.0042	1049	132.7437	33.3051	0.0242	0.0100	-0.0069
1050	132.6336	33.0961	0.0215	0.0094	-0.0039	1051	133.5310	33.6258	0.0264	0.0085	0.0062
1022	133.1545	33.6070	0.0262	0.0123	-0.0020	1023	134.0993	33.4971	0.0262	0.0107	0.0083
1054	133.0895	33.4167	0.0235	0.0101	0.0031	1055	134.2055	33.3949	0.0246	0.0106	-0.0026
1056	132.9721	33.1931	0.0218	0.0086	0.0025	1058	132.8315	32.9611	0.0200	0.0094	-0.0001
1059	132.5554	32.7386	0.0189	0.0082	0.0008	1060	130.7224	33.9297	0.0242	0.0079	-0.0030
1061	130.9711	33.8670	0.0235	0.0049	0.0115	1062	130.2969	33.6831	0.0223	0.0076	-0.0083
1063	130.6757	33.5798	0.0219	0.0063	-0.0042	1064	130.9954	33.5647	0.0266	0.0075	-0.0035

1065	130.0793	33.5030	0.0197	0.0069	-0.0009	1066	130.0972	33.2920	0.0192	0.0072	-0.0058
1067	129.8629	33.0734	0.0168	0.0069	-0.0002	1068	129.9590	32.7683	0.0138	0.0081	-0.0068
1069	130.6218	33.0601	0.0182	0.0066	0.0011	1070	130.8727	32.9959	0.0196	0.0066	-0.0013
1071	130.7484	32.7092	0.0175	0.0057	-0.0033	1073	130.8273	32.3961	0.0160	0.0058	-0.0040
1074	130.1799	32.3674	0.0145	0.0063	0.0020	1075	130.6565	32.3435	0.0144	0.0052	0.0006
1076	130.9864	32.2924	0.0146	0.0067	-0.0045	1077	131.5211	33.5143	0.0258	0.0096	-0.0045
1078	131.2917	33.3838	0.0250	0.0074	-0.0060	1079	131.7484	33.0962	0.0210	0.0077	-0.0061
1080	132.0390	32.9364	0.0205	0.0078	0.0013	1081	131.4415	32.8989	0.0205	0.0067	-0.0072
1082	131.6292	32.8522	0.0205	0.0071	-0.0044	1083	131.3647	32.5279	0.0168	0.0062	-0.0037
1084	131.5830	32.3162	0.0134	0.0057	-0.0004	1085	131.3475	32.1119	0.0111	0.0057	-0.0022
1086	131.2545	32.0018	0.0102	0.0066	-0.0013	1087	130.9770	31.8778	0.0105	0.0059	-0.0043
1088	131.4701	31.7860	0.0106	0.0072	0.0024	1089	130.7357	31.7438	0.0103	0.0052	0.0006
1090	130.9983	31.5646	0.0096	0.0054	-0.0020	1091	130.3401	31.4503	0.0114	0.0063	-0.0043
1092	130.5406	31.3772	0.0128	0.0054	-0.0010	1093	130.8671	31.2427	0.0113	0.0073	-0.0037
1094	127.9937	26.3863	0.0047	-0.0002	-0.0019	1095	127.7604	26.3127	0.0034	0.0008	-0.0041
1096	127.6776	26.1946	0.0016	-0.0013	0.0039	1098	153.9787	24.2901	-0.0074	0.0084	-0.0061
1099	137.5508	36.1143	0.1805	0.0518	-0.0027	1100	138.7273	35.3608	0.1241	0.0507	0.0064
1101	140.8583	43.2095	0.0275	-0.0524	-0.0020	1102	139.4892	42.0788	0.1098	-0.1247	0.0102
1103	140.8592	40.8975	0.2661	-0.3155	0.0303	1104	139.7035	39.9421	0.5634	-0.3313	0.0382
1105	139.5460	38.5633	1.0158	-0.2494	0.0232	1107	140.2495	35.1294	0.0994	0.0092	-0.0271
1108	139.6155	35.1602	0.1078	0.0252	-0.0042	1109	138.2812	37.8148	0.4648	-0.0336	0.0309
1110	138.5085	37.3565	0.4784	-0.0074	0.0340	1111	136.9003	37.4057	0.2300	0.0028	0.0166
1112	136.1488	36.2546	0.1190	0.0204	0.0102	1113	139.1330	34.8955	0.0699	0.0314	0.0047
1114	138.7642	34.8069	0.0623	0.0225	0.0006	1115	138.3274	34.8707	0.0756	0.0234	0.0041
1116	136.8238	34.9040	0.0653	0.0214	0.0037	1117	135.1915	34.1441	0.0349	0.0156	0.0028
1118	134.3159	35.5937	0.0615	0.0150	0.0064	1119	131.6046	34.6276	0.0316	0.0080	-0.0039
1120	133.2435	33.3335	0.0278	0.0097	0.0028	1121	129.8493	33.4731	0.0196	0.0057	-0.0034
1122	134.1781	33.2661	0.0220	0.0088	0.0048	1123	130.1911	32.0174	0.0124	0.0055	-0.0085
1124	127.8247	26.1795	0.0006	0.0015	-0.0021	1125	132.9822	32.8695	0.0237	0.0096	-0.0086
1126	132.8107	32.7621	0.0207	0.0082	-0.0113	1127	137.8145	35.7775	0.1437	0.0365	0.0118
1128	136.7287	35.4051	0.0859	0.0275	0.0108	1129	136.4319	34.6033	0.0502	0.0161	0.0052
1130	135.5899	33.7476	0.0288	0.0087	0.0015	1131	133.9409	33.7225	0.0282	0.0114	0.0002
1132	133.0432	33.5458	0.0245	0.0099	0.0033	1133	132.4888	33.0395	0.0220	0.0093	-0.0039
1134	132.9227	33.3910	0.0250	0.0102	-0.0041	1135	133.6996	35.4904	0.0547	0.0128	0.0071
1136	137.6369	34.7021	0.0636	0.0212	0.0098	1137	131.3840	33.0788	0.0206	0.0114	-0.0108
1138	137.5960	36.5770	0.2307	0.0290	0.0118	1139	136.5405	34.2851	0.0409	0.0129	0.0006
1140	136.0811	20.4255	-0.0019	-0.0044	0.0020	1141	132.9617	33.1039	0.0218	0.0089	0.0002
1142	132.6758	32.9277	0.0209	0.0080	0.0006	1143	136.2956	34.9307	0.0620	0.0180	0.0096
1144	138.7947	34.9706	0.0789	0.0274	0.0058	1145	141.2832	38.9019	3.2136	-1.4640	-0.2582
1146	135.4261	34.0855	0.0348	0.0136	0.0051	1147	131.8350	34.0438	0.0283	0.0102	-0.0098
1148	136.7282	34.4900	0.0489	0.0145	0.0048	1149	136.6932	34.2966	0.0427	0.0124	-0.0010
1150	140.8988	42.5579	0.0509	-0.0824	0.0011	1151	132.6503	34.4921	0.0345	0.0121	-0.0008
1152	133.9241	33.6223	0.0254	0.0077	0.0051	1153	134.1142	33.7746	0.0278	0.0112	0.0045
1154	135.3053	33.7694	0.0298	0.0130	0.0000	1155	135.9706	33.6608	0.0275	0.0139	-0.0019
1156	136.0244	33.8204	0.0298	0.0094	-0.0001	1157	132.3398	34.3970	0.0321	0.0113	-0.0084

1158	136.7727	37.0007	0.1952	0.0120	0.0121	1159	141.0547	39.3620	1.7220	-1.0949	-0.0360
1160	137.7234	34.6723	0.0629	0.0211	0.0058	1161	137.4425	34.6804	0.0611	0.0206	0.0075
1162	139.5338	38.5112	1.0235	-0.2382	0.0233	1163	139.2762	36.6023	0.5192	0.0606	-0.0039
1164	132.2688	34.5754	0.0343	0.0112	-0.0070	G201	141.6853	45.4078	0.0051	-0.0111	-0.0048
G202	144.2858	44.0194	0.0048	0.0128	-0.0024	G203	144.3714	42.9756	0.0098	0.0212	-0.0057
G204	140.7245	41.7817	0.1050	-0.1523	0.0214	G206	139.8249	34.9188	0.0611	0.0041	-0.0121
G207	137.2246	36.7622	0.2059	0.0196	0.0170	G208	135.7732	33.4759	0.0235	0.0109	0.0025
G209	132.0662	34.8973	0.0360	0.0099	-0.0020	G210	129.8662	32.7351	0.0164	0.0046	-0.0010
G211	131.4093	31.5770	0.0107	0.0018	0.0022	G212	127.6652	26.2133	-0.0006	0.0007	0.0017
G213	142.1946	27.0939	0.0038	-0.0001	0.0030	GUAM	144.8700	13.5900	0.0016	-0.0016	0.0154
GUUG	144.8000	13.4300	-0.0057	-0.0010	0.0051	3001	139.5423	36.2952	0.4915	0.0652	-0.0283
3002	140.1743	36.2633	0.7310	0.0093	-0.1059	3003	139.8105	36.2037	0.5417	0.0518	-0.0465
3004	140.5445	36.1813	0.9223	-0.0692	-0.2055	3005	139.3452	36.1210	0.3726	0.0652	0.0003
3006	140.3432	36.0969	0.7146	0.0019	-0.1315	3007	139.6367	36.0872	0.4383	0.0631	-0.0290
3008	139.7999	36.0109	0.4509	0.0607	-0.0437	3009	140.6592	35.9555	0.7938	-0.0449	-0.2320
3010	140.4030	35.9704	0.6497	0.0112	-0.1270	3011	139.4643	35.9255	0.3343	0.0641	-0.0138
3012	139.9927	35.9403	0.4718	0.0535	-0.0607	3013	139.6519	35.9375	0.3759	0.0639	-0.0248
3014	140.1455	35.8736	0.4815	0.0431	-0.0908	3015	140.4070	35.8033	0.5027	0.0285	-0.0960
3016	139.8128	35.7802	0.3450	0.0626	-0.0412	3018	140.0247	35.7865	0.3921	0.0557	-0.0600
3019	139.4883	35.7104	0.2638	0.0642	-0.0208	3020	140.3151	35.7175	0.4095	0.0386	-0.0803
3021	140.6468	35.7773	0.5457	-0.0171	-0.1269	3022	140.8372	35.7264	0.5410	-0.0763	-0.1386
3023	139.9024	35.6755	0.3126	0.0601	-0.0436	3024	140.4483	35.6424	0.3747	0.0177	-0.0841
3025	140.1866	35.5441	0.2721	0.0397	-0.0533	3026	139.6734	35.5634	0.2317	0.0542	-0.0254
3027	140.3182	35.5301	0.2794	0.0266	-0.0569	3028	139.4678	35.5214	0.1962	0.0516	-0.0070
3029	139.3226	35.4826	0.1778	0.0482	-0.0025	3030	140.0513	35.4478	0.2138	0.0423	-0.0387
3031	139.0452	35.4154	0.1538	0.0490	0.0111	3032	139.6537	35.4365	0.1836	0.0488	-0.0164
3033	140.3374	35.4211	0.2176	0.0182	-0.0531	3034	139.4661	35.3267	0.1438	0.0411	-0.0032
3035	139.2627	35.3049	0.1346	0.0404	0.0014	3036	139.8255	35.3117	0.1481	0.0359	-0.0236
3037	140.1468	35.3331	0.1652	0.0287	-0.0356	3038	138.8817	35.3216	0.1364	0.0455	0.0084
3039	139.8436	35.1437	0.1043	0.0229	-0.0173	3041	140.2680	35.1659	0.1083	0.0113	-0.0307
3042	139.1104	35.1486	0.0983	0.0332	-0.0014	3043	138.9019	35.1100	0.0915	0.0365	0.0039
3044	140.0793	35.1119	0.0959	0.0132	-0.0249	3045	139.9543	35.2548	0.1326	0.0294	-0.0191
3046	138.9979	35.0148	0.0822	0.0324	0.0002	3047	139.8641	34.9541	0.0674	0.0062	-0.0158
3048	139.1312	34.9393	0.0722	0.0234	-0.0071	3049	138.9248	34.9161	0.0715	0.0264	-0.0038
3050	137.6723	34.8353	0.0686	0.0218	0.0123	3051	139.3814	34.7844	0.0615	0.0281	-0.0008
3052	138.0175	34.7859	0.0668	0.0238	0.0077	3053	138.9898	34.7514	0.0596	0.0244	-0.0048
3055	139.4332	34.6868	0.0476	0.0058	-0.0087	3057	139.2579	34.3718	0.0406	0.0115	0.0035
3058	139.1345	34.2005	0.0223	0.0007	-0.0000	3059	139.5038	34.1211	0.0181	-0.0044	-0.0108
3060	139.5471	34.0591	0.0174	-0.0033	-0.0098	3061	139.0137	34.9218	0.0707	0.0270	-0.0069
3062	139.1244	34.8785	0.0634	0.0205	-0.0126	3063	139.2681	35.7238	0.2452	0.0599	-0.0020
3064	138.9759	35.6233	0.1939	0.0523	0.0080	3065	139.1572	35.6103	0.1999	0.0542	0.0004
3066	139.2049	35.4285	0.1608	0.0505	-0.0032	3067	139.6648	35.2671	0.1300	0.0325	-0.0149
3068	139.0493	35.2455	0.1217	0.0410	0.0101	3069	138.4453	35.4436	0.1344	0.0410	0.0148
3070	138.8140	35.4966	0.1560	0.0464	0.0076	3071	138.5634	35.3621	0.1261	0.0391	0.0156
3072	138.7707	35.3055	0.1364	0.0407	0.0224	3073	138.4457	35.2895	0.1138	0.0411	0.0094

3074	138.2535	35.2010	0.1012	0.0318	0.0041	3075	138.6170	35.2032	0.1105	0.0416	0.0036
3076	138.7215	35.1736	0.1039	0.0501	0.0041	3077	138.5247	35.0674	0.0921	0.0359	0.0060
3078	138.3687	35.1035	0.0923	0.0318	0.0099	3079	138.1349	35.1039	0.0911	0.0313	0.0091
3081	138.3783	34.9905	0.0864	0.0298	0.0130	3084	137.6952	35.0793	0.0839	0.0268	0.0105
3085	138.7861	34.7761	0.0593	0.0234	-0.0041	3086	138.8384	34.6100	0.0491	0.0176	0.0033
3088	138.0749	34.9398	0.0777	0.0252	0.0107	3089	137.9321	34.8439	0.0697	0.0251	0.0064
3090	137.8179	34.9413	0.0745	0.0242	0.0060	3091	138.1369	34.7578	0.0660	0.0219	0.0043
3092	138.2256	34.7383	0.0630	0.0203	-0.0056	3093	138.0535	34.7153	0.0638	0.0217	0.0058
3094	138.1293	34.6429	0.0585	0.0189	0.0088	3095	137.9374	34.6704	0.0622	0.0192	0.0111
3096	137.9113	34.7554	0.0645	0.0228	0.0064	3097	137.7918	34.7928	0.0647	0.0222	0.0089
3098	137.8234	34.6719	0.0611	0.0199	0.0063	3099	137.5755	34.9377	0.0707	0.0229	0.0029
3102	137.4340	34.8648	0.0715	0.0238	0.0028	3103	137.5543	34.8087	0.0683	0.0227	0.0045
3104	137.5149	34.7181	0.0607	0.0186	-0.0036	5105	139.1710	35.0406	0.0836	0.0195	0.0021
5113	139.7972	33.1199	-0.0068	-0.0170	-0.0141	IRKJ	104.3162	52.2190	0.0047	-0.0025	0.0009
IRKM	104.3162	52.2190	0.0035	-0.0014	0.0058	IRKT	104.3160	52.2190	0.0094	-0.0018	-0.0029
0001	141.7504	45.4030	0.0057	-0.0084	0.0014	0002	143.2242	44.4337	0.0047	0.0021	-0.0035
0003	141.7563	44.3979	0.0127	-0.0151	0.0005	0004	144.6758	43.9157	0.0063	0.0154	-0.0054
0005	144.4490	43.5079	0.0052	0.0131	-0.0083	0007	142.4825	43.5897	0.0089	-0.0125	0.0003
0008	141.5104	43.8540	0.0160	-0.0231	0.0017	0009	145.1296	43.0701	0.0060	0.0199	-0.0075
0010	144.4319	42.9633	0.0108	0.0213	-0.0039	0011	143.4592	43.0286	0.0094	0.0075	-0.0008
0012	142.4020	42.9805	0.0135	-0.0220	0.0030	0013	141.0309	43.1779	0.0279	-0.0512	0.0055
0014	141.7307	42.9833	0.0200	-0.0449	0.0065	0015	143.3310	42.3216	0.0218	0.0059	-0.0075
0016	142.3646	42.3569	0.0277	-0.0394	0.0017	0017	139.8577	42.4507	0.0761	-0.0986	0.0106
0018	140.9424	42.3742	0.0551	-0.0946	0.0090	0019	143.1565	42.0059	0.0264	-0.0037	-0.0039
0020	139.5196	42.1535	0.1034	-0.1199	0.0040	0021	140.1073	42.0081	0.1074	-0.1363	0.0098
0022	140.7478	41.8261	0.1033	-0.1507	0.0184	0023	140.0406	41.4664	0.1614	-0.1829	0.0142
0024	141.2133	41.3008	0.1519	-0.2093	0.0229	0026	140.2730	40.7790	0.3032	-0.2903	0.0349
0027	141.7891	40.1334	0.7348	-0.7197	-0.0639	0028	141.9400	39.5724	2.0076	-1.4853	-0.3808
0029	141.2039	39.1106	2.5799	-1.3286	-0.1584	0030	139.7762	39.9679	0.5582	-0.3361	0.0332
0031	140.0482	39.3987	0.9853	-0.4961	0.0322	0032	139.8089	38.8946	1.0766	-0.3650	0.0135
0033	140.3187	38.7586	1.6457	-0.5568	-0.0520	0035	140.3661	38.3310	1.9676	-0.4267	-0.0730
0036	141.4412	38.4492	4.8938	-1.6092	-0.8284	0037	140.9542	38.3175	3.2537	-0.8230	-0.2871
0038	140.9081	37.8007	2.8463	-0.4254	-0.2876	0040	139.7915	37.6437	1.1083	-0.0713	-0.0222
0041	140.9025	37.0907	2.0216	-0.3692	-0.4765	0042	140.6118	36.5399	1.2259	-0.1451	-0.2805
0043	139.7264	36.4018	0.5868	0.0478	-0.0293	0044	138.9063	36.6970	0.4395	0.0551	0.0166
0045	138.8654	36.2590	0.3190	0.0578	0.0151	0046	137.8511	36.4998	0.2374	0.0367	0.0185
0047	137.9438	35.9236	0.1689	0.0397	0.0176	0048	138.5833	35.5903	0.1640	0.0476	0.0130
0049	139.5096	38.2307	1.0209	-0.1718	0.0114	0050	138.9889	37.8965	0.6917	-0.0710	0.0268
0051	138.5744	37.3977	0.4970	-0.0075	0.0332	0052	137.4872	36.9290	0.2462	0.0149	0.0139
0053	136.8892	37.3824	0.2258	0.0020	0.0158	0054	136.6499	36.6634	0.1649	0.0183	0.0154
0055	136.1730	36.2312	0.1162	0.0192	0.0061	0056	136.1058	35.6026	0.0874	0.0208	0.0147
0057	135.2334	35.5499	0.0703	0.0163	0.0096	0058	137.3479	36.1360	0.1541	0.0291	0.0167
0059	137.2484	35.8005	0.1241	0.0319	0.0108	0060	136.9000	35.5261	0.0978	0.0270	0.0100
0061	137.4676	35.3968	0.1017	0.0288	0.0098	0062	136.1582	35.0947	0.0681	0.0222	0.0084
0063	137.0413	35.1281	0.0800	0.0255	0.0017	0064	136.5023	34.7590	0.0571	0.0184	0.0099

0065	136.8511	34.4654	0.0484	0.0174	0.0094	0066	136.1984	34.0607	0.0352	0.0105	-0.0009
0067	135.5010	34.8380	0.0524	0.0142	0.0030	0068	135.8514	34.3923	0.0423	0.0140	0.0044
0069	135.2215	34.1577	0.0351	0.0118	0.0002	0070	135.7644	33.4834	0.0234	0.0069	-0.0017
0071	134.5504	34.7848	0.0447	0.0117	-0.0019	0074	133.0587	35.4339	0.0498	0.0157	-0.0088
0075	132.2090	35.0028	0.0395	0.0117	0.0006	0076	131.6104	34.6165	0.0316	0.0094	-0.0005
0077	133.5280	34.5488	0.0368	0.0111	0.0036	0078	132.5754	34.3404	0.0333	0.0117	-0.0028
0079	130.9136	33.9966	0.0257	0.0073	-0.0026	0080	134.0239	34.2860	0.0348	0.0123	0.0046
0081	134.6260	33.9269	0.0344	0.0145	0.0062	0082	134.1221	33.3159	0.0233	0.0074	0.0009
0083	133.5783	33.5291	0.0250	0.0113	0.0041	0084	133.2418	33.2729	0.0243	0.0108	0.0016
0085	132.9664	32.7557	0.0189	0.0082	0.0009	0086	132.2812	33.4690	0.0230	0.0080	-0.0005
0087	130.4768	33.7307	0.0223	0.0071	-0.0028	0088	131.6914	33.4615	0.0231	0.0078	-0.0068
0089	130.9678	33.3311	0.0235	0.0061	-0.0015	0090	131.8764	32.9246	0.0213	0.0076	-0.0045
0091	129.8503	33.4761	0.0198	0.0071	-0.0090	0093	130.6456	32.5464	0.0178	0.0075	-0.0067
0094	131.6323	32.4454	0.0143	0.0055	-0.0010	0095	131.4697	32.0218	0.0099	0.0061	-0.0063
0096	130.1901	32.0132	0.0114	0.0050	-0.0009	0097	130.4664	31.5038	0.0114	0.0069	-0.0056
0098	130.2995	31.2646	0.0102	0.0055	-0.0025	0099	131.0875	31.2585	0.0102	0.0058	-0.0046
0100	127.7689	26.1448	0.0026	-0.0022	0.0042	0101	142.1697	45.3358	0.0040	-0.0075	-0.0052
0102	141.0382	45.2760	0.0056	-0.0166	-0.0062	0103	142.5371	45.0024	0.0046	-0.0051	-0.0050
0104	141.7414	44.8925	0.0076	-0.0135	-0.0029	0105	142.2652	44.7285	0.0053	-0.0083	-0.0041
0106	141.3301	44.4270	0.0109	-0.0228	-0.0041	0107	142.6256	44.2946	0.0054	-0.0052	-0.0032
0108	144.0298	44.0639	0.0055	0.0101	-0.0063	0109	145.1861	44.0192	0.0016	0.0118	-0.0070
0110	142.1517	44.0068	0.0105	-0.0147	0.0010	0111	143.3337	44.0056	0.0052	0.0033	-0.0068
0112	143.9269	42.8945	0.0109	0.0165	-0.0043	0113	144.9870	43.5494	0.0076	0.0159	-0.0055
0114	143.7873	43.8489	0.0049	0.0090	-0.0025	0115	145.1314	43.6618	0.0068	0.0181	-0.0074
0116	144.7743	43.4087	0.0087	0.0184	-0.0030	0117	141.4312	43.4047	0.0174	-0.0354	-0.0012
0118	145.1150	43.3825	0.0044	0.0174	-0.0058	0119	145.8011	43.3669	0.0055	0.0187	-0.0084
0120	140.5971	43.2926	0.0320	-0.0536	0.0018	0121	143.5624	43.2895	0.0063	0.0094	-0.0020
0122	144.3250	43.2329	0.0088	0.0183	-0.0044	0123	143.2980	43.2320	0.0065	0.0023	-0.0018
0124	144.1265	43.1206	0.0090	0.0170	-0.0053	0125	144.8430	43.0576	0.0066	0.0192	-0.0066
0126	140.4992	43.0568	0.0384	-0.0631	0.0012	0127	140.5439	42.9853	0.0395	-0.0645	0.0008
0128	141.2903	42.9714	0.0278	-0.0526	0.0049	0129	140.8833	42.8579	0.0389	-0.0662	0.0016
0130	140.6035	42.8027	0.0461	-0.0725	0.0066	0131	140.2332	42.7864	0.0531	-0.0792	0.0046
0132	141.8640	42.7294	0.0263	-0.0499	-0.0003	0133	142.2958	42.7272	0.0186	-0.0313	0.0039
0134	143.1033	42.6993	0.0147	-0.0003	-0.0000	0135	141.0750	42.6679	0.0407	-0.0709	0.0069
0136	141.6023	42.6555	0.0313	-0.0619	0.0099	0137	140.8257	42.6463	0.0469	-0.0770	0.0118
0138	143.4612	42.5516	0.0153	0.0074	-0.0055	0139	141.3615	42.5498	0.0392	-0.0725	0.0036
0140	140.3542	42.4944	0.0644	-0.0933	0.0088	0141	142.0602	42.4813	0.0308	-0.0517	0.0065
0142	142.5675	42.2477	0.0249	-0.0285	-0.0023	0143	140.2505	42.2437	0.0801	-0.1150	0.0103
0144	142.9354	42.1309	0.0268	-0.0153	-0.0057	0145	140.0040	42.1308	0.0981	-0.1200	0.0114
0146	140.5689	42.0986	0.0859	-0.1258	0.0136	0147	140.8055	42.0430	0.0815	-0.1277	0.0094
0149	140.3159	41.5990	0.1365	-0.1625	0.0230	0150	140.8805	41.4553	0.1427	-0.1895	0.0219
0151	140.6359	41.0432	0.2265	-0.2509	0.0279	0152	141.3680	40.9682	0.2180	-0.2880	0.0179
0153	141.1978	40.6251	0.3534	-0.4211	0.0198	0154	139.9281	40.5776	0.3544	-0.2862	0.0295
0155	140.5781	40.5237	0.4191	-0.3875	0.0263	0156	141.5113	40.5154	0.4059	-0.4761	0.0050
0157	141.0765	40.2911	0.5641	-0.5758	0.0130	0158	141.7131	40.4052	0.4659	-0.5213	-0.0216

0159	141.2937	40.2911	0.5701	-0.6033	0.0073	0160	141.4619	40.0486	0.8336	-0.7811	-0.0149
0161	141.2251	39.9806	0.8788	-0.7879	0.0073	0162	141.9505	39.8694	1.2142	-1.0363	-0.2006
0163	141.1649	39.8512	1.0431	-0.8700	0.0061	0164	141.8038	39.8492	1.2236	-1.0338	-0.1455
0165	140.9645	39.7011	1.1695	-0.8824	0.0106	0166	141.1721	39.5966	1.4307	-1.0425	-0.0190
0167	141.9553	39.4582	2.3552	-1.6682	-0.5096	0169	141.5342	39.3381	2.3098	-1.4716	-0.2331
0170	141.7980	39.2535	3.0178	-1.8615	-0.5363	0171	141.7399	39.0238	3.9306	-2.0765	-0.7398
0172	141.5726	38.9029	3.9438	-1.8500	-0.6381	0173	140.9906	38.8153	2.6791	-1.0997	-0.1090
0174	140.8016	38.7489	2.3834	-0.9000	-0.0912	0175	141.4494	38.6827	4.3777	-1.7103	-0.6354
0176	141.1475	38.5395	3.6862	-1.2452	-0.3116	0177	140.8514	38.4118	2.8305	-0.7701	-0.1640
0178	140.6429	38.2057	2.4913	-0.4828	-0.1376	0179	140.8440	38.0297	2.8702	-0.5002	-0.2061
0180	140.4426	37.9899	2.0492	-0.2558	-0.1162	0181	140.5773	40.3250	0.5102	-0.4356	0.0298
0182	140.2637	40.2712	0.5060	-0.3933	0.0365	0183	140.7873	40.2154	0.5927	-0.5306	0.0199
0184	140.0487	40.2473	0.4900	-0.3602	0.0323	0185	140.4020	40.0069	0.6866	-0.4986	0.0261
0186	140.1324	39.9361	0.6618	-0.4312	0.0363	0187	140.5970	39.7492	0.9563	-0.6240	-0.0019
0188	140.2342	39.6583	0.8864	-0.5175	0.0297	0189	140.3866	39.5493	1.0290	-0.5891	0.0219
0190	140.5598	39.3270	1.3305	-0.7307	-0.0092	0191	139.9077	39.2061	0.9928	-0.4285	0.0370
0192	140.1620	39.1642	1.1963	-0.5414	0.0073	0193	140.6296	39.0519	1.7173	-0.8236	-0.1024
0194	139.5477	39.1856	0.7926	-0.3124	0.0394	0195	139.9574	38.7597	1.2620	-0.4010	-0.0018
0196	139.8318	38.5940	1.2023	-0.3201	-0.0008	0197	139.7422	38.1462	1.1879	-0.1821	-0.0171
0198	140.0935	37.9636	1.5269	-0.2012	-0.0623	0199	140.0776	38.1975	1.5081	-0.2610	-0.0431
0200	140.4665	37.6833	1.9385	-0.1817	-0.0749	0201	140.7551	37.5606	2.2834	-0.2816	-0.2223
0202	140.0727	37.5669	1.3410	-0.0617	-0.0771	0203	141.0066	37.5337	2.9515	-0.4715	-0.6031
0204	139.5286	37.4735	0.8913	-0.0399	-0.0086	0205	140.6621	37.3255	1.9124	-0.2230	-0.2473
0206	139.3643	37.3028	0.7648	-0.0072	-0.0011	0207	139.5038	37.2815	0.8213	-0.0067	-0.0103
0209	139.8714	37.2611	1.0605	-0.0246	-0.0524	0210	140.2599	37.1263	1.3225	-0.0674	-0.0870
0211	140.5616	37.0893	1.6180	-0.1822	-0.2328	0212	140.4133	36.8621	1.3031	-0.1213	-0.1755
0213	140.2934	36.6506	1.0322	-0.0541	-0.1379	0214	140.7539	36.8003	1.6107	-0.2348	-0.4333
0215	140.0779	36.3649	0.7475	0.0132	-0.0905	0216	140.4763	36.3444	0.9894	-0.0726	-0.2050
0217	140.0393	36.8542	0.9939	-0.0107	-0.0597	0218	139.6192	36.6660	0.6586	0.0480	-0.0258
0219	139.9235	36.5989	0.7550	0.0198	-0.0558	0220	139.2249	36.7697	0.5499	0.0458	-0.0020
0221	138.5527	36.5080	0.3325	0.0590	0.0135	0222	139.3304	36.4216	0.4763	0.0687	-0.0017
0223	139.0757	35.9869	0.2908	0.0636	0.0026	0224	139.7960	35.8960	0.3977	0.0629	-0.0369
0225	140.0481	35.6572	0.2565	0.0252	-0.0766	0226	140.3849	35.2432	0.1227	-0.0079	-0.0468
0227	139.9749	35.0028	0.0715	0.0061	-0.0202	0228	139.6306	35.6637	0.2636	0.0588	-0.0176
0229	139.1626	35.3362	0.1397	0.0441	0.0020	0230	139.1424	35.2686	0.1251	0.0372	-0.0006
0231	139.2533	38.4654	0.8244	-0.1818	0.0364	0232	138.5131	38.3193	0.5369	-0.0882	0.0414
0233	138.4717	38.0633	0.5262	-0.0603	0.0286	0234	139.3515	37.9294	0.9062	-0.0979	0.0201
0235	138.2731	37.8159	0.4612	-0.0329	0.0300	0236	139.4779	37.6859	0.9192	-0.0652	0.0027
0237	138.7805	37.6675	0.5933	-0.0380	0.0246	0238	139.0591	37.6623	0.7204	-0.0465	0.0282
0239	138.9980	37.4677	0.6559	-0.0166	0.0215	0240	138.7900	37.3113	0.5705	0.0037	0.0329
0241	138.3336	37.2311	0.4241	0.0003	0.0316	0242	138.9337	37.1660	0.5906	0.0164	0.0158
0243	138.1002	37.1608	0.3612	0.0061	0.0272	0244	138.6087	37.0791	0.6239	0.3746	0.2445
0245	137.8738	37.0452	0.3057	0.0170	0.0246	0246	138.8308	36.9935	0.4965	0.0426	0.0162
0247	138.1987	36.8654	0.3319	0.0236	0.0263	0248	136.9961	36.7406	0.1924	0.0196	0.0135
0249	137.1952	36.6343	0.1941	0.0228	0.0153	0250	137.4399	36.5787	0.2121	0.0249	0.0189

0251	136.9206	36.4019	0.1611	0.0241	0.0150	0252	136.9193	37.8505	0.2538	-0.0162	0.0220
0253	137.2701	37.4460	0.2694	0.0022	0.0177	0255	136.3889	36.3945	0.1346	0.0204	0.0099
0256	136.6339	36.1653	0.1290	0.0235	0.0092	0257	136.2789	36.1456	0.1163	0.0209	0.0131
0258	136.5049	35.9849	0.1119	0.0224	0.0074	0259	135.9898	35.9450	0.0994	0.0200	0.0115
0260	136.1974	35.7928	0.0970	0.0227	0.0094	0261	135.9076	35.5344	0.0778	0.0189	0.0105
0262	135.6089	35.4627	0.0722	0.0196	0.0012	0263	138.3164	35.8560	0.1837	0.0484	0.0201
0264	138.6951	35.7469	0.1964	0.0531	0.0137	0265	138.4362	36.8017	0.3719	0.0302	0.0002
0266	137.8723	36.7065	0.2685	0.0320	0.0210	0267	138.2475	36.6652	0.3103	0.0376	0.0200
0268	138.3225	36.3862	0.2719	0.0460	0.0199	0269	138.6378	36.3460	0.3136	0.0589	0.0107
0270	137.9028	36.3224	0.2211	0.0405	0.0201	0271	138.2165	36.2085	0.2358	0.0435	0.0119
0272	138.4610	36.1306	0.2495	0.0565	0.0213	0273	137.9830	36.1211	0.2044	0.0361	0.0233
0274	137.6963	35.7836	0.1379	0.0350	0.0154	0275	138.0383	35.5561	0.1307	0.0361	0.0123
0276	137.8152	35.5211	0.1200	0.0345	0.0078	0277	137.9253	35.3171	0.1064	0.0316	0.0116
0278	137.5877	35.2470	0.0952	0.0300	0.0056	0279	137.1472	36.3355	0.1866	0.0338	0.0055
0280	136.9528	36.0330	0.1293	0.0274	0.0151	0281	137.5349	35.9735	0.1484	0.0354	0.0127
0282	136.8632	35.8669	0.1140	0.0263	0.0080	0283	136.9753	35.7578	0.1141	0.0252	0.0107
0284	137.4248	35.6572	0.1179	0.0320	0.0078	0285	136.4888	35.6362	0.0934	0.0205	0.0082
0286	136.6114	35.6329	0.0973	0.0229	0.0116	0287	137.1741	35.6121	0.1087	0.0278	0.0140
0288	136.6873	35.4883	0.0898	0.0230	0.0054	0289	137.1247	35.4787	0.1002	0.0284	0.0104
0291	136.5497	35.3717	0.0822	0.0211	0.0060	0292	137.1102	35.3674	0.0929	0.0269	0.0081
0293	137.4056	35.2620	0.0913	0.0293	0.0105	0294	136.5934	35.2279	0.0770	0.0225	0.0054
0295	137.9804	35.0315	0.0825	0.0270	0.0067	0296	138.5157	34.9865	0.0833	0.0322	0.0035
0297	138.9223	34.8656	0.0672	0.0225	-0.0151	0298	136.9300	35.3348	0.0872	0.0250	0.0075
0299	136.8288	35.1901	0.0802	0.0220	0.0130	0300	137.2536	35.1388	0.0791	0.0252	0.0027
0301	137.3132	35.0395	0.0747	0.0231	-0.0039	0302	137.0598	34.9950	0.0749	0.0233	0.0062
0303	137.2999	34.9197	0.0728	0.0262	0.0015	0304	136.8676	34.8234	0.0644	0.0213	0.0026
0305	137.1190	34.7949	0.0655	0.0228	0.0028	0306	137.2778	34.6487	0.0592	0.0210	0.0033
0307	137.0681	34.6092	0.0544	0.0170	0.0003	0309	136.6365	34.9138	0.0602	0.0182	0.0053
0310	136.1835	34.7429	0.0529	0.0159	0.0025	0311	136.5507	34.5470	0.0498	0.0156	0.0052
0312	136.3343	34.4331	0.0455	0.0148	0.0067	0314	136.8206	34.2534	0.0441	0.0209	0.0009
0315	136.0859	33.8751	0.0312	0.0143	0.0021	0316	136.0109	33.7413	0.0282	0.0093	-0.0010
0317	136.1980	35.5573	0.0836	0.0192	0.0104	0318	136.0537	35.4663	0.0784	0.0189	0.0065
0319	135.9132	35.3513	0.0750	0.0192	0.0098	0320	136.0628	35.3190	0.0726	0.0174	0.0042
0321	136.2356	35.2694	0.0736	0.0188	0.0050	0322	135.8708	35.1370	0.0634	0.0168	0.0050
0323	136.1450	34.9864	0.0632	0.0176	0.0110	0324	135.9062	34.9396	0.0582	0.0177	0.0046
0326	136.0548	34.8693	0.0567	0.0186	0.0090	0327	135.1732	35.7524	0.0764	0.0188	0.0071
0328	134.9323	35.5557	0.0652	0.0162	0.0123	0329	135.1640	35.2923	0.0625	0.0163	0.0062
0331	135.3669	35.1638	0.0626	0.0154	0.0064	0332	135.5645	35.0776	0.0581	0.0158	0.0079
0333	135.6654	34.9886	0.0597	0.0168	0.0000	0334	135.8642	34.7470	0.0540	0.0227	-0.0007
0335	135.6855	34.7778	0.0508	0.0143	-0.0013	0336	135.5185	34.6779	0.0493	0.0187	-0.0007
0337	135.4813	34.5273	0.0453	0.0158	0.0055	0338	135.6273	34.4791	0.0432	0.0144	-0.0002
0339	135.5869	34.4248	0.0451	0.0138	0.0062	0340	135.3642	34.4065	0.0417	0.0166	0.0013
0341	134.5825	35.4367	0.0608	0.0161	0.0043	0342	134.8185	35.3149	0.0571	0.0150	0.0042
0343	135.1819	35.1053	0.0566	0.0164	0.0047	0344	134.5860	35.0945	0.0499	0.0149	0.0048
0345	134.9726	35.0908	0.0547	0.0163	0.0040	0346	134.4038	34.9976	0.0495	0.0150	0.0051

0347	134.7673	34.9847	0.0499	0.0152	0.0020	0348	135.3260	34.9768	0.0505	0.0169	0.0041
0349	135.1764	34.9448	0.0530	0.0164	0.0036	0350	134.5452	34.8973	0.0472	0.0138	0.0035
0351	135.2159	34.8122	0.0501	0.0137	0.0068	0352	134.9972	34.8049	0.0474	0.0164	0.0066
0353	135.3418	34.7909	0.0499	0.0161	0.0068	0354	134.8288	34.7870	0.0462	0.0130	-0.0001
0355	135.3804	34.7243	0.0477	0.0148	-0.0018	0356	135.1723	34.6870	0.0454	0.0191	0.0046
0357	134.5196	34.6699	0.0447	0.0132	0.0078	0358	134.9657	34.6697	0.0442	0.0132	0.0013
0359	135.0241	34.5771	0.0428	0.0138	0.0055	0360	134.8610	34.4933	0.0403	0.0156	0.0036
0361	134.8815	34.3498	0.0398	0.0143	-0.0025	0362	134.7352	34.3343	0.0396	0.0144	-0.0075
0363	134.7365	34.2237	0.0365	0.0115	0.0011	0364	136.0504	34.5670	0.0465	0.0151	-0.0013
0365	135.7310	34.5392	0.0461	0.0184	-0.0003	0366	135.7042	34.3883	0.0415	0.0146	0.0045
0367	135.9637	34.0382	0.0315	0.0149	0.0017	0368	135.3580	34.2561	0.0382	0.0165	0.0041
0369	135.0660	34.2715	0.0371	0.0160	0.0014	0370	135.5901	34.2218	0.0364	0.0174	0.0035
0371	135.3849	33.9617	0.0334	0.0106	-0.0008	0372	135.1801	33.9139	0.0304	0.0119	-0.0008
0373	135.7821	33.8152	0.0309	0.0089	-0.0066	0374	135.5084	33.7855	0.0308	0.0112	0.0027
0375	135.3962	33.7443	0.0291	0.0144	0.0050	0376	135.9207	33.5839	0.0277	0.0128	0.0090
0377	135.5992	33.5056	0.0240	0.0093	0.0020	0378	134.0467	35.4568	0.0547	0.0110	0.0042
0379	133.4391	35.3455	0.0464	0.0118	0.0088	0380	134.2374	35.2659	0.0519	0.0127	0.0033
0381	133.3085	35.1646	0.0448	0.0129	0.0002	0382	133.2399	36.2853	0.0626	0.0074	0.0097
0383	132.9844	36.0932	0.0544	0.0083	0.0073	0384	132.7432	35.3926	0.0435	0.0090	0.0025
0385	132.9954	35.1956	0.0455	0.0162	-0.0052	0386	132.5073	35.1860	0.0424	0.0142	-0.0057
0387	132.7205	35.0198	0.0415	0.0117	-0.0036	0388	131.9231	34.7673	0.0310	0.0077	0.0003
0389	133.7925	35.2635	0.0486	0.0133	0.0035	0390	134.3196	35.0996	0.0501	0.0134	0.0024
0391	134.2348	35.0209	0.0489	0.0138	0.0053	0392	133.7345	35.0030	0.0436	0.0111	0.0026
0393	133.9609	34.9825	0.0464	0.0135	0.0016	0394	133.5981	34.8097	0.0408	0.0097	-0.0035
0395	133.9290	34.7914	0.0436	0.0118	0.0062	0396	134.1658	34.6577	0.0414	0.0147	0.0015
0397	133.7967	34.4386	0.0348	0.0098	-0.0019	0398	133.1202	34.9435	0.0419	0.0129	-0.0024
0399	132.2773	34.7269	0.0360	0.0113	-0.0036	0400	132.5402	34.6788	0.0359	0.0113	-0.0049
0401	133.1075	34.6725	0.0385	0.0132	-0.0045	0402	132.8240	34.5713	0.0363	0.0152	-0.0090
0403	132.4635	34.5392	0.0302	0.0077	-0.0037	0405	133.0098	34.3787	0.0350	0.0125	-0.0086
0407	131.4165	34.4399	0.0304	0.0077	-0.0001	0408	130.9431	34.2946	0.0266	0.0077	-0.0031
0409	131.5628	34.2837	0.0257	0.0060	-0.0045	0410	131.9533	34.2591	0.0306	0.0090	-0.0044
0411	131.3461	34.1895	0.0259	0.0092	0.0012	0412	131.5308	34.0572	0.0263	0.0101	-0.0057
0413	131.2860	33.9777	0.0262	0.0066	-0.0047	0414	132.1044	33.9751	0.0292	0.0090	-0.0059
0415	134.3520	34.0970	0.0361	0.0124	0.0020	0416	134.5601	34.0599	0.0328	0.0142	-0.0023
0417	134.0492	34.0515	0.0341	0.0121	-0.0027	0418	134.2302	34.0384	0.0346	0.0121	0.0033
0419	133.6813	33.9367	0.0304	0.0115	0.0039	0420	134.3891	33.8789	0.0292	0.0086	0.0019
0421	134.0582	33.8775	0.0295	0.0104	-0.0013	0422	134.6678	33.8302	0.0300	0.0094	0.0006
0423	134.5330	33.7251	0.0287	0.0084	0.0054	0424	134.3720	33.6185	0.0265	0.0089	0.0038
0425	134.3142	34.4724	0.0381	0.0114	0.0059	0426	134.2420	34.2546	0.0353	0.0106	0.0013
0427	133.7151	34.2174	0.0324	0.0092	0.0001	0428	133.6475	34.0681	0.0310	0.0083	-0.0009
0429	133.9255	34.1642	0.0335	0.0094	0.0008	0430	132.9902	34.0779	0.0296	0.0140	-0.0074
0431	133.5382	33.9387	0.0296	0.0123	0.0011	0432	133.2013	33.9212	0.0294	0.0142	-0.0028
0433	132.9116	33.7965	0.0281	0.0122	-0.0056	0434	132.6840	33.7226	0.0279	0.0093	-0.0060
0435	132.9379	33.5692	0.0264	0.0089	-0.0030	0436	132.6934	33.4468	0.0268	0.0097	-0.0059
0437	132.5618	32.9639	0.0213	0.0105	-0.0053	0438	133.6558	33.7670	0.0266	0.0109	0.0009

0439	133.8050	33.6542	0.0273	0.0100	-0.0010	0440	134.1069	33.6038	0.0258	0.0096	0.0010
0441	134.2808	33.5278	0.0252	0.0092	-0.0008	0442	133.9036	33.5057	0.0252	0.0110	0.0009
0443	133.2809	33.4684	0.0238	0.0117	-0.0027	0444	134.0071	33.4278	0.0247	0.0095	0.0050
0445	133.4030	33.4077	0.0239	0.0072	0.0017	0447	132.7927	33.1716	0.0213	0.0093	-0.0014
0448	132.9992	32.9912	0.0205	0.0090	0.0009	0449	132.7037	32.8406	0.0204	0.0101	0.0041
0450	130.2508	33.5361	0.0193	0.0090	-0.0094	0451	130.5220	33.5004	0.0199	0.0088	-0.0075
0452	130.8288	33.4655	0.0220	0.0066	-0.0041	0453	130.5647	33.2059	0.0212	0.0067	-0.0071
0454	130.2687	33.2749	0.0194	0.0089	-0.0069	0455	130.0942	33.0985	0.0182	0.0057	-0.0061
0456	129.4821	34.6556	0.0239	0.0073	-0.0025	0457	129.3115	34.2682	0.0218	0.0072	-0.0039
0458	129.7347	33.7427	0.0206	0.0066	-0.0027	0459	129.5370	33.3622	0.0182	0.0057	-0.0061
0460	129.6907	33.0631	0.0161	0.0072	-0.0092	0461	130.2713	32.8707	0.0172	0.0065	-0.0094
0462	128.8431	32.6694	0.0136	0.0076	-0.0064	0463	130.1546	32.6369	0.0145	0.0058	-0.0063
0464	130.5477	32.9335	0.0188	0.0055	-0.0032	0465	130.7648	32.8421	0.0179	0.0072	-0.0086
0466	131.0993	32.7407	0.0186	0.0066	-0.0025	0467	129.9873	32.3262	0.0140	0.0056	-0.0014
0468	130.5068	32.2992	0.0159	0.0061	-0.0047	0469	130.8026	32.2387	0.0136	0.0065	0.0009
0470	131.5642	33.6712	0.0243	0.0068	-0.0054	0471	131.1689	33.4962	0.0234	0.0063	-0.0057
0472	131.3473	33.2540	0.0233	0.0082	-0.0085	0473	131.7981	33.2394	0.0224	0.0073	-0.0046
0474	131.2861	33.0090	0.0194	0.0085	-0.0065	0475	131.5878	32.9869	0.0202	0.0093	-0.0100
0476	131.7568	32.7040	0.0171	0.0071	-0.0044	0477	131.3276	32.6848	0.0194	0.0054	-0.0057
0478	131.1489	32.4566	0.0144	0.0088	0.0003	0479	131.1852	32.2459	0.0126	0.0062	-0.0056
0480	131.5159	32.1704	0.0135	0.0062	-0.0067	0481	131.0786	31.9650	0.0141	0.0089	-0.0082
0482	131.0215	31.7403	0.0123	0.0058	-0.0020	0483	131.3689	31.6765	0.0093	0.0050	0.0008
0484	131.2174	31.4694	0.0086	0.0067	-0.0071	0485	130.5978	32.0575	0.0143	0.0061	-0.0049
0486	130.7597	31.8555	0.0080	0.0004	0.0017	0487	129.7954	31.7687	0.0110	0.0047	-0.0030
0488	130.2782	31.7174	0.0096	0.0071	-0.0083	0489	130.8361	31.6174	0.0085	0.0054	-0.0002
0490	130.6404	31.2352	0.0094	0.0067	-0.0004	0491	130.7231	31.1062	0.0095	0.0047	-0.0049
0492	130.9642	30.5309	0.0072	0.0037	-0.0028	0493	130.6384	30.3817	0.0068	0.0019	-0.0024
0494	129.4890	28.3991	0.0000	0.0000	-0.0011	0495	128.4323	27.0322	0.0018	0.0015	-0.0024
0496	127.8985	26.6948	0.0034	0.0001	-0.0039	0497	131.2278	25.8312	-0.0043	0.0022	-0.0113
0498	125.3738	24.7531	0.0020	0.0023	-0.0050	0499	122.9428	24.4542	0.0026	-0.0036	0.0041
0500	123.7920	24.4263	0.0027	0.0045	0.0007	0501	141.1671	45.1377	0.0078	-0.0149	-0.0025
0502	142.9645	44.5820	0.0033	-0.0014	-0.0056	0503	143.6157	44.2197	0.0042	0.0058	-0.0041
0504	143.0768	44.1919	0.0046	0.0007	-0.0033	0505	144.2933	43.9888	0.0048	0.0129	-0.0034
0506	142.5777	43.9084	0.0094	-0.0105	-0.0014	0507	144.1152	43.8281	0.0053	0.0111	-0.0060
0508	142.4096	43.7385	0.0076	-0.0128	-0.0030	0509	141.8738	43.7408	0.0112	-0.0233	-0.0019
0510	142.9030	43.7714	0.0067	-0.0043	-0.0026	0511	143.5782	43.6705	0.0048	0.0083	-0.0017
0512	145.2590	43.2321	0.0054	0.0185	-0.0073	0513	144.0796	43.4388	0.0035	0.0156	0.0009
0514	142.3953	43.3363	0.0089	-0.0174	0.0022	0515	144.5977	43.3070	0.0046	0.0165	-0.0052
0516	141.8909	43.2484	0.0150	-0.0319	0.0017	0517	140.8606	43.2095	0.0296	-0.0512	0.0028
0518	142.8097	43.1655	0.0080	-0.0082	-0.0001	0519	145.5205	43.1952	0.0045	0.0182	-0.0094
0520	141.5401	43.0776	0.0227	-0.0467	0.0066	0521	143.1706	42.9389	0.0097	-0.0003	-0.0021
0522	141.5774	42.8844	0.0204	-0.0480	-0.0031	0523	141.4071	42.7732	0.0342	-0.0551	0.0034
0525	140.7676	42.5514	0.0526	-0.0845	0.0068	0526	140.8764	42.4739	0.0531	-0.0884	0.0063
0527	139.4462	42.0605	0.1114	-0.1248	0.0087	0528	140.6669	42.1231	0.0814	-0.1218	0.0138
0529	140.7154	41.9767	0.0895	-0.1356	0.0137	0530	140.0712	41.8030	0.1259	-0.1564	0.0169

0531	144.7191	42.9826	0.0105	0.0230	-0.0072	0532	143.3157	42.1256	0.0245	0.0041	-0.0111
0533	141.4476	41.4047	0.1257	-0.1783	0.0138	0534	140.4908	41.1851	0.2024	-0.2258	0.0228
0535	140.8220	41.1455	0.1970	-0.2406	0.0277	0537	141.1318	40.8624	0.2618	-0.3279	0.0196
0538	140.5892	40.7063	0.3297	-0.3356	0.0370	0539	141.3762	40.6764	0.3208	-0.3955	0.0151
0540	140.4785	40.6243	0.3642	-0.3420	0.0315	0541	140.8033	40.6436	0.3775	-0.4035	0.0101
0542	140.4516	40.9102	0.2641	-0.2717	0.0336	0543	141.0663	39.9531	0.8603	-0.7676	-0.0028
0544	140.7692	39.3513	1.4775	-0.8881	-0.0419	0546	141.5755	39.1431	3.1200	-1.7336	-0.3972
0547	141.6753	39.5961	1.7912	-1.3126	-0.1874	0548	140.8479	38.5462	2.6946	-0.8635	-0.1260
0549	141.2129	38.4251	4.0406	-1.2214	-0.4567	0550	141.5007	38.3012	5.3055	-1.6092	-1.1032
0551	139.8489	39.8911	0.6042	-0.3558	0.0436	0552	140.0447	39.8258	0.7061	-0.4283	0.0348
0553	140.7328	39.7027	1.0653	-0.7061	-0.0084	0554	140.5067	39.1991	1.4140	-0.7024	-0.0270
0555	139.9275	39.0160	1.1188	-0.4267	0.0189	0556	140.3652	38.4968	1.8725	-0.4881	-0.0646
0557	140.2711	38.1481	1.7586	-0.2953	-0.0659	0559	140.2057	37.6160	1.5175	-0.0600	-0.0934
0560	140.3729	37.6207	1.7494	-0.1451	-0.0754	0561	140.1359	37.4245	1.3438	-0.0415	-0.0655
0563	139.5862	37.0972	0.8167	0.0154	-0.0192	0564	139.4617	38.0562	0.9846	-0.1312	0.0073
0565	138.3699	38.0237	0.4999	-0.0528	0.0308	0566	138.7069	37.5358	0.5502	-0.0239	0.0320
0567	138.5164	37.3485	0.4755	-0.0055	0.0370	0568	139.0202	37.3199	0.6493	-0.0031	0.0161
0569	138.2426	37.0567	0.3744	0.0123	0.0316	0570	137.8939	36.9509	0.2919	0.0206	0.0270
0571	139.0739	37.7521	0.7234	-0.0525	0.0314	0572	137.3695	36.7370	0.2173	0.0218	0.0144
0573	137.0319	36.6496	0.1853	0.0211	0.0182	0574	137.1385	37.3070	0.2485	0.0039	0.0201
0575	136.7188	37.1567	0.2026	0.0081	0.0157	0576	136.9961	37.1232	0.2170	0.0109	0.0140
0577	136.7556	36.8175	0.1771	0.0140	0.0176	0578	136.6053	36.3701	0.1430	0.0190	0.0127
0579	136.1850	35.9689	0.1049	0.0204	0.0125	0580	136.0560	35.8368	0.0954	0.0207	0.0100
0581	140.4976	36.7430	1.2784	-0.1510	-0.2268	0582	139.9878	36.3007	0.6700	0.0345	-0.0602
0583	139.9315	36.1148	0.5405	0.0517	-0.0530	0584	140.2024	36.0313	0.5954	0.0330	-0.0914
0585	140.1648	36.9523	1.1443	-0.0354	-0.0790	0586	139.8057	36.9796	0.8853	0.0146	-0.0446
0587	139.8543	36.7764	0.8193	0.0194	-0.0319	0588	140.1577	36.6925	0.9707	-0.0236	-0.0915
0589	139.4906	36.6242	0.5955	0.0631	-0.0185	0590	140.1793	36.5422	0.8904	-0.0228	-0.0990
0591	138.5914	36.6163	0.3651	0.0599	0.0112	0592	139.0666	36.2347	0.3452	0.0613	0.0117
0593	138.9124	36.1428	0.3020	0.0601	-0.0015	0594	139.4340	34.7615	0.0544	0.0129	0.0006
0595	139.3586	34.7376	0.0526	0.0187	-0.0014	0596	139.2709	34.5196	0.0395	0.0101	-0.0035
0597	139.2109	34.3331	0.0228	-0.0014	0.0057	0598	139.1376	34.2399	0.0178	0.0045	-0.0026
0600	139.4788	34.0758	0.0149	-0.0077	-0.0101	0601	139.6129	33.8841	0.0076	-0.0105	-0.0053
0602	139.7646	32.4635	-0.0068	-0.0188	-0.0054	0603	142.1628	26.6352	0.0062	-0.0015	-0.0031
0606	138.6904	35.6495	0.1799	0.0487	0.0099	0607	139.0258	35.5119	0.1706	0.0491	0.0067
0608	137.9845	36.2390	0.2205	0.0365	0.0204	0609	137.8717	36.2284	0.2043	0.0443	0.0152
0610	138.4993	36.2847	0.2812	0.0595	0.0168	0611	137.6826	36.0847	0.1699	0.0423	0.0119
0612	138.2145	36.0262	0.2026	0.0458	0.0161	0613	138.5830	35.9741	0.2303	0.0563	0.0152
0614	137.5983	35.8800	0.1444	0.0349	0.0148	0615	137.9839	35.7263	0.1476	0.0381	0.0132
0616	137.6764	35.3437	0.1029	0.0302	0.0090	0617	136.9043	36.2615	0.1471	0.0254	0.0115
0618	137.3630	36.2856	0.1717	0.0268	0.0142	0619	137.2007	35.9116	0.1281	0.0294	0.0183
0620	138.7765	34.8550	0.0670	0.0235	0.0019	0621	138.9284	35.2044	0.1061	0.0407	0.0073
0622	138.0983	34.6799	0.0625	0.0196	0.0085	0623	138.1830	34.6778	0.0613	0.0191	0.0062
0624	138.0465	34.6664	0.0605	0.0193	0.0082	0625	138.1590	34.6345	0.0582	0.0193	0.0035
0626	138.9069	35.0472	0.0869	0.0355	0.0031	0627	140.0863	36.1036	0.5968	0.0371	-0.0819

0628	138.9393	34.6989	0.0535	0.0177	-0.0089	0629	137.0736	35.2391	0.0867	0.0271	0.0037
0630	136.9658	35.1684	0.0741	0.0253	0.0069	0631	136.8627	34.9844	0.0706	0.0236	0.0072
0632	136.8319	34.9044	0.0664	0.0218	0.0042	0633	136.6942	35.0509	0.0710	0.0212	0.0085
0634	136.3933	34.8549	0.0588	0.0157	0.0083	0635	136.3298	34.6488	0.0494	0.0185	0.0055
0636	136.6284	34.4314	0.0502	0.0178	0.0091	0637	136.3429	34.2082	0.0388	0.0111	0.0057
0638	136.2647	35.4204	0.0807	0.0193	0.0066	0639	136.0412	35.0857	0.0644	0.0180	0.0053
0640	135.0340	35.6851	0.0730	0.0157	0.0064	0641	135.4158	35.4822	0.0700	0.0171	0.0044
0642	135.5495	35.2759	0.0656	0.0158	0.0036	0643	135.7733	35.0531	0.0617	0.0200	0.0047
0644	135.7724	34.9526	0.0585	0.0169	0.0026	0645	134.6774	35.6212	0.0654	0.0154	0.0055
0646	134.7287	35.4613	0.0619	0.0174	0.0032	0647	135.0220	35.2379	0.0576	0.0154	0.0051
0648	134.7712	35.1627	0.0532	0.0145	0.0070	0649	134.9450	34.9362	0.0517	0.0175	0.0067
0650	135.5284	34.3118	0.0405	0.0171	0.0009	0652	135.1677	34.0254	0.0402	0.0096	-0.0225
0653	135.4962	33.5544	0.0253	0.0096	0.0018	0654	133.3397	35.4360	0.0498	0.0138	0.0019
0655	134.3253	35.3614	0.0567	0.0121	0.0009	0656	133.1379	35.5635	0.0531	0.0136	-0.0024
0657	132.4573	34.8927	0.0388	0.0091	-0.0028	0658	132.0136	34.5711	0.0357	0.0077	-0.0000
0659	131.8643	34.4397	0.0327	0.0059	-0.0021	0660	133.5640	35.1697	0.0451	0.0128	0.0026
0662	133.3963	34.9934	0.0444	0.0153	-0.0037	0663	132.8516	34.8116	0.0369	0.0120	-0.0081
0664	133.3376	34.7778	0.0413	0.0158	-0.0087	0665	132.1947	34.3703	0.0323	0.0104	-0.0003
0666	132.4556	34.2609	0.0302	0.0120	-0.0049	0667	132.8844	34.2101	0.0324	0.0120	-0.0027
0668	131.1524	34.7643	0.0309	0.0077	-0.0007	0669	131.1762	34.3421	0.0277	0.0072	-0.0075
0670	131.0657	34.1798	0.0275	0.0096	-0.0086	0672	132.3583	33.9099	0.0287	0.0093	-0.0075
0673	134.6050	34.1718	0.0344	0.0123	0.0014	0674	133.8750	34.0397	0.0320	0.0100	-0.0011
0675	134.3015	33.7895	0.0293	0.0100	0.0017	0676	133.9987	34.4455	0.0398	0.0080	-0.0044
0677	133.7807	34.3834	0.0349	0.0108	0.0034	0678	133.1891	34.2524	0.0324	0.0145	-0.0048
0679	132.7817	33.9595	0.0281	0.0119	-0.0061	0680	132.4873	33.6116	0.0256	0.0099	-0.0111
0681	132.5438	33.1776	0.0232	0.0068	-0.0144	0683	133.2285	33.3269	0.0237	0.0112	-0.0027
0684	133.1286	33.2154	0.0239	0.0089	0.0011	0685	130.7496	33.7455	0.0260	0.0056	-0.0071
0686	131.0165	33.6974	0.0249	0.0080	-0.0064	0687	130.8239	33.6405	0.0221	0.0073	-0.0098
0688	130.7012	33.3272	0.0210	0.0072	-0.0057	0689	129.9401	33.1960	0.0173	0.0090	-0.0093
0690	129.6900	33.2661	0.0170	0.0085	-0.0072	0691	129.1255	33.2558	0.0160	0.0045	0.0000
0692	129.0263	32.8856	0.0139	0.0077	0.0000	0693	130.1664	32.7957	0.0168	0.0065	-0.0015
0694	130.3360	32.7930	0.0162	0.0067	-0.0040	0695	130.2167	32.7123	0.0163	0.0070	-0.0047
0696	130.3523	32.7226	0.0158	0.0082	-0.0091	0697	130.2907	32.6607	0.0158	0.0074	-0.0039
0698	128.6194	32.6343	0.0130	0.0066	-0.0099	0699	131.0629	33.1220	0.0246	0.0111	-0.0109
0700	130.7486	33.0113	0.0204	0.0085	-0.0076	0701	130.9962	32.8707	0.0230	0.0079	-0.0016
0702	130.7949	32.5767	0.0183	0.0081	-0.0065	0703	131.0934	32.9507	0.0195	0.0059	-0.0047
0704	131.1322	32.8450	0.0225	0.0092	-0.0055	0705	131.3566	33.5371	0.0237	0.0073	-0.0071
0706	131.5884	33.3499	0.0215	0.0084	-0.0050	0707	131.1211	33.2703	0.0234	0.0079	-0.0045
0709	131.5795	33.2284	0.0208	0.0089	-0.0051	0710	130.9157	33.1906	0.0218	0.0059	-0.0036
0711	131.5307	32.5570	0.0159	0.0076	-0.0084	0712	131.3340	32.3844	0.0141	0.0063	-0.0010
0713	131.4860	32.0691	0.0121	0.0055	-0.0013	0714	130.8656	32.0477	0.0106	0.0033	-0.0049
0715	131.3063	31.8421	0.0121	0.0052	-0.0066	0716	131.3059	31.3991	0.0096	0.0043	-0.0029
0717	130.1797	32.1971	0.0146	0.0056	-0.0106	0718	130.4397	31.9088	0.0122	0.0069	-0.0046
0719	130.6519	31.6241	0.0135	0.0078	-0.0089	0720	130.7085	31.5918	0.0103	0.0093	-0.0101
0721	130.6374	31.5522	0.0113	0.0086	-0.0060	0722	130.6994	31.4962	0.0110	0.0073	-0.0048

0723	130.2750	30.7847	0.0091	0.0026	-0.0046	0724	131.0286	30.7533	0.0076	0.0022	-0.0004
0725	130.1982	30.4614	0.0074	0.0027	-0.0024	0726	130.9032	30.3987	0.0078	0.0012	-0.0025
0727	130.4244	30.3958	0.0075	0.0035	-0.0056	0728	130.5546	30.2364	0.0061	0.0027	-0.0011
0729	129.7057	29.6153	0.0046	0.0039	-0.0038	0730	129.6936	28.4872	0.0034	0.0022	-0.0072
0731	130.0290	28.3711	0.0053	-0.0008	-0.0102	0732	129.9217	28.2940	0.0039	0.0019	-0.0075
0733	129.3204	28.1376	0.0013	0.0038	-0.0036	0734	128.8945	27.8166	0.0018	0.0037	-0.0076
0735	128.6507	27.4012	0.0028	0.0023	-0.0044	0736	127.9451	26.9445	0.0019	0.0005	-0.0022
0737	128.2484	26.8593	0.0045	-0.0009	-0.0004	0738	128.1440	26.7083	0.0019	0.0013	-0.0016
0739	127.2316	26.5829	0.0018	0.0000	0.0007	0740	127.9724	26.4827	0.0032	0.0004	-0.0024
0741	127.8327	26.4469	0.0031	0.0011	-0.0031	0742	127.1436	26.3729	0.0024	0.0018	-0.0019
0743	126.7392	26.3478	0.0018	0.0031	0.0016	0744	127.3452	26.1788	-0.0019	0.0039	-0.0046
0745	127.8262	26.1686	0.0027	-0.0006	0.0006	0746	131.2907	25.9537	-0.0004	-0.0004	0.0017
0747	125.1710	24.8280	0.0034	0.0011	-0.0033	0748	124.6924	24.6416	0.0026	0.0006	-0.0049
0749	124.3013	24.5366	0.0038	0.0010	-0.0035	0750	124.1727	24.3389	0.0041	-0.0005	0.0016
0751	123.7959	24.0615	-0.0012	0.0053	-0.0056	0752	139.0567	36.5393	0.4430	0.0611	0.0119
0753	139.2693	36.0037	0.3230	0.0645	0.0005	0754	139.1822	35.8840	0.2736	0.0620	-0.0002
0755	139.3660	35.8008	0.2804	0.0608	-0.0020	0756	140.2492	35.2884	0.1355	0.0114	-0.0364
0758	139.3699	35.6164	0.2196	0.0539	-0.0077	0759	139.6138	35.1609	0.1059	0.0245	-0.0095
0760	135.7898	34.8820	0.0558	0.0174	0.0098	0761	135.6188	34.6211	0.0494	0.0158	0.0068
0762	134.6597	34.8641	0.0480	0.0149	0.0002	0763	135.7060	34.6983	0.0517	0.0165	0.0067
0764	135.8199	34.5740	0.0467	0.0139	-0.0066	0765	134.1758	34.8096	0.0442	0.0131	0.0047
0766	133.7570	34.5791	0.0370	0.0103	-0.0006	0767	133.2881	34.4504	0.0364	0.0134	-0.0015
0768	132.8202	34.3349	0.0333	0.0123	-0.0106	0769	132.2191	34.1912	0.0305	0.0123	-0.0113
0770	129.9548	33.3722	0.0191	0.0058	-0.0045	0771	130.4445	33.3465	0.0210	0.0076	-0.0055
0772	129.9897	32.9456	0.0178	0.0086	-0.0089	0773	130.4305	32.5817	0.0139	0.0044	-0.0022
0774	130.0852	32.5245	0.0147	0.0050	-0.0056	0775	130.3236	32.4263	0.0157	0.0071	-0.0040
0776	130.4695	31.6751	0.0115	0.0062	-0.0022	0777	130.1358	31.4159	0.0115	0.0056	-0.0042
0778	141.5982	45.2198	0.0048	-0.0123	-0.0088	0779	142.3518	45.1268	0.0037	-0.0076	-0.0076
0780	142.7179	44.7802	0.0047	-0.0049	-0.0010	0781	141.7939	44.6399	0.0071	-0.0137	-0.0063
0782	142.2645	44.3651	0.0063	-0.0104	-0.0024	0783	141.6646	44.1488	0.0104	-0.0213	-0.0030
0784	144.5064	43.7228	0.0061	0.0150	-0.0049	0785	141.3706	43.6243	0.0159	-0.0314	0.0028
0787	142.6431	43.4316	0.0065	-0.0107	0.0011	0788	143.9020	43.1017	0.0089	0.0147	-0.0025
0789	142.8701	43.0137	0.0097	-0.0084	0.0003	0790	142.0846	42.9338	0.0167	-0.0355	0.0032
0791	143.4950	42.8065	0.0104	0.0097	-0.0037	0792	141.0811	42.4205	0.0513	-0.0900	0.0105
0793	143.1520	42.4864	0.0179	-0.0013	-0.0044	0794	140.3712	41.9349	0.1059	-0.1436	0.0160
0795	141.4526	39.8490	1.1238	-0.9411	-0.0343	0796	140.9884	39.1270	2.0796	-1.1092	-0.0588
0797	140.6456	37.9844	2.4119	-0.3579	-0.1284	0798	140.8229	40.0450	0.7702	-0.6690	0.0028
0799	140.0946	38.4343	1.5012	-0.3465	-0.0386	0800	140.8416	37.0184	1.8220	-0.3407	-0.4802
0801	139.4022	37.0369	0.7059	0.0173	-0.0191	0802	138.9448	36.7781	0.4734	0.0528	0.0207
0803	140.1999	38.2890	1.6577	-0.3323	-0.0499	0804	139.5219	35.4193	0.1708	0.0459	-0.0112
0805	139.2260	37.8282	0.7846	-0.0700	0.0164	0806	138.8804	37.7770	0.6250	-0.0517	0.0214
0807	138.7795	37.4987	0.5713	-0.0176	0.0289	0809	138.4568	35.6737	0.1659	0.0447	0.0139
0810	138.9203	37.5897	0.6438	-0.0286	0.0324	0811	137.5288	35.5751	0.1145	0.0319	0.0094
0812	136.4703	35.3597	0.0818	0.0246	0.0103	0813	138.9739	35.1142	0.0950	0.0333	0.0098
0814	138.8765	34.7195	0.0586	0.0220	-0.0018	0815	138.6100	35.1172	0.0971	0.0395	0.0046

0817	138.2100	35.0670	0.0875	0.0297	0.0072	0818	138.0817	35.0449	0.0871	0.0304	0.0070
0819	137.9468	34.9021	0.0743	0.0233	0.0055	0820	138.1767	34.8494	0.0717	0.0222	0.0060
0821	137.6808	34.7520	0.0636	0.0216	0.0055	0822	136.7888	35.3008	0.0833	0.0243	0.0070
0823	134.5882	35.2833	0.0609	0.0138	0.0032	0824	136.0970	34.1800	0.0369	0.0110	-0.0003
0825	135.7352	33.9695	0.0328	0.0108	-0.0058	0826	135.7088	33.6372	0.0284	0.0101	-0.0019
0827	134.3934	34.2178	0.0344	0.0110	-0.0001	0828	132.0461	33.3680	0.0223	0.0077	-0.0044
0829	132.4753	33.3844	0.0237	0.0095	-0.0034	0830	133.3626	33.7043	0.0266	0.0133	-0.0034
0831	130.4650	33.0974	0.0193	0.0070	-0.0067	0832	129.7207	32.8396	0.0161	0.0060	-0.0015
0833	131.2068	33.1278	0.0223	0.0096	-0.0166	0834	130.3607	32.0984	0.0126	0.0082	-0.0073
0835	130.2390	31.9062	0.0123	0.0062	-0.0022	0836	130.4080	31.7960	0.0116	0.0094	-0.0098
0837	130.5996	31.8241	0.0129	0.0070	-0.0055	0838	138.7628	34.6903	0.0552	0.0242	-0.0057
0840	138.3312	34.8362	0.0715	0.0239	0.0032	0841	139.0699	34.9498	0.0748	0.0250	0.0060
0842	138.2499	34.9543	0.0764	0.0269	-0.0052	0843	134.0495	35.1749	0.0477	0.0118	0.0001
0844	140.8105	40.8344	0.2862	-0.3259	0.0299	0845	140.3244	37.3618	1.5199	-0.0893	-0.0900
0846	133.4618	33.8184	0.0269	0.0094	0.0001	0847	137.8688	35.1604	0.0890	0.0283	0.0101
0848	141.9552	45.5141	0.0059	-0.0082	0.0021	0849	141.8818	45.2301	0.0051	-0.0093	0.0003
0850	142.2923	44.9905	0.0042	-0.0063	-0.0066	0851	142.0218	44.9161	0.0017	-0.0101	-0.0081
0852	142.0387	44.7432	0.0092	-0.0116	0.0047	0853	142.5712	44.5465	0.0050	-0.0048	-0.0052
0854	142.9358	44.3323	0.0045	-0.0015	-0.0049	0855	141.8722	44.3177	0.0087	-0.0155	0.0044
0856	143.3646	44.2609	0.0042	0.0042	-0.0044	0857	142.4009	44.1655	0.0061	-0.0094	-0.0037
0858	142.6012	44.1144	0.0054	-0.0066	-0.0035	0859	144.9935	44.0650	0.0071	0.0158	-0.0082
0860	141.8607	44.0521	0.0103	-0.0194	-0.0023	0861	143.5341	43.9099	0.0050	0.0072	-0.0033
0862	142.2365	43.8893	0.0088	-0.0150	-0.0025	0863	143.1767	43.8787	0.0050	0.0027	-0.0035
0864	145.0569	43.7940	0.0066	0.0143	-0.0060	0865	142.1323	43.7257	0.0102	-0.0181	-0.0014
0866	143.3811	43.7103	0.0054	0.0062	-0.0032	0867	142.7944	43.6469	0.0084	-0.0077	-0.0018
0868	143.9917	43.6446	0.0060	0.0128	-0.0035	0869	145.2204	43.5560	0.0069	0.0162	-0.0052
0870	144.7190	43.5459	0.0073	0.0181	-0.0063	0871	142.1876	43.5216	0.0105	-0.0192	0.0001
0872	141.6168	43.5042	0.0160	-0.0296	0.0039	0873	143.7539	43.4736	0.0061	0.0114	-0.0013
0874	143.1870	43.3665	0.0056	0.0039	-0.0020	0875	140.3783	43.3207	0.0340	-0.0544	0.0009
0876	141.3460	43.2405	0.0222	-0.0443	0.0003	0877	141.6520	43.2209	0.0209	-0.0341	0.0040
0878	144.9707	43.2182	0.0093	0.0202	-0.0065	0879	143.0278	43.1713	0.0079	-0.0020	0.0006
0880	142.5670	43.1650	0.0076	-0.0138	0.0013	0881	144.4965	43.1494	0.0098	0.0198	-0.0046
0882	141.2033	43.1404	0.0268	-0.0507	0.0035	0883	143.5977	43.1239	0.0086	0.0094	-0.0031
0884	140.8111	43.0826	0.0339	-0.0573	0.0027	0885	142.5323	42.8906	0.0134	-0.0186	0.0020
0886	143.6555	42.8003	0.0126	0.0117	-0.0041	0887	142.9537	42.8033	0.0125	-0.0057	-0.0025
0888	140.0118	42.6853	0.0609	-0.0868	0.0033	0889	143.3128	42.6740	0.0153	0.0043	-0.0022
0890	142.3959	42.5543	0.0231	-0.0302	0.0043	0891	142.7679	42.2772	0.0262	-0.0178	0.0005
0892	140.9293	41.7406	0.1064	-0.1580	0.0165	0893	140.5350	41.7113	0.1239	-0.1627	0.0203
0894	141.0945	41.4662	0.1322	-0.1863	0.0186	0895	140.9838	41.1997	0.1800	-0.2329	0.0255
0896	141.3857	41.1609	0.1700	-0.2378	0.0194	0897	140.2935	41.1217	0.2158	-0.2367	0.0286
0898	140.0110	40.7306	0.3120	-0.2723	0.0330	0899	141.1060	40.5800	0.3856	-0.4442	0.0262
0901	141.3320	40.5088	0.4199	-0.4846	0.0089	0902	140.9416	40.4476	0.4592	-0.4809	0.0231
0903	141.4849	40.2710	0.5934	-0.6225	-0.0047	0904	141.0465	40.1067	0.6973	-0.6727	0.0064
0905	141.6622	39.9710	0.9864	-0.8689	-0.0647	0906	141.9702	39.7390	1.5236	-1.2223	-0.2852
0907	141.4261	39.6394	1.5365	-1.1370	-0.0659	0908	140.8363	39.5545	1.2661	-0.8564	-0.0076

0909	141.2930	39.4647	1.7666	-1.1881	-0.0721	0910	141.3117	39.2354	2.3352	-1.3517	-0.1494
0911	141.4008	39.0121	3.1426	-1.5586	-0.2993	0912	141.1485	38.9955	2.6297	-1.2570	-0.1594
0913	140.8332	38.9340	2.1803	-0.9692	-0.0932	0914	141.3179	38.7432	3.7299	-1.5148	-0.4062
0915	141.0043	38.6861	2.9547	-1.0943	-0.1736	0916	141.1607	38.6606	3.5137	-1.3093	-0.2924
0917	140.7277	38.5718	2.3985	-0.7498	-0.1228	0918	141.3044	38.5098	4.2548	-1.4122	-0.5516
0919	140.9437	38.1771	3.2529	-0.7277	-0.2260	0920	140.7277	37.8246	2.4848	-0.3412	-0.1818
0921	140.0276	40.3394	0.4447	-0.3353	0.0339	0922	140.4082	40.1833	0.5696	-0.4504	0.0360
0923	140.0055	40.0997	0.5543	-0.3811	0.0393	0924	140.5359	39.9214	0.7772	-0.5552	0.0093
0925	140.0539	39.5276	0.8980	-0.4787	0.0321	0926	140.5961	39.5081	1.1645	-0.6985	0.0040
0927	140.2789	39.2967	1.1578	-0.5769	0.0174	0928	140.7151	39.1462	1.6940	-0.8875	-0.0886
0929	140.4473	39.0544	1.4947	-0.6568	-0.0285	0930	140.1835	38.9381	1.3632	-0.5318	-0.0084
0931	140.4973	38.7522	1.8769	-0.6215	-0.0922	0932	139.6745	38.7012	1.0563	-0.3034	0.0198
0933	140.2205	38.6284	1.6045	-0.4526	-0.0451	0934	140.3939	38.1704	1.9891	-0.3660	-0.1186
0935	139.8794	37.9206	1.2698	-0.1463	-0.0256	0936	140.4468	37.8335	1.9569	-0.1942	-0.0764
0937	139.9727	37.6693	1.2967	-0.0910	-0.0753	0938	140.5717	37.5911	2.0218	-0.2019	-0.1306
0939	139.8355	37.4613	1.1087	-0.0485	-0.0249	0940	140.4640	37.4449	1.7159	-0.0806	-0.1776
0941	139.6863	37.3262	0.9635	-0.0131	-0.0229	0942	140.2127	37.2930	1.3642	-0.0514	-0.0800
0943	140.4510	37.2106	1.5731	-0.1388	-0.1379	0944	140.7160	37.1831	1.8473	-0.2644	-0.3066
0945	140.3763	37.0236	1.3705	-0.1063	-0.1358	0946	140.6902	36.9326	1.6330	-0.2178	-0.3430
0947	140.3857	36.4758	0.9983	-0.0650	-0.1716	0948	140.0354	37.1247	1.1079	-0.0136	-0.0579
0949	139.5053	36.8722	0.7310	0.0491	-0.0297	0950	139.7528	36.5376	0.6577	0.0416	-0.0341
0951	139.9025	36.4566	0.6928	0.0276	-0.0517	0952	139.0609	36.8374	0.5196	0.0454	0.0086
0954	138.8479	36.5914	0.4019	0.0558	0.0176	0955	139.0167	36.3953	0.3864	0.0627	0.0045
0956	139.2546	36.2677	0.4061	0.0703	0.0086	0957	138.7030	36.2003	0.2859	0.0595	0.0191
0958	138.9261	35.9299	0.2569	0.0628	-0.0049	0959	139.9685	35.1438	0.1009	0.0179	-0.0251
0960	139.3661	35.3915	0.1570	0.0435	-0.0060	0961	139.1115	37.5403	0.7289	-0.0271	0.0208
0962	138.6346	37.2121	0.4896	0.0140	0.0244	0963	139.2471	37.1576	0.6820	0.0020	-0.0055
0964	138.4574	37.1071	0.4713	-0.0225	0.0327	0965	140.2965	36.7790	1.1237	-0.0680	-0.1311
0966	137.0264	36.9195	0.2047	0.0157	0.0198	0967	137.5513	36.8643	0.2527	0.0169	0.0154
0968	137.1545	36.7579	0.2017	0.0215	0.0171	0969	136.8064	36.5921	0.1646	0.0187	0.0034
0970	137.2392	36.4728	0.1805	0.0273	0.0234	0971	137.0339	37.4323	0.2451	0.0000	0.0160
0972	136.9088	37.2264	0.2192	0.0085	0.0121	0973	136.5407	36.5373	0.1511	0.0173	0.0074
0974	136.3616	36.2296	0.1331	0.0229	0.0064	0975	136.0490	36.1097	0.1068	0.0203	0.0113
0976	136.6577	35.9014	0.1143	0.0265	0.0136	0977	136.3396	35.8882	0.1023	0.0214	0.0090
0978	135.7556	35.4866	0.0770	0.0191	0.0091	0979	138.4442	35.9049	0.2022	0.0518	0.0184
0980	138.9500	35.7539	0.2177	0.0571	0.0100	0981	138.6069	35.4677	0.1478	0.0371	0.0062
0982	138.6243	36.8567	0.3904	0.0692	0.0149	0983	138.0967	36.7066	0.2930	0.0345	0.0206
0984	138.1209	36.5236	0.2725	0.0405	0.0224	0985	138.3660	36.2610	0.2570	0.0521	0.0187
0986	137.7854	35.9446	0.1600	0.0379	0.0179	0987	138.0957	35.8784	0.1704	0.0414	0.0166
0988	137.4509	35.8156	0.1318	0.0333	0.0092	0989	137.6202	35.6612	0.1253	0.0346	0.0122
0990	137.0805	36.1403	0.1428	0.0278	0.0099	0991	136.7846	35.7235	0.1054	0.0275	0.0099
0992	137.3091	35.5231	0.1056	0.0285	0.0089	0993	136.5453	35.4801	0.0888	0.0244	0.0058
0994	137.2523	35.3006	0.0939	0.0285	0.0070	0995	137.5753	35.1000	0.0852	0.0281	0.0064
0996	137.1524	34.9173	0.0708	0.0232	0.0041	0997	137.3388	34.7859	0.0660	0.0229	0.0024
0998	136.9385	34.7401	0.0625	0.0200	0.0097	0999	136.4745	34.4203	0.0469	0.0163	0.0076

KGNI	139.4880	35.7100	0.2722	0.0596	-0.0013	KHAJ	135.0460	48.5210	0.0084	-0.0112	0.0001
KNYA	130.8786	31.4253	0.0115	0.0061	-0.0113	KSMV	140.6580	35.9550	0.7552	-0.0682	-0.2698
KUNM	102.7970	25.0300	0.0001	0.0056	-0.0132	MAGJ	150.8104	59.5776	0.0012	-0.0008	-0.0171
MCIL	153.9800	24.2900	-0.0074	0.0088	-0.0050	MIZU	141.1330	39.1350	2.3313	-1.2477	-0.0861
MTKA	139.5600	35.6800	0.2545	0.0580	-0.0118	NIMT	100.7137	14.0430	-0.0010	-0.0009	-0.0056
OKN1	127.7689	26.1448	0.0003	-0.0042	0.0062	PETS	158.6500	53.0200	0.0054	-0.0007	0.0020
PIMO	121.0800	14.6400	-0.0030	0.0042	-0.0013	2004	130.8786	31.4253	0.0105	0.0043	-0.0067
2005	141.8448	43.5286	0.0146	-0.0281	0.0013	2007	142.1950	27.0675	0.0048	-0.0007	0.0002
2106	139.0820	35.0069	0.0805	0.0331	0.0070	2107	139.1017	34.9719	0.0712	0.0345	-0.0023
2110	140.0872	36.1061	0.5996	0.0342	-0.0846	SHAO	121.2000	31.1000	0.0054	0.0002	-0.0012
SMST	135.9370	33.5779	0.0269	0.0154	-0.0008	STK2	141.8450	43.5290	0.0136	-0.0278	0.0029
SUWN	127.0540	37.2760	0.0260	0.0007	-0.0033	TCMS	120.9900	24.8000	0.0003	-0.0006	-0.0032
TNML	120.9900	24.8000	0.0000	-0.0001	-0.0059	TSK2	140.0900	36.1100	0.5933	0.0393	-0.0809
TSKB	140.0870	36.1060	0.5932	0.0376	-0.0808	TWTF	121.1600	24.9500	-0.0011	0.0010	0.0029
ULAB	107.0500	47.8700	0.0038	-0.0015	-0.0012	USUD	138.3620	36.1330	0.2347	0.0508	0.0226
WUHN	114.3570	30.5320	0.0073	-0.0018	0.0033	YSSK	142.7200	47.0300	0.0022	-0.0024	-0.0054
G101	136.5038	35.1048	0.0712	0.0218	0.0073	G102	138.1858	35.3221	0.1129	0.0340	0.0141
G103	137.4231	34.9675	0.0757	0.0256	0.0025	G104	136.9818	34.5439	0.0520	0.0228	0.0033
G105	136.8020	34.3736	0.0444	0.0175	0.0063	G106	136.3885	34.2979	0.0418	0.0152	0.0099
G107	136.1400	33.9329	0.0331	0.0153	0.0064	G108	135.7435	34.1558	0.0346	0.0121	-0.0007
G109	135.2903	34.0909	0.0338	0.0145	0.0057	G110	135.3991	33.8545	0.0291	0.0127	0.0021
G111	135.8711	33.7991	0.0289	0.0147	0.0098	G112	135.4060	33.6473	0.0272	0.0124	0.0049
G113	135.8341	33.5201	0.0219	0.0108	0.0042	G114	134.5100	33.9328	0.0307	0.0096	0.0079
G115	133.7970	33.8388	0.0270	0.0111	0.0019	G116	134.4846	33.8220	0.0285	0.0113	0.0090
G117	132.5647	33.5104	0.0302	0.0103	-0.0138	G118	132.3604	33.2022	0.0241	0.0083	-0.0029
G119	133.4317	33.5457	0.0247	0.0109	0.0021	G120	133.6998	33.5425	0.0243	0.0113	0.0116
G121	134.0562	33.3674	0.0233	0.0097	0.0132	G123	132.9740	33.3121	0.0271	0.0090	-0.0101
G124	132.8221	33.0601	0.0218	0.0099	-0.0049	CHOS	141.6699	35.5030	1.1224	-0.1908	-0.1119
FUKU	142.0831	37.1660	4.4169	-1.6650	0.8600	KAMN	143.3623	38.8879	13.8338	-5.8282	1.6100
KAMS	143.2635	38.6364	21.0896	-8.9423	1.4900	MYGI	142.9167	38.0829	22.1045	-10.3906	3.1400
MYGW	142.4333	38.1506	14.4144	-5.0258	-0.7800						

Table D.1: Estimated coseismic displacements

APPENDIX E

REGIONS AND PREFECTURES OF JAPAN

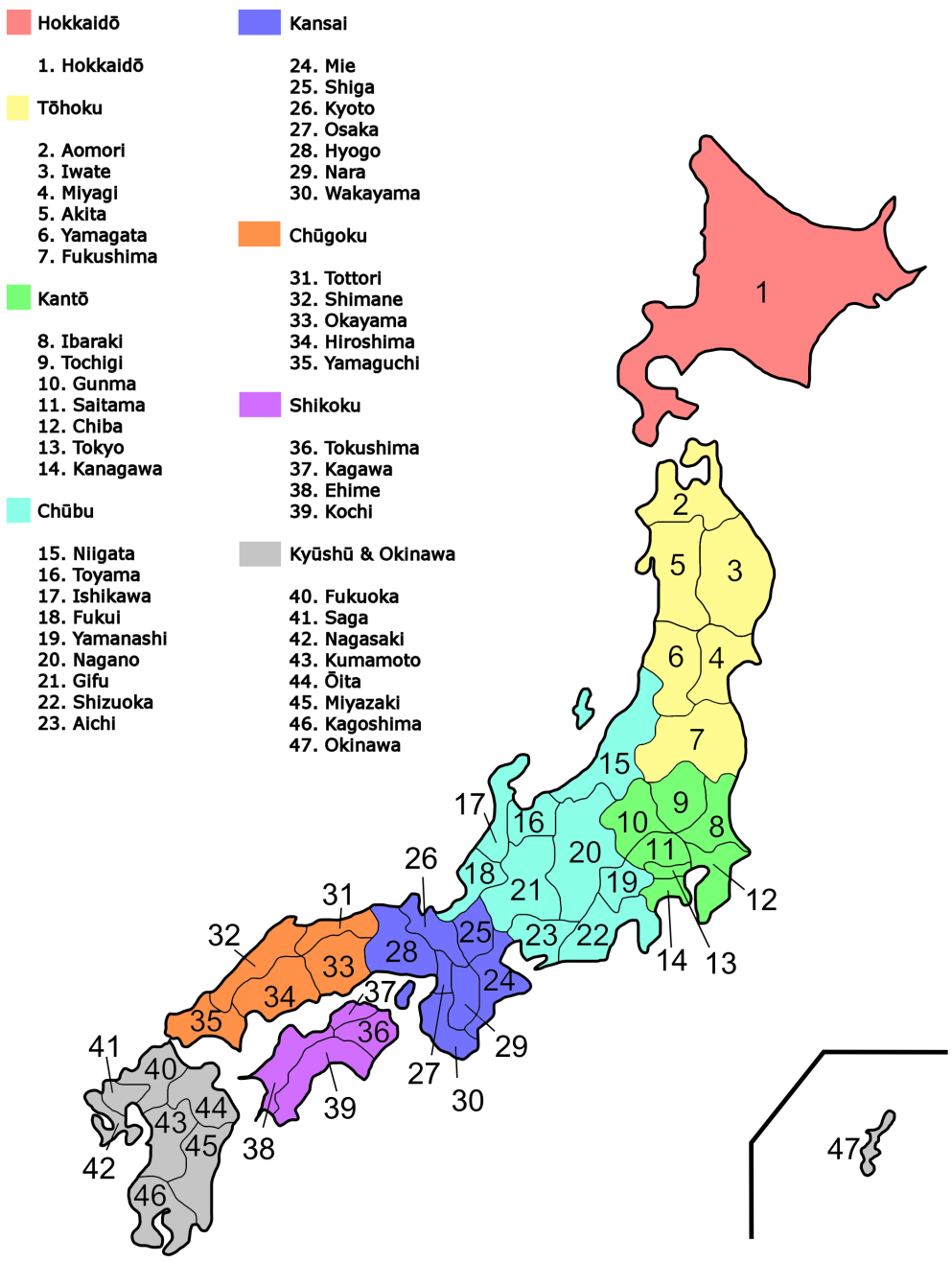

BIBLIOGRAPHY

Ammon, C. J., T. Lay, H. Kanamori, and M. Cleveland, A rupture model of the 2011 off the pacific coast of tohoku earthquake, *Earth, Planets and Space*, *63*, 693–696, 2011.

Andersen, M., J. Dahl, and L. Vandenberghe, Python software for convex optimization (cvxopt), 2014.

Apel, E. V., R. Bürgmann, G. Steblov, N. Vasilenko, R. King, and A. Prytkov, Independent active microplate tectonics of northeast asia from gps velocities and block modeling, *Geophysical Research Letters*, *33*, L11,303, 2006.

Aster, R., B. Borchers, and C. Thurber, *Parameter estimation and inverse problems*, 2nd ed., 2013.

Baek, J., Y.-H. Shin, S.-H. Na, N. V. Shestakov, P.-H. Park, and S. Cho, Coseismic and postseismic crustal deformations of the korean peninsula caused by the 2011 mw 9.0 tohoku earthquake, japan, from global positioning system data, *Terra Nova*, *24*, 295–300, 2012.

Bird, P., An updated digital model of plate boundaries, *Geochemistry, Geophysics, Geosystems*, *4*, n/a–n/a, 2003.

Constable, S. C., R. L. Parker, and C. G. Constable, Occams inversion: A practical algorithm for generating smooth models from electromagnetic sounding data, *GEOPHYSICS*, *52*, 289–300, 1987.

Diao, F., X. Xiong, R. Wang, Y. Zheng, T. R. Walter, H. Weng, and J. Li, Overlapping post-seismic deformation processes: afterslip and viscoelastic relaxation following the 2011 mw 9.0 tohoku (japan) earthquake, *Geophysical Journal International*, *196*, 218–229, 2013.

Dziewonski, A. M., and D. L. Anderson, Preliminary reference earth model, *Physics of the Earth and Planetary Interiors*, *25*, 297–356, 1981.

Ergintav, S., S. McClusky, E. Hearn, R. Reilinger, R. Cakmak, T. Herring, H. Ozener, O. Lenk, and E. Tari, Seven years of postseismic deformation following the 1999, m = 7.4 and m = 7.2, izmit-düzce, turkey earthquake sequence, *Journal of Geophysical Research*, *114*, B07,403, 2009.

Evans, E. L., and B. J. Meade, Geodetic imaging of coseismic slip and postseismic afterslip: Sparsity promoting methods applied to the great tohoku earthquake, *Geophysical Research Letters*, *39*, n/a–n/a, 2012.

Frasso, G., Smoothing parameter selection using the l-curve, Master's thesis, Leiden University, 2012.

Fujii, Y., K. Satake, S. Sakai, M. Shinohara, and T. Kanazawa, Tsunami source of the 2011 off the pacific coast of tohoku earthquake, *Earth, Planets and Space*, *63*, 815–820, 2011.

Han, S.-c., J. Sauber, and F. Pollitz, Broadscale postseismic gravity change following the 2011 tohoku-oki earthquake and implication for deformation by viscoelastic relaxation and afterslip, pp. 1–9, 2014.

Hayes, G. P., D. J. Wald, and R. L. Johnson, Slab1.0: A three-dimensional model of global subduction zone geometries, *Journal of Geophysical Research*, *117*, B01,302, 2012.

Hearn, E. H., S. McClusky, S. Ergintav, and R. E. Reilinger, Izmit earthquake postseismic deformation and dynamics of the north anatolian fault zone, *Journal of Geophysical Research: Solid Earth*, *114*, n/a—-n/a, 2009.

Iinuma, T., et al., Coseismic slip distribution of the 2011 off the pacific coast of tohoku earthquake (m9.0) refined by means of seafloor geodetic data, *Journal of Geophysical Research: Solid Earth*, *117*, n/a—-n/a, 2012.

Ito, T., K. Ozawa, T. Watanabe, and T. Sagiya, Slip distribution of the 2011 off the pacific coast of tohoku earthquake inferred from geodetic data, *Earth, Planets and Space*, *63*, 627–630, 2011.

Kreemer, C., G. Blewitt, and E. C. Klein, A geodetic plate motion and global strain rate model, *Geochemistry, Geophysics, Geosystems*, *15*, 3849–3889, 2014.

Lubis, a. M., a. Hashima, and T. Sato, Analysis of afterslip distribution following the 2007 september 12 southern sumatra earthquake using poroelastic and viscoelastic media, *Geophysical Journal International*, *192*, 18–37, 2012.

Maeda, T., T. Furumura, S. Sakai, and M. Shinohara, Significant tsunami observed at ocean-bottom pressure gauges during the 2011 off the pacific coast of tohoku earthquake, *Earth, Planets and Space*, *63*, 803–808, 2011.

Marone, C. J., C. H. Scholtz, and R. Bilham, On the mechanics of earthquake afterslip, *Journal of Geophysical Research*, *96*, 8441, 1991.

Matsu'ura, M., A. Noda, and Y. Fukahata, Geodetic data inversion based on bayesian formulation with direct and indirect prior information, *Geophysical Journal International*, *171*, 1342–1351, 2007.

Minoura, K., F. Imamura, D. Sugawara, Y. Kono, and T. Iwashita, The 869 jogan tsunami deposit and recurrence interval of large-scale tsunami on the pacific coast of northeast japan, *Journal of Natural Disaster Science*, *23*, 83–88, 2001.

Minson, S. E., A bayesian approach to earthquake source studies, Ph.D. thesis, California Institute of Technology, 2010.

Minson, S. E., M. Simons, J. L. Beck, F. Ortega, J. Jiang, S. E. Owen, A. W. Moore, A. Inbal, and A. Sladen, Bayesian inversion for finite fault earthquake source models - ii: the 2011 great tohoku-oki, japan earthquake, *Geophysical Journal International*, *198*, 922–940, 2014.

Nishimura, T., M. Sato, and T. Sagiya, Global positioning system (gps) and gps-acoustic observations: Insight into slip along the subduction zones around japan, *Annual Review of Earth and Planetary Sciences*, *42*, 653–674, 2014.

Nur, A., and G. Mavko, Postseismic viscoelastic rebound., *Science (New York, N.Y.)*, *183*, 204–6, 1974.

Ohzono, M., Y. Ohta, T. Iinuma, S. Miura, and J. Muto, Geodetic evidence of viscoelastic relaxation after the 2008 iwate-miyagi nairiku earthquake, *Earth, planets and space*, *64*, 759–764, 2012.

Ozawa, S., T. Nishimura, H. Suito, and T. Kobayashi, Coseismic and postseismic slip of the 2011 magnitude-9 tohoku-oki earthquake, *Nature*, *475*, 373–376, 2011.

Ozawa, S., T. Nishimura, H. Munekane, H. Suito, T. Kobayashi, M. Tobita, and T. Imakiire, Preceding, coseismic, and postseismic slips of the 2011 tohoku earthquake, japan, *Journal of Geophysical Research*, *117*, B07,404, 2012.

Ozawa, S., H. Yarai, T. Imakiire, and M. Tobita, Spatial and temporal evolution of the long-term slow slip in the bungo channel, japan, *Earth Planets Space*, *65*, 67–73, 2013.

Peltzer, G., P. Rosen, F. Rogez, and K. Hudnut, Postseismic rebound in fault step-overs caused by pore fluid flow, *SCIENCE-NEW YORK THEN WASHINGTON-*, pp. 1202–1203, 1996.

Peltzer, G., P. Rosen, F. Rogez, and K. Hudnut, Poroelastic rebound along the landers 1992 earthquake surface rupture, *Journal of Geophysical Research*, *103*, 30,131, 1998.

Perfettini, H., Postseismic relaxation driven by brittle creep: A possible mechanism to reconcile geodetic measurements and the decay rate of aftershocks, application to the chi-chi earthquake, taiwan, *Journal of Geophysical Research*, *109*, B02,304, 2004.

Perfettini, H., Geodetic displacements and aftershocks following the 2001 m w = 8.4 peru earthquake: Implications for the mechanics of the earthquake cycle along subduction zones, *Journal of Geophysical Research*, *110*, B09,404, 2005.

Pollitz, F. F., Postseismic relaxation theory on the spherical earth, *Bulletin of the Seismological Society of America*, *82*, 422–453, 1992.

Pollitz, F. F., Coseismic deformation from earthquake faulting on a layered spherical earth, *Geophysical Journal International*, 1996.

Pollitz, F. F., Gravitational viscoelastic postseismic relaxation on a layered spherical earth, *Journal of Geophysical Research: Solid Earth (1978 . . . , 102*, 1997.

Pollitz, F. F., R. Biirgmann, and P. Segall, Joint estimation of afterslip rate and postseismic relaxation following the 1989 loma prieta earthquake, *103*, 1998.

Pollitz, F. F., R. Bürgmann, and P. Banerjee, Post-seismic relaxation following the great 2004 sumatra-andaman earthquake on a compressible self-gravitating earth, *Geophysical Journal International*, *167*, 397–420, 2006.

Pollitz, F. F., R. Bürgmann, and P. Banerjee, Geodetic slip model of the 2011 m9.0 tohoku earthquake, *Geophysical Research Letters*, *38*, n/a–n/a, 2011.

Sagiya, T., A decade of geonet : 1994 2003 the continuous gps observation in japan and its impact on earthquake studies , *2*, 1994–2003, 2004.

Sato, M., T. Ishikawa, N. Ujihara, S. Yoshida, M. Fujita, M. Mochizuki, and A. Asada, Displacement above the hypocenter of the 2011 tohoku-oki earthquake, *Science*, *332*, 1395, 2011.

Sella, G. F., T. H. Dixon, and A. Mao, Revel: A model for recent plate velocities from space geodesy, *Journal of Geophysical Research*, *107*, 2081, 2002.

Shao, G., X. Li, C. Ji, and T. Maeda, Focal mechanism and slip history of the 2011 m w 9.1 off the pacific coast of tohoku earthquake, constrained with teleseismic body and surface waves, *Earth, Planets and Space*, *63*, 559–564, 2011.

Shestakov, N. V., et al., Analysis of the far-field crustal displacements caused by the 2011 great tohoku earthquake inferred from continuous gps observations, *Tectonophysics*, *524525*, 76–86, 2012.

Silverii, F., D. Cheloni, N. D'Agostino, G. Selvaggi, and E. Boschi, Post-seismic slip of the 2011 tohoku-oki earthquake from gps observations: implications for depth-dependent properties of subduction megathrusts, *Geophysical Journal International*, pp. ggu149–, 2014.

Simons, M., et al., The 2011 magnitude 9.0 tohoku-oki earthquake: mosaicking the megathrust from seconds to centuries., *Science (New York, N.Y.)*, *332*, 1421–5, 2011.

Suito, H., and K. Hirahara, Simulation of postseismic deformations caused by the 1896 riku-u earthquake, northeast japan: Re-evaluation of the viscosity in the upper mantle, *Geophysical Research Letters*, *26*, 2561–2564, 1999.

Sun, T., et al., Prevalence of viscoelastic relaxation after the 2011 tohoku-oki earthquake, *Nature*, *514*, 84–87, 2014.

Tajima, F., J. Mori, and B. L. Kennett, A review of the 2011 tohoku-oki earthquake (mw 9.0): Large-scale rupture across heterogeneous plate coupling, *Tectonophysics*, *586*, 15–34, 2013.

Wang, L., C. K. Shum, F. J. Simons, B. Tapley, and C. Dai, Coseismic and postseismic deformation of the 2011 tohoku-oki earthquake constrained by grace gravimetry, *Geophysical Research Letters*, *39*, n/a–n/a, 2012.

Wang, M., Q. Li, F. Wang, R. Zhang, Y. Wang, H. Shi, P. Zhang, and Z. Shen, Far-field coseismic displacements associated with the 2011 tohoku-oki earthquake in japan observed by global positioning system, *Chinese Science Bulletin*, *56*, 2419–2424, 2011.

Watanabe, S.-i., M. Sato, M. Fujita, T. Ishikawa, Y. Yokota, N. Ujihara, and A. Asada, Evidence of viscoelastic deformation following the 2011 tohoku-oki earthquake revealed from seafloor geodetic observation, *Geophysical Research Letters*, *41*, 5789–5796, 2014.

Yabuki, T., and M. Matsu'ura, Geodetic data inversion using a bayesian information criterion for spatial distribution of fault slip, *Geophysical Journal International*, *109*, 363–375, 1992.

Yamagiwa, S., S. Miyazaki, K. Hirahara, and Y. Fukahata, Afterslip and viscoelastic relaxation following the 2011 tohoku-oki earthquake (m w 9.0) inferred from inland gps and seafloor gps/acoustic data, *Geophysical Research Letters*, pp. n/a–n/a, 2014.

Yokota, Y., K. Koketsu, Y. Fujii, K. Satake, S. Sakai, M. Shinohara, and T. Kanazawa, Joint inversion of strong motion, teleseismic, geodetic, and tsunami datasets for the rupture process of the 2011 tohoku earthquake, *Geophysical Research Letters*, *38*, 2011.

Zhao, B., W. Wang, S. Yang, M. Peng, X. Qiao, R. Du, and Z. Nie, Far field deformation analysis after the mw9.0 tohoku earthquake constrained by cgps data, *Journal of Seismology*, *16*, 305–313, 2012.